# SENSITIVITY ANALYSIS AND PARAMETERIZATION OF PASSIVELY MEASURED PROMPT-DIAGNOSTIC SIGNATURES FROM A NUCLEAR DETONATION AND THE EFFECTS ON EARLY-TIME ATTRIBUTION

A Dissertation
Presented to
The Academic Faculty

By

Evan M. Redd

In Partial Fulfillment
of the Requirements for the Degree
Doctor of Philosophy in the
School of Mechanical Engineering
Nuclear and Radiological EngineeringDepartment

Georgia Institute of Technology

December 2017

**SENSITIVITY ANALYSIS AND PARAMETERIZATION OF PASSIVELY MEASURED PROMPT-DIAGNOSTIC SIGNATURES FROM A NUCLEAR DETONATION AND THE EFFECTS ON EARLY-TIME ATTRIBUTION**

Approved by:

Dr. Anna Erickson, Advisor
School of Mechanical Engineering
Nuclear and Radiological Engineering Program
*Georgia Institute of Technology*

Dr. Glenn Sjoden
Chief Scientist
Air Force Technical Applications Center - Former Nuclear and Radiological Engineering Program at Georgia Institute of Technology
*United States Air Force*

Dr. Michael Shannon
School of Mechanical Engineering
Nuclear and Radiological Engineering Program
*Georgia Institute of Technology*

Dr. Adam Stulberg
The Sam Nunn School of International Affairs
*Georgia Institute of Technology*

Dr. Brandon Grogan
Nuclear Security Modeling Group
*Oak Ridge National Laboratory*

Date Approved: August 25, 2017

A good plan, violently executed now, is better than a perfect plan next week.

*General George S. Patton*

For Ollie.

## TABLE OF CONTENTS

## LIST OF TABLES

## LIST OF FIGURES

## SUMMARY

An orphaned nuclear detonation in an urban environment would create enormous pressure on policy makers to act quickly requiring strong attribution evidence. Traditional post-detonation nuclear forensic science focuses on delayed particulate collection methods and lengthy laboratory analyses which impedes availability of empirical attribution evidence. Therefore, characterization of passively measurable prompt emissions emanating from a nuclear detonation, within 60 seconds, bolsters traditional post-detonation nuclear forensic collection and analyses. Passively measurable emission detectability limits require categorization into peri-detonation nuclear forensics or prompt phenomena occurring within 60 seconds and post-detonation or delayed phenomena following 60 seconds. Because of the competing physical effects and number of unknowns that affect prompt emissions, global and local sensitivity methods must be employed for determining which device characteristics can be determined at early-times. The results of these sensitivities and trends aid a Monte Carlo Filtering matching algorithm that accurately determines yield, fuel-type(s), mass, and height-of-burst from hypothetical photon emissions produced by simplified Fat Man and Little Boy design derivatives. Additionally, signatures emanating from nuclear cloud rise between approximately 3 and 60 seconds clarified ambiguous results from the Monte Carlo Filtering algorithm, reducing uncertainty and improving accuracy. Superior Monte Carlo Filtering accuracy and lowered uncertainty indicates promise of using signatures from nuclear cloud rise as diagnostic indicators, if earlier data is destroyed or unavailable. Additionally, experimental photon emission sensitivities were shown with varying masses of $^{239}$Pu within 0.01 seconds of irradiation using selected energy ranges from the 47-group photon energy structure. The derived early signatures may provide policy makers with empirical technical nuclear forensics information when combined with information from other sources.

# CHAPTER 1
# INTRODUCTION

Post-detonation nuclear forensics is a broad and complex problem spanning multiple scientific disciplines. The complexity, uncertainty, and limitations related to post-detonation nuclear forensics require statistical methods/models to study passively measurable radioactive emissions. These methods extract and highlight pertinent information from passively measured signatures to expedite the attribution process. To facilitate attribution time line reduction, the importance metrics developed through statistical methods are used to highlight the most relevant experimental and computational results. In parallel, experimental assessment of detector technology provides constraints on data availability and provides realistic input parameters - detector capabilities - for modeling and simulation. Most importantly, the results limit conclusions and inferences related to device reconstruction/characteristics primarily affecting attribution conclusions. The overall research goal is to expedite the attribution process by determining detonation characteristics and design features from prompt nuclear forensic indicators considering current detection capabilities and limitations.

## 1.1 Problem Context

Following a nuclear detonation in an urban setting, chaos, devastation, and radioactivity hinder early efforts to collect fallout samples. Surviving static monitoring stations and air-sampling methods are options for collecting debris. All collection methods contain a time delay; potentially extending the nuclear forensic time line and corresponding attribution. In the event of a nuclear attack, real-time technical nuclear forensics information shortens the forensic time line moving attribution earlier. Additionally, advancements in technical nuclear forensic capabilities strengthen nuclear deterrence strategy.

The Nuclear Forensics and Attribution Act of 2010 concerns thwarting a nuclear ter-

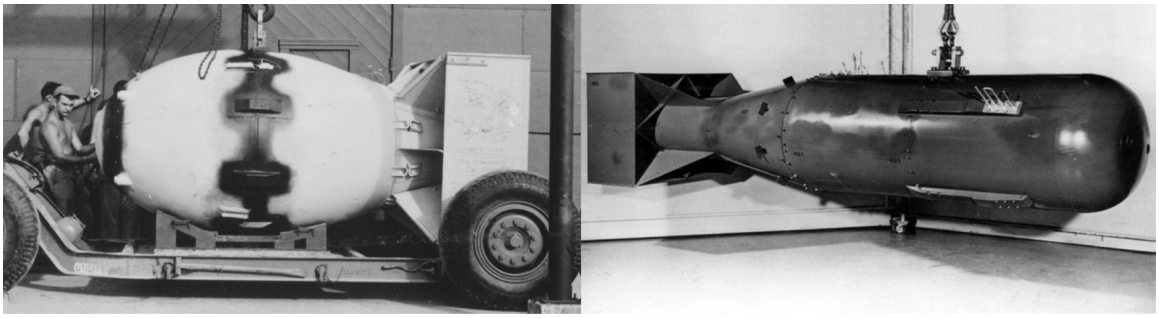

Figure 1.1: Fat Man (left) and Little Boy (right) devices. Determining these designs following detonation is on the order of weeks following start of laboratory analysis.

rorist attack against United States' interests [1]. The act facilitates development of nuclear forensic science/attribution capabilities for ascribing a nuclear attack with the goal of using the attributive ability as a deterrent against the use and proliferation of nuclear weapons [1]. Conceivably, terrorist organizations lack defined borders and centralized government causing attribution to be insignificant. In all likelihood, a terrorist organization would relish being attributed to a nuclear attack. Therefore, direct deterrence has less of an effect, if any, against nuclear terrorism. Lack of organizational borders also poses a problem because producing material for a nuclear device requires complex processes, facilities, and machinery. Organizational and production challenges may force terrorists to acquire nuclear material or device from a state source.

## 1.2 Nuclear Forensic Background

Nuclear forensic science is considered a new field within the nuclear treaty monitoring community. The science provides a deterrent of using nuclear weapons by bolstering a strong attribution program [2]. Pre- and post-detonation nuclear forensics each present challenges ultimately affecting attribution. The complexities and breadth of challenges force post-detonation forensics to be divided into peri- and post-detonation categories.

## 1.3 Peri-Detonation Nuclear Forensics

Because of the differing emission production pathways, this research isolates phenomena and emissions into prompt or peri-detonation and delayed or post-detonation effects. Peri-detonation phenomena encompass initial nuclear radiation output by the fireball and early-stages of the radioactive cloud. The peri-detonation period ends and post-detonation nuclear forensics begin once prompt output is no longer distinguishable/detectable. For clarity of the period boundaries, gamma rays emitted by fission and fission products from a 20 kiloton (kt) detonation have an effective distance of roughly 2 miles. Once the radioactive cloud from a 20 kt blast reaches 2 miles, the initial radiation has little effect, which is near one minute [3]. Therefore, peri-detonation effects span up to one minute while post-detonation encompasses effects greater than one minute. Each period presents its own challenges and holds information about device characteristics needed for attribution purposes. Extracting relevant information during the peri-detonation period requires computational statistical methods, such as sensitivity analysis (SA), because of inhibiting phenomena that obscures prompt emissions.

## 1.4 Sensitivity Analysis Application to Peri-Detonation Nuclear Forensics

The abundance of variables affecting radiation emission from a detonation requires the use of sensitivity analysis (SA). SA is a versatile tool for studying input-output models benefiting the researcher by determining [4]:

- model accuracy
- significant factors and insignificant parameters of the model
- regional maximums and minimums of model variation
- optimal regions in factor space for desired response

- factor interactions

SA can be divided into screening, local, and global methods. Screening methods produce qualitative measures on the output response while local methods produce "local" one-factor-at-a-time (OAT) measures on the output response. Global SA methods relate uncertainty in the output response to the possible distribution of the input factors or uncertainty [4]. The amount of data and variables associated with early-time emissions require the use of global SA techniques. Passively measurable signatures following a nuclear detonation are energy dependent and evolve over time. In this case, global SA methods determine the time-dependent importance of input variables (i.e. fuel-type, neutron spectrum shape, flux magnitude, etc.). Simply, this analysis has the ability to "sift" through the noise associated with passive detection and highlight only the dominant variables.

Additionally, Monte Carlo filtering (MCF) can greatly benefit the nuclear forensic scientist. MCF rejects sets of model simulations that fail to match a predetermined result or constraint often called "acceptable behavior [4]." The goal is to simply identify factors that contribute the most to the desired pre-selected output [5]. MCF, in this research, assigns the "unknown" photon emission spectrum as the output or constraint. Realistically, the "unknown" cases would be truly unknown in the field but in this case derivative designs were chosen to mimic Fat Man and Little Boy pure fission devices. Through Monte Carlo sampling of the input variables, the factors or groups of factors that create the desired photon spectrum are categorized as behavioral or acceptable.

## 1.5 Peri-Detonation Nuclear Forensic Experimental Problem Context and Motivation

Computationally determining sensitivities related to photon production contain uncertainty in the data used for analysis. The theory and data itself is derived from experimental research and observations. Experimental analyses present their own challenges when related to peri-detonation detectability. The prompt time scale of the event places heavy empha-

sis on the detection system employed which ultimately dictates information availability. Connecting computational and experimental results/limitations is invaluable for advancing peri-detonation nuclear forensic analyses.

For perspective of the time scale, the burnup period of a nuclear detonation is a fraction of a microsecond [3]. Logically, device reconstruction should begin closest to time zero as possible because the device is partially intact and revealing clues through prompt radiation emission. Information from the fissioning fuel, structural components, and energy output is present in this tiny window and expedites attribution evidence production. Gaining the most information in this short period is vital in peri-detonation nuclear forensics placing requirements on the detection system employed. Assessing current detection technologies allows for placing computational limitations on data analyses/conclusions as well as early-time attribution conclusions/capabilities.

# CHAPTER 2
# DETERRENCE BY EARLY-TIME ATTRIBUTION: PERI-DETONATION NUCLEAR FORENSICS

Whether clandestine, an act of terrorism, or warfare, a nuclear detonation creates a momentous impact on the world that is impossible to quantify. No matter the pathway to non-state nuclearization, the potential for a nuclear detonation by a non-state actor or clandestine operation shifts the scales to improvement of safeguards and nuclear treaty monitoring capabilities.

## 2.1 Peri-Detonation Nuclear Deterrence

The unknown magnitude of effects stemming from a nuclear detonation requires all deterrent strategies to be implemented. During the Cold War, the nuclear powers were known and the consequences/outcomes of an attack were also, to some extent, known. Because of this, nuclear deterrence was arguably a byproduct formed through the development and acquisition of nuclear weapons. The U.S. began shifting its deterrence strategy from attacking dense population regions to more targeted action which was addressed in many speeches of Secretary of Defense Robert McNamara (1961-1968), calling for a Single Integrated Operational Plan (SIOP) that focused on the destruction of military targets [6]. These public statements on strategic nuclear war policy further demonstrate the clear lines of engagement and targets. Clarification of nuclear strategy is also demonstrated by the appearance of the mutually assured destruction (MAD) strategic doctrine in the 1960s [6]. Another example involved the U.S. withdrawing from the Anti-Ballistic Missile Treaty in 2002 for development of smaller and more accurate nuclear weapons [6]. When defined borders and somewhat known retaliation measures/consequences exist, expanding and modernizing nuclear capabilities deter aggression and use of nuclear weapons. Objectives of nuclear

weapon use during the Cold War was strategic and military driven, producing a level of predictability. Conversely, the wide range of possible motivations and predictability of terrorism and rogue nations have changed the balance of nuclear deterrence.

Deterrence research following the collapse of the Soviet Union began moving towards other threat sources. September 11, 2001 firmly shifted deterrence strategy to include asymmetric threats from terrorist and rogue nations. The strategy change also brought into debate the magnitude deterrence would contribute to national security policy [7]. Whether a centralized or subtle role, WMD deterrence, specifically nuclear, in a constantly changing threat spectrum must be itself adaptive and be comprehensive - including nuclear forensics. Jeffrey W. Knopf categorizes nuclear forensics into a sub-category of "fourth wave" deterrence strategy [7].

Extensive research has been done on deterrence strategy. Historically, during the Cold War era, deterrence was categorized into three waves. These waves were focused on direct state conflict that was prevalent and most likely at the time [7]. Most relevant, the third wave attempted to bring empirical evidence into deterrence strategy that was lacking in the previous two waves. Additionally, the third wave highlighted historical deterrence strategy failures [8]. The third wave research had clear focus on strategy related to state actors while fourth wave addresses deterring asymmetric threats such as rogue nations and terrorists.

Nuclear forensic science arguably provides a direct and indirect deterrent. The Comprehensive Nuclear Test-Ban Treaty Organization's international monitoring systems have conceivably deterred above ground nuclear testing while strong attribution capabilities deter potential proliferation sources. With respect to asymmetric threats, nuclear forensic science is most applicable to the fourth wave deterrence strategy. Fourth wave deterrence strategy employs several deterrents such as denial, punishment, indirect methods, and non-military options such as delegitimization [7]. If nuclear terrorism occurred, the device would likely take these forms, in order of casualties and likelihood: (1) a radiological dispersal device (RDD), (2) an improvised nuclear device (IND), or (3) a sophisticated nuclear

device (SND). The SND and material for the IND likely will be gained/diverted through a sophisticated source. Thus, deterring the potential source is the next logical step. Hence, nuclear forensics creates an indirect deterrent to the source of the nuclear device or material. Displaying advanced - empirical - capabilities of attribution would enable fear of discovery and subsequent retaliation to the source country. There are technical challenges related to timely data availability and uncertainty.

Researchers have brought up several concerns with post-detonation nuclear forensics contribution to deterrence. The main technical concern is the availability of samples for comparison to the blast debris. Also, for nuclear forensic science to be a deterrent, the capabilities would need to be public information and reach potential source states. This requirement is a double-edged sword as known capabilities highlight vulnerabilities. Although, public release of nuclear forensic funding, active research, and vague capabilities possibly dulls one-side of the blade. Another hurdle directly applicable to this research is timeliness of post-detonation results.

Deterrence research has focused on physical debris collection for nuclear treaty monitoring and forensics purposes [1] [7]. For instance, a nuclear terrorist attack was deemed "the most serious threats to the national security of the United States." This act placed heavy emphasis on development of nuclear forensics program for attributing a nuclear detonation. Per section 2 of the Nuclear Forensics and Attribution Act, many of the radioisotopes produced by a detonation are short lived requiring timely sample collection. Expedient sample collection requires obtaining atmospheric debris for analysis. According to the Nuclear Forensics and Attribution Act, atmospheric sample collection capabilities have diminished over the past several decades. Development and advancement of this capability creates an effective indirect deterrent against the use or proliferation of nuclear weapons[1]. Obtaining and analyzing debris from a nuclear detonation takes considerable time. Devastation following a nuclear detonation will place extreme pressure on the policy makers to act. Peri-detonation nuclear forensics provides objective data to the policy maker for consider-

ation. Although the data is limited at these early times compared to laboratory produced data, the coarse information may provide actionable data. The subtle underlying challenge then becomes relating limited empirical evidence associated with peri-detonation nuclear forensics to confidence of decisions.

While current U.S. Congress opinion on creating a strong and credible nuclear deterrent is advancement and maintenance of the nuclear triad [9]. The Nuclear Forensics Attribution Act directs developing/advancing the technical nuclear forensics capability to strengthen the collective response of the United States to nuclear terrorism or other nuclear attack. Post-detonation nuclear forensic science produces scientific evidence that can be applied for attribution. Furthermore, if law enforcement and intelligence determined the source of attack they will require supporting evidence [10] - partly originating from post-detonation technical nuclear forensic conclusions. The ability of nuclear forensic science creating a modern, indirect, nuclear deterrent to the transfer of nuclear capabilities from a weapon state bolsters the effectiveness of the U.S. governments attribution capabilities.

## 2.2 Advantages and Limitations of Post-Detonation Nuclear Forensics

Obtaining an early-time sample of nuclear device debris for analysis following a nuclear detonation is challenging. Radioactivity levels, fire, debris, and blast damage potentially hinders early-time efforts for airborne or ground sample retrieval. Assuming it was possible, the subsequent radiochemical forensic analysis potentially extends the attribution time line further due to the detailed separation processes.

Speculated timelines from pre-detonation estimates place determination of nuclear origin and explosive yield within hours. Preceding laboratory analysis, a sample must be collected and transported to a laboratory. Scientists could then determine the isotopic composition and rough material history days after laboratory analysis began. Then the fuel-type and sophistication level can be determined. Determining device design and matching known designs take place several weeks after laboratory analysis [11]. This timeline

provides concern if early-time attribution is desired. Average political action from conventional attacks is 19 days with a median of 10 days [12]. Political action would arguably be similar following a nuclear attack.

Current prompt diagnostic systems carry associated uncertainties and are likely to be affected by the environment in between the burst and sensor location. However, prompt diagnostic systems offer timely data on an event compared to airborne and ground materials collection methods. Obtaining and analyzing an airborne sample is a likely early-time option for materials/debris collection. The U.S. has two WC-135 "Constant Phoenix" airplanes in service for treaty monitoring that may be available for nuclear forensics applications [13]. These airplanes recover airborne radioactive particles. The requirement of flying through a radioactive cloud may hinder extremely early analysis/collection because of high activities present. Early-time ground debris collection is also complicated due to the extremely high radioactivity. There is also a Ground Filter Unit (GFU) network consisting of particulate sampling using filter paper and distillation devices that can collect complementary samples to the WC-135. Unfortunately, the GFU network requires samples to be physically removed and shipped to laboratories [14]. Laboratory equipment has been found to be far more superior than field instruments [11].

Passively measurable signatures provide a mechanism to gain early-time attribution information. Current networks of systems, such as the CTBTO's International Monitoring System can detect a detonation event, but can infer very little about the device itself. These existing infrastructures focus primarily on secondary signatures from a detonation, such as speed of sound phenomenology (seismic, hydro-acoustic etc.) and volatile fission products. These tools can provide some information in a short period of time; however, limitations do exist and tends to be associated with a high degree of uncertainty [15]. A more promising route is to measure primary signatures such as photons and neutrons because of their underlying properties. Measurements of these early-time emissions, will be referred to in this research, as peri-detonation nuclear forensics. Increasing knowledge and modeling of

such peri-detonation phenomena potentially provide high-impact contribution to nuclear forensic science.

## 2.3 Peri-Detonation Nuclear Forensics Contribution to Nuclear Detonation Characterization

A domestic nuclear detonation requires a cohesive contingency structure following the event [16]. Many challenges are present following a detonation mainly mitigating further loss of life and consequence management. Strategically, attribution and (potential) retaliation are the main drivers for nuclear forensic science.

The broad field of post-detonation nuclear forensics offers many methods of information extraction mostly from laboratory analysis of collected debris. Due to the associated nanosecond timescales, peri-detonation forensics is potentially capable of obtaining direct measurement of the device itself. Because peri-detonation encompasses prompt burnup, the structure and fuel of the device are partially intact at the time of measurement and emitting passively measurable radiation. Fissioning material and promptly activated structural component signatures are only present during and shortly after the prompt burnup period, well before laboratory or field analyses can take place. Indications of fuel type, structural components, and energy output can correlate to information relating to the device.

The severity of consequences involving a nuclear detonation requires due diligence with respect to the collection/analysis of nuclear forensic evidence. In the case of an orphaned nuclear detonation, providing a definitive/accurate answer weeks to months later can be detrimental. Peri-detonation forensics can provide a middle ground, by providing information within 60 seconds, but with some associated uncertainty. Peri-detonation forensics is not expected to supersede existing methods, but to complement by gathering information at a crucial time, when scientific data is scarce.

## 2.4 Peri-Detonation Nuclear Forensic Challenges

The information extracted by peri-detonation forensic methods is constrained by detector technology, weapon effects, environment, and inherent physical uncertainties. These extreme circumstances mitigate the ability to correlate measurable output to device characteristics ultimately impeding the amount of information available. Examining factors that affect determination of device characteristics places restrictions on conclusions due to uncertainty and reveals other relationships between device output and characteristics.

Many factors influence the ability to gain early time information from passively measurable signatures. Weapon physics, weather, and structures/materials found in an urban environment can negatively affect signal production and propagation. If signal were available, the ability to detect the emissions is the next logical challenge.

The conditions surrounding a nuclear detonation within an urban environment are somewhat unknown, but must be accounted for when measuring the emission output. Because the time of detonation is unknown, the deployed detector technology would require ruggedness. Also, the distance from the blast would dictate the amount of signal in the detector requiring a large array or crystal. The largest hurdle for detection is simply the existence of a detector in the blast vicinity. Custom detection systems would need to be strategically placed for information gathering. Additionally, leveraging existing monitoring stations or networks behavior following a blast is possible in gaining early-time information. Consequently, peri-detonation technology deployment and development is likely costly.

# CHAPTER 3
# PERI-DETONATION SENSITIVITY/UNCERTAINTY ANALYSIS TECHNICAL APPROACH AND RESULTS

Early-time determination of nuclear device design features and detonation characteristics require statistical methods capable of revealing subtle characteristic artifacts from prompt emissions. Device physics, environmental factors, competing variables (e.g. different fuel types, flux magnitude and shape), and other exacerbating factors oftentimes obfuscate meaningful information found in prompt emissions. One method of determining variable importance is applying sensitivity analysis to prompt emissions. Saltelli offers a definition of sensitivity analysis (SA) as the study of the uncertainty in the model output can be apportioned to different sources of uncertainty in the model input [17]. SA aids the researcher in understanding the underlying laws or rules of the system and the effect on the desired responses or outcomes. Peri-detonation nuclear forensic SA focuses analysis to a critical region of the system revealing early-time exploitable characteristics. Specifically, the effects of model inputs - device design features - on passively measurable radiation and deduction limitations of device characteristics. Peri-detonation system behavior and relationships are determined by multiple sensitivity methods.

## 3.1 Sensitivity/Uncertainty Analysis Methods and Background

SA offers many useful purposes in modeling complex systems by exposing technical errors, identifying dominant regions in the input space, simplifying models, and guiding research priorities [17]. SA has many methods, sub-categories, and metrics. A complement to SA, Monte Carlo Filtering (MCF), allows the researcher to determine needed behavior for a desired outcome (e.g. conditions required for a given detector response or photon spectrum). This research employs local, global, and MCF methods.

### 3.1.1 Local Sensitivity Analysis

Local SA methods primarily use partial derivatives for the computation of sensitivity indices. The dependence of an output response,$Y_i$, on an input variable, $X_j$, can be shown with the partial derivative, $\partial Y_i/\partial X_j$. This method is limited when the model input is uncertain and of unknown linearity [17]. The derivative is oftentimes unnormalized and simply based on the raw input and output values resulting in variables demonstrating equal importance on the output response. Oftentimes, weighting the partial derivative with the standard deviations of the input/output reveals input variable importance. Shown below in Eq. 3.1 is the sigma-normalized sensitivity coefficient using the same above variables [17].

$$S^{\sigma}_{\mathrm{X_j}} = \frac{\sigma_{X_j}}{\sigma_{Y_i}} \frac{\partial Y_i}{\partial X_j} \tag{3.1}$$

As previously mentioned, local sensitivity measures (sigma-normalized and unnormalized) do not provide perspective of ranking input variables on the desired output response. However, the sigma-normalized partial derivative can be further normalized to unity, providing a pseudo-ranking system of input variable importance. A simplified method of providing a ranking system to the input variables is shown below in Eq. 3.2.

$$\sum_{j=1}^{r} (S^{\sigma}_{\mathrm{X_j}})^2 = 1 \tag{3.2}$$

Another method in gaining a local sensitivity metric is to simply plot the dependent and independent variables. Examining the trend between the independent and dependent variables can provide insight into the correlation between the variables. Simply, fitting a line and determining the strength of fit of the plotted data provides an empirical correlation metric or the pseudo-main effect coefficient between the dependent and independent variables.

The above local methods provide sensitivity metrics between the input variables - design features - and output response but does not account for potential interactions between

the input variables or any nonlinearities in the model. Sobol developed a method for determining a variable's total effect on an output response which provides insight into any variable interactions and nonlinear associations.

### 3.1.2 Global Sensitivity Analysis

Local SA methods are, by name, bound to "local" regions of the input space often using one-factor-at-a-time (OAT) calculations. Global methods have the ability to examine all regions of the input space. Variance decomposition is one such global method. Saltelli et al. offers 4 "settings" for SA [5]:

- Factors Prioritization (FP): determination of which variable to fix that causes the greatest reduction in output uncertainty.
- Factors Fixing (FF): identification of noninfluential factors or groups of factors.
- Variance Cutting (VC): determination of the least amount of input variables to reach a prescribed level of output uncertainty.
- Factors Mapping (FM): identification of dominant factors that produce a desired output response.

Conveniently, variance based SA methods are conducive in determining FP, FF, and VC points. The last item encompasses MCF methods which are discussed later.

*Variance Decomposition Background*

Beginning with a model denoted by the function $Y = f(\mathbf{X})$. All factors spanning their ranges of uncertainty are denoted by the $\mathbf{X}$. The function's total variability results from contributions from all variables and is known as the unconditional variance, denoted by $V(Y)$. Logically if an input value was known, the associated uncertainty from that input variable would be removed from the output response. Therefore by setting an input variable

to a "known" amount, $X_i = x_i^*$ while varying other variables gives the amount of output variance associated with the input variable. $V_{X_{\sim i}}(Y|X_{\mathrm{i}} = x_{\mathrm{i}}^*)$ is the variance of $Y$ taken over all factors but $X_i$ or $X_{\sim i}$. This measure is also called the conditional variance [5]. The conditional variance should be less than the unconditional variance because of only one variable being frozen. This inequality allows $V_{X_{\sim i}}(Y|X_i = x_i^*)$ to become a ranking system of the input variables. Although, there is a problematic high dependence on $x_i^*$'s input space position. This dependence is removed when $x_i^*$ is averaged over all values [17] and the formulation is shown below in Eq. 3.3. The property shown in Eq. 3.4 allows for an importance measure to be ascertained.

$$E_{X_i}(V_{X_{\sim i}}(Y|X_i)) \tag{3.3}$$

$$E_{X_i}(V_{X_{\sim i}}(Y|X_i)) + V_{X_i}(E_{X_{\sim i}}(Y|X_i)) = V(Y) \tag{3.4}$$

By weighting the conditional variance, $V_{X_i}(E_{X_{\sim i}}(Y|X_i))$, by the unconditional variance, $V(Y)$, the first-order sensitivity measure or main effect is obtained in Eq. 3.5.

$$S_i = \frac{V_{X_i}(E_{X_{\sim i}}(Y|X_i))}{V(Y)} \tag{3.5}$$

A high $S_i$ value equates to a high-importance for the input variable. This value is the main effect contribution to the variance in the output for each input variable. $S_i$ mimics a correlation coefficient between the model output and the input variable. Correlation coefficients are not suited for nonlinear relationships in the model indicating only estimates of linear relationships. A total sensitivity measure that takes into account nonlinearities and interactions between variables is needed.

Sobol's variance decomposition method calculates a total sensitivity index that encompasses all main and higher-order effects from interactions. The notation $V(E(Y|X_i))$ is used for $V_{X_i}(E_{X_{\sim i}}(Y|X_i))$. Sobol introduced decomposing the unconditional variance of

a model with $k$ input variables into a sum of all conditional variances shown in 3.6 [5].

$$V(Y) = \sum_i V_i + \sum_i \sum_{j>i} V_{ij} + ... + V_{12...k}; \tag{3.6}$$

where:

$$V_i = V(E(Y|X_i))\text{—main effect of } X_i; \tag{3.7a}$$

$$V_{ij} = V(E(Y|X_i, X_j)) - V_i - V_j\text{—joint effect of } X_i \text{ and } X_j \text{ sans their main effects;} \tag{3.7b}$$

$$V_{ijm} = V(E(Y|X_i, X_j, X_m)) - V_{ij} - V_{im} - V_{jm} - V_i - V_j - V_m; \tag{3.7c}$$

The process continues up to $2^k - 1$ unconditional variances which is referred to as the curse of dimensionality. Eq. 3.6 can then be divided by $V(Y)$ resulting in Eq. 3.8. Sobol's total effect index, shown in Eq. 3.9 for a 2-variable model, reveals the additive nature of the model. For example, differences between $S_{T_i}$ and $S_i$ values implies interactions or nonlinear effects.

$$\sum_i S_i + \sum_i \sum_{j>i} S_{ij} + ... + S_{12...k} = 1; \tag{3.8}$$

$$S_{T_1} = S_1 + S_{12} \tag{3.9}$$

Sobol's variance decomposition method reveals the behavior of the model output due to input variables. Calculating all sensitivity indices requires a high computational cost. This research introduces energy, time, and spatial dimensions further increasing computational cost.

*Monte Carlo Sampling*

This research uses Monte Carlo sampling for determination of sensitivity indices. The variables studied/sampled were: neutron spectrum (shape), flux (magnitude), and fuel-type ($^{238}$U, $^{235}$U, $^{233}$U, $^{239}$Pu). All variables were sampled over uniform distributions.

For the neutron spectrum shape, samples were generated by moving from a Watt Spectrum to a pure high-energy (HE) Dirac delta function at 14 MeV. The perturbation method for the group dependent spectrum shape is found in Eq. 3.10 [18]. Perfetti uses this method for perturbation of the prompt fission neutron emission spectrum or chi spectrum probability. This perturbation method assumes changing the emission probability in one energy group affects all energy groups.

$$\begin{aligned} P(n_{i=g})' &= P(n_i) + \delta P(n_g) \\ P(n_{i\neq g})' &= P(n_i)\frac{1 - P(n_g) - \delta P(n_g)}{1 - P(n_g)} \end{aligned} \tag{3.10}$$

where:

$P(n_g)$: Probability of neutrons in group g.

To guarantee coverage of average neutron energies, $\bar{E}_{neutron}$, a stratified sampling method was also used. Stratified sampling divides the uniform distribution into even segments based on the number of total samples to assure sampling within each region. The flux magnitude was sampled between 1.0E+26 - 1.0E+30 $\frac{neutrons}{cm^2 - second}$. Fissile and fissionable fuels were also uniformly sampled. For primary fuel types, $^{235}$U, $^{233}$U, $^{239}$Pu, masses were sampled between 3.0 and 50.0 kilograms. The secondary fuel type or reflector, $^{238}$U, was sampled between 0.0 and 1000.0 kilograms.

### 3.1.3 Monte Carlo Filtering

Monte Carlo filtering (MCF) is an SA method used in diagnostic modeling. By setting a predetermined constraint, the model is conditioned to best mimic the desired behavior.

Prior distributions of model input values are sampled and evaluated based on the proximity to the desired behavior. The prior statistical distributions represent uncertainty in the system. This classification system is related to the first-order effects discussed in Section 3.1.2. MCF makes no attempt to explain higher-order effects or variable interactions [5]. For this research, MCF is used to determine the most-likely design features and characteristics based on the prompt photon output. Uncertainties in the nuclear data are considered for MCF methods but not in acceleration schemes.

### 3.1.4 Uncertainty Analysis

There are many sources of uncertainty associated with computational simulations. Simulated photon emission uncertainties lie within the nuclear data and geometry specifications. These cross-section uncertainties create a fluctuation/distribution of possible device yields which are used for scaling the prompt photon emissions and generating fission products. The prompt fission, radiative capture, and neutron inelastic scatter photon emission distribution is also affected by cross-section uncertainty. A distribution of yields is shown below that arise from cross-section uncertainties in Fig. 3.1.

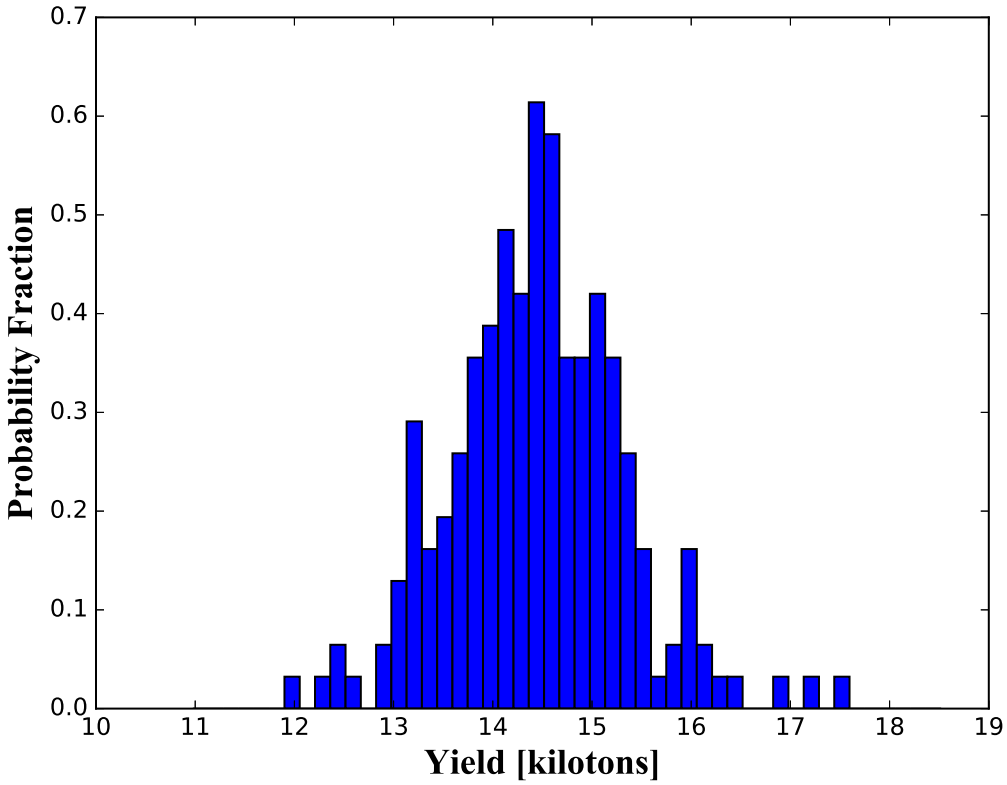


Figure 3.1: Yield distribution from cross-section uncertainties.

Fission product photon uncertainties contain more sources of error. The decay constants, fission product yields, cross-sections, and power uncertainties dominate the time/energy dependent photon emission uncertainty. Scale's Sampler module was used to quantify the time and energy dependent photon uncertainty. Sampler quantifies uncertainties associated with the multi-group cross-sections, decay and fission yield data, along with geometry input. The module uses Monte Carlo sampling of the probability density functions (PDF), rather than perturbation methods which require separate forward and adjoint calculations [19]. The Sampler module was used to generate the perturbed input decks. A custom routine was written to process and run the Sampler module for added uncertainty quantification related to photon emissions. The routine propagated the prompt power uncertainties through the Oak Ridge Isotope GENeration (ORIGEN) generated photon emissions. Nuclear data uncertainties are used in the MCF algorithm reference case photon emissions.

Noteworthy, nuclear data uncertainty was not considered with the acceleration scheme or each MCF run. This is due to the unreasonable amount of samples/calculations needed per random configuration generated. Alternatively, detailed uncertainty analysis was completed on the reference cases. Realistically, the reference spectrum would contain measurement/counting error while the MCF runs would contain error related to nuclear data and modeling uncertainty. Mimicking this logic, the energy and time dependent uncertainty calculated for the reference cases were applied to the MCF randomly generated configuration. Matching sequences were run to determine if the reference case falls within the generated MCF run.

### 3.2 Monte Carlo Filtering Affirmation, Search Parameters, and Reference Cases

MCF requires a known photon spectrum for comparison to the random Monte Carlo generated photon spectra. Once a Monte Carlo generated model was run, the output photon spectrum was compared to the reference spectrum. The randomly generated configurations contain various fuel types, densities, reflectors, and resulting yields. Several methods are employed to determine the proximity to the reference spectrum. Because MCF requires a predetermined constraint, several "known" test cases were considered. In reality, these "known" test cases would be unknown in the field but would still serve as a constraint. Their corresponding photon spectra are stored and serve as the MCF constraint. Simply, the MCF constraint is the photon spectrum the algorithm is trying to match. All photon spectra have used the same detector response functions. These response functions yield a convenient uncertainty bound on the photon energy bins. Logically, a configuration is matched if the rate or counts in the photon energy bin from the reference case falls within the range of nuclear data uncertainty in the MCF run. To determine proximity, several metrics are used on the reference and randomly generated configuration spectrum.

Because the reference spectrum contains error associated with counts and nuclear data, the randomly generated spectrum is checked against the upper and lower bounds of the ref-

erence spectrum and assigned a score based on "passes." The integral counts, detection rate, and ratios are compared between each generated case and assigned a score. A chi-squared metric is then applied and divided by the degrees of freedom to determine the distance away from the reference spectrum. Additionally, the reference spectrum and randomly generated spectrum are both normalized to unity. This normalization forces the algorithm to examine the shape of the photon spectrum rather than the magnitude which is more indicative to fissioning or activated structural components. Each of the metrics used in the scoring function are shown below in Eq. 3.11.

**Scoring Function**

$$Score_i = \gamma * \beta * \epsilon * (1.0 - \chi)$$

Where:

$$\gamma = \frac{\text{Passes}}{\text{Total Energy Bins}} \text{ Integral count match fraction for each energy bin}$$
$$\beta = \frac{\text{Passes}}{\text{Total Energy Bins}} \text{ Time-dependent rate match fraction for each energy bin}$$
$$\epsilon = \frac{\text{Passes}}{\text{Total Ratio Combinations}} \text{Integral count ratio for each possible ratio combination}$$
$$\chi = \frac{\chi^2}{\text{Degrees of Freedom}} \text{ Distance between reference spectrum and generated spectrum} \tag{3.11}$$

To provide a brief description of the scoring function, these metrics are applied to the prompt burnup front-end period to initially filter the results. After a spectrum passes the first filter, nuclear cloud rise is simulated with the filtered results and assigned scores based on the same formula. Simply, results passing the first filter are further scrutinized by grading the signatures emanating from the nuclear cloud rise period. This second filter is meant to analyze fission product photon emission, neutron activation in the cloud, and lingering fuel-type emissions. Fortuitously, by applying realistic detector settings and characteristics, the matched MCF configurations highlight the effect of technology capabilities on conclusions.

The possible fuels and reflectors that are considered are shown in Tables 3.1 and 3.2

with their corresponding weight fractions [20]. Combinations of these fuels and reflectors are used for randomly generating different configurations. The resulting photon spectrum of the randomly generated configuration is then compared to the reference case spectrum.

Table 3.1: Fuels and corresponding compositions used in Monte Carlo Filtering analysis.

| Fuel Type | Composition [Weight Percent] |
|---|---|
| Weapons Grade Pu (WGPu) | $^{238}$Pu: 0.05, $^{239}$Pu: 93.50, $^{240}$Pu: 6.0 $^{241}$Pu: 0.40, $^{242}$Pu: 0.05 |
| Fuel Grade Pu (FGPu) | $^{238}$Pu: 0.10, $^{239}$Pu: 86.1, $^{240}$Pu: 12.0 $^{241}$Pu: 1.60, $^{242}$Pu: 0.20 |
| Aged Weapons Grade Pu (AWGPu) | $^{238}$Pu: 0.01, $^{239}$Pu: 93.63, $^{240}$Pu: 5.99 $^{241}$Pu: 0.20, $^{242}$Pu: 0.03, $^{241}$Am: 0.14 |
| Pure $^{239}$Pu | $^{239}$Pu: 100.0 |
| Highly Enriched Uranium (HEU) | $^{234}$U: 0.98, $^{235}$U: 93.16, $^{236}$U: 0.45 $^{238}$U: 5.42 |
| Pure $^{235}$U | $^{235}$U: 100.0 |
| Pure $^{233}$U | $^{233}$U: 100.0 |

Table 3.2: Reflectors and corresponding compositions used in Monte Carlo Filtering analysis.

| Fuel Type | Composition [Weight Percent] |
|---|---|
| Natural Uranium ($^{Nat}$U) | $^{234}$U: 0.0057, $^{235}$U: 0.7204, $^{238}$U: 99.2739 |
| Tungsten | $^{180}$W: 0.12, $^{182}$W: 26.23, $^{183}$W: 14.24 $^{184}$W: 30.66, $^{186}$W: 28.76 |
| Lead | $^{204}$Pb: 1.38, $^{206}$Pb: 23.96, $^{207}$Pb: 22.07 $^{208}$Pb: 52.59 |
| Iridium | $^{191}$Ir: 37.06, $^{193}$Ir: 62.94 |
| Air | $^{Nat}$C: 0.01, $^{Nat}$N: 75.53, $^{Nat}$O: 23.18 $^{Nat}$Ar: 1.28 |

Because the spatial model employs a MCF algorithm, reference cases are needed for comparison to the model runs. The first case mimics Little Boy (Uranium) and Fat Man (Plutonium) design types using open source mass estimates and randomly selected densities [21] [22]. The reference cases are shown in Table 3.3.

Table 3.3: Reference cases used for Monte Carlo Filtering analysis.

| Design Derivative | Fuel Type, Mass [kg], Density [$\frac{g}{cm^3}$] | Reflector Type, Mass[kg], Density [$\frac{g}{cm^3}$] |
|---|---|---|
| Fat Man | Pure $^{239}$Pu, 6.2, 31.6 | $^{Nat}$U, 100.0, 28.0 |
| Little Boy | Pure $^{235}$U, 34.4, 28.0 | N/A |

These design derivatives were chosen because of geometry and sophistication differences. The Fat Man derivative was an implosion type device with a $^{Nat}$U reflector. A smaller fissile mass was required because of the reflector and implosion technique which was a higher level of sophistication compared to the Little Boy derivative. The Little Boy derivative was a gun-type design with no reflector requiring more fissile mass. These two design types

show the effects of bare versus reflected assembly photon emissions and varying levels of sophistication.

The overall goal of the MCF algorithm is to find a behavioral match to the reference spectra. In order to complete this task, 5 computational calculations (labeled Sections (i) - (v)) and 1 sub-step (Section (i.a)) were performed and are described in the following section.

### 3.3 Peri-Detonation Nuclear Forensic Computational Analysis Technical Approach

The preceding variance decomposition method provides two metrics for variable importance. First-order or main effect index values show the linear strength between the input variables and model output - time and energy dependent photon emissions. Total sensitivity index values provide insight into nonlinearities and interactions between the input variables. Comparison of these two metrics invaluably highlights the underlying system behavior and dependencies. Notably, the metrics are also used in developing the MCF acceleration scheme.

Additionally, the level of complexity and breadth of the problem justify several limiting assumptions in this work. Prompt-phenomena encompasses several scientific disciplines further justifying placing scoping limits on the problem. All assumptions and methods are found in open-source literature and are intentionally simplified. The associated phenomena and assumptions are grouped in each corresponding calculation section. For clarity, the following section describes the computational workflow used in this research.

The overall calculation progression is shown below in Fig. 3.2 which is broken up into sections (i)-(v) with a sub-section (i.a) for MCF acceleration. The MCF acceleration scheme was developed from using the global and local sensitivity indices which highlighted relevant energy bins for each fuel and reflector type. These relevant energy bin to input variable relationships allowed for rough determination of present fuel types. Sub-sections to follow describe calculation methods in detail, but a brief overview description is provided.

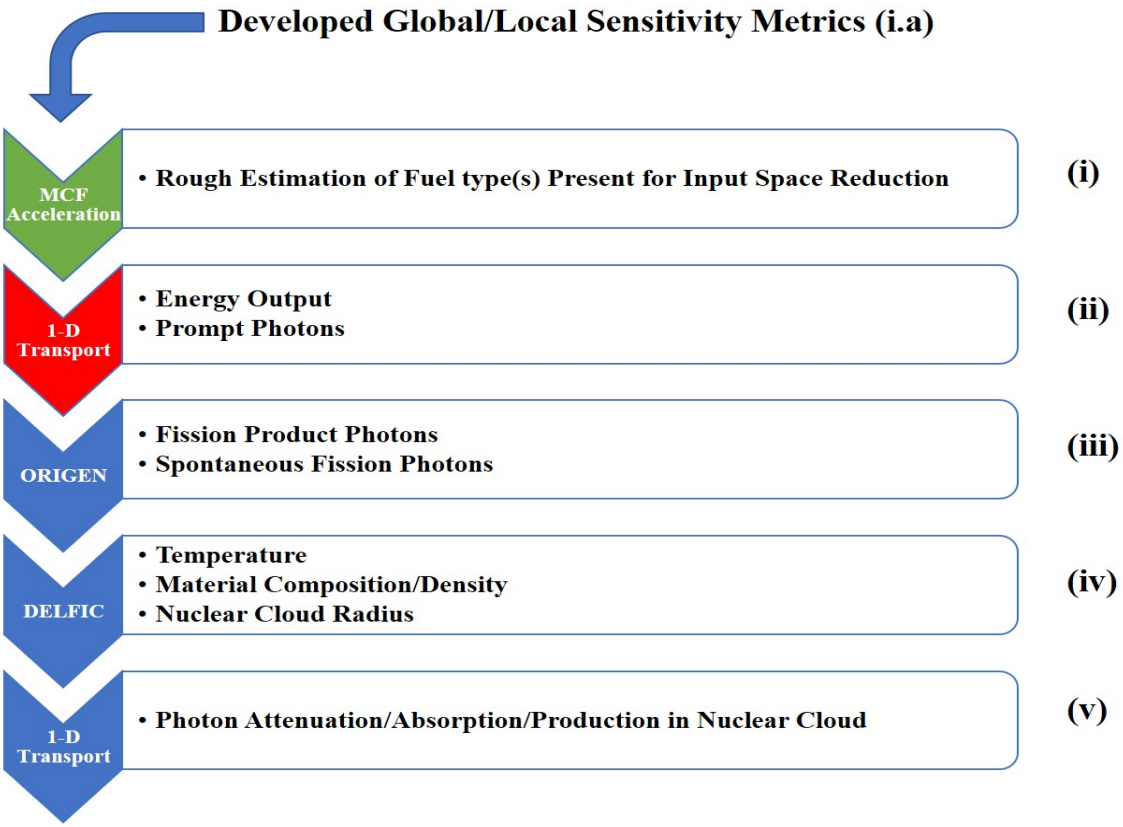


Figure 3.2: Flow diagram of computational calculations.

Before section (i) or section (i.a), global and local sensitivity analyses are completed using the Oak Ridge Isotope GENeration (ORIGEN) code which produced point-source photon emissions to highlight which energy bins and energy ratios can be used for the MCF acceleration step. Section (i) is the MCF acceleration calculation that uses the found relationships developed in section (i.a) to lower the possible MCF input space. The acceleration scheme is completed on integral counts between 1.00E-05 and 1.00E-01 seconds in the determined energy bins. In Section (ii), a 1-D discrete ordinates transport calculation is completed to provide neutronic properties and constants that allow for calculation of energy output (device yield) which dictates prompt fission, activation, and inelastic scattering photons. Section (iii) uses material compositions and spatial power levels from Section (ii) to produce point source fission product and spontaneous fission photon emissions in the ORIGEN code. Section (iv) solves a set of ODEs cited from the Defense Land Fallout

Interpretive Code (DELFIC) code to yield temperature, material composition/density, and cloud radius. The DELFIC parameters and the photon source from section (iii) are inserted into a final 1-D discrete ordinates transport calculation in section (v) as the geometry and independent photon source, respectively. All the described calculations are used to generate an energy- and time-dependent photon spectrum that is compared to the reference case, discarded or kept, and then the process repeats. Before the MCF algorithm begins, the acceleration calculation is completed for computational speedup by narrowing down the possible input space.

In this research, Section (ii) is referred to as the prompt front-end (shown in red above), while Sections (ii) - (v) are grouped in prompt back-end phenomena. This segregation is shown below in Fig. 3.3.

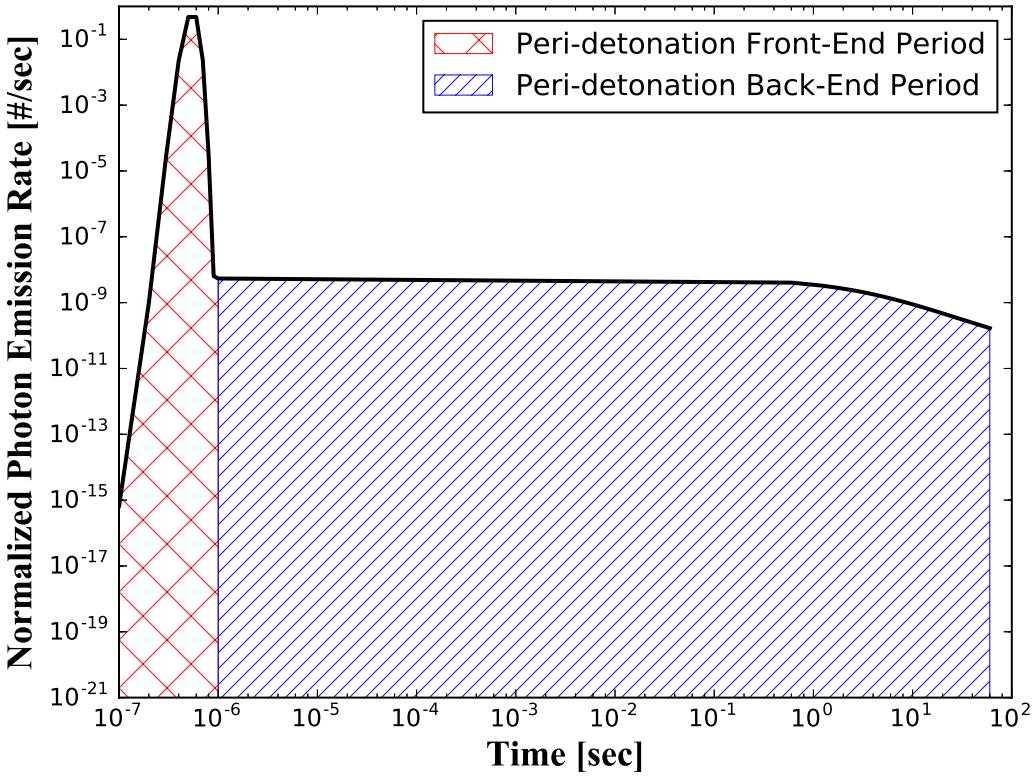


Figure 3.3: Peri-detonation spatial front and back-end model divisions.

The coarse grouping into front/back-end phenomena serves multiple purposes. Physically,

the prompt front-end burnup period (hypothetical unboosted fission) contains photon emissions from the fissioning fuel/reflector, (n, $\gamma$), and inelastic scatter (n, n'$\gamma$) reactions (among others) from structural components/fuel. Also, these front-end emissions grossly outnumber fission product photons. At this stage, the device is - mostly - intact and not deconstructed revealing real-time design hints.

### 3.3.1 Peri-Detonation Global/Local Sensitivity Metric Development – Section (i.a)

The point-source model Sensitivity Analysis (SA) is completed on the entirety of the input space with and without detector response functions to develop photon spectrum signatures/relationships related to short-lived fission products. SA reveals underlying connections between the input variables and photon signal (i.e. linearity, variable interactions, and monotonicity). These relationships then serve as an acceleration scheme that shrinks the model input space used in the spatial MCF calculation, improving computation time.

The developed point-source model exclusively uses the ORIGEN point depletion code. ORIGEN produces highly idealized isotopic and emission inventories and does not include fission or activation photons which are required for prompt analyses [23]. Also, ORIGEN is a point-source model which inherently does not account for attenuation, absorption, and scattering. Although limited, the ORIGEN point-source model serves as a good method development tool, shows overall trends in the data, highlights variable behavior, and accelerates MCF calculations. The point-source model can also mimic a radioactive sample found in the field after a nuclear detonation sans fission and activation photons.

For MCF acceleration purposes, this step also considers the integral counts between 1.00E-05 and 1.00E-01 seconds which is between the prompt burnup photon emission and infancy of nuclear cloud rise. Detector response functions were included in the predictive relationships developed. The relationships are meant to significantly lower the input space available to the MCF algorithm. Uncertainty in the acceleration scheme resulting from nuclear data was not considered because of the lengthy calculation time.

Variables considered in the point-source SA are: neutron spectrum (shape), flux (magnitude), and fuel-type ($^{238}$U, $^{235}$U, $^{233}$U, $^{239}$Pu). Using the methods in section 3.1, time and energy dependent total/first-order sensitivity indices are calculated for each variable using the methods introduced in Section 3.1. All data was stored in version 9.6 PostgreSQL databases and post-processed.

Due to the initial high temperatures, unfractionated samples were the primary research focus. Although because the nuclear cloud cools considerably within 60 seconds, trends of chemically fractionated samples were examined due to the differing elemental condensation temperatures which determine presence in the cloud.

*Chemical Fractionation*

If a nuclear detonation occurs near the surface of the Earth, the fireball will uptake the contacted environment. Some of this debris will be vaporized along with the device components, fuel, and fission products. As the fireball amalgamation begins to cool, the fission products and other debris constituents condense based on their respective condensation temperatures. If the condensation temperatures of the debris constituents are higher than the carrier material, the device constituents are distributed volumetrically in the fallout particles. A lower condensation temperature causes the device constituents to be surface distributed [24][25]. Freiling offers a definition of fractionation as "any alteration of radionuclide composition occurring between the time of detonation and the time of radiochemical analysis which causes the debris sample to be nonrepresentative of the detonation products taken as a whole [25]." An illustration of fractionation is shown in Figs. 3.4 and 3.5.

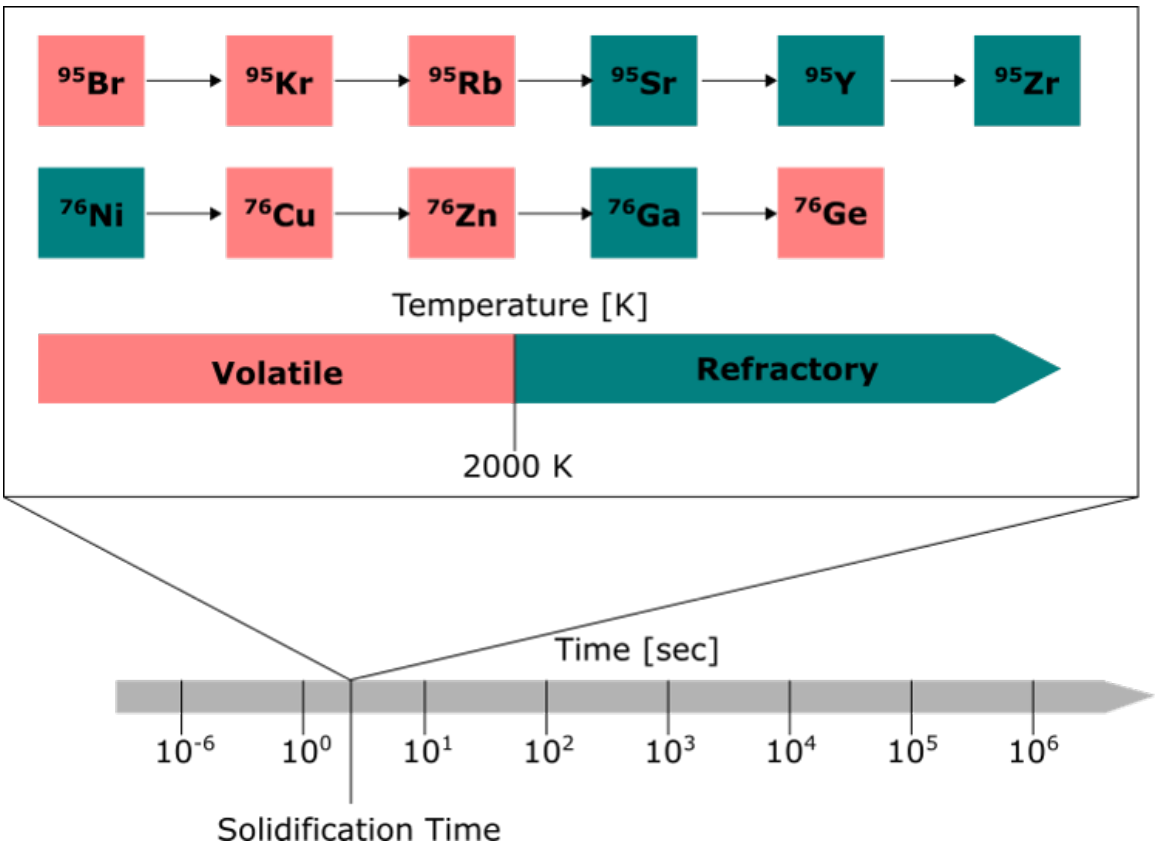


Figure 3.4: Refractory and volatile nature of mass chains 76 and 95.

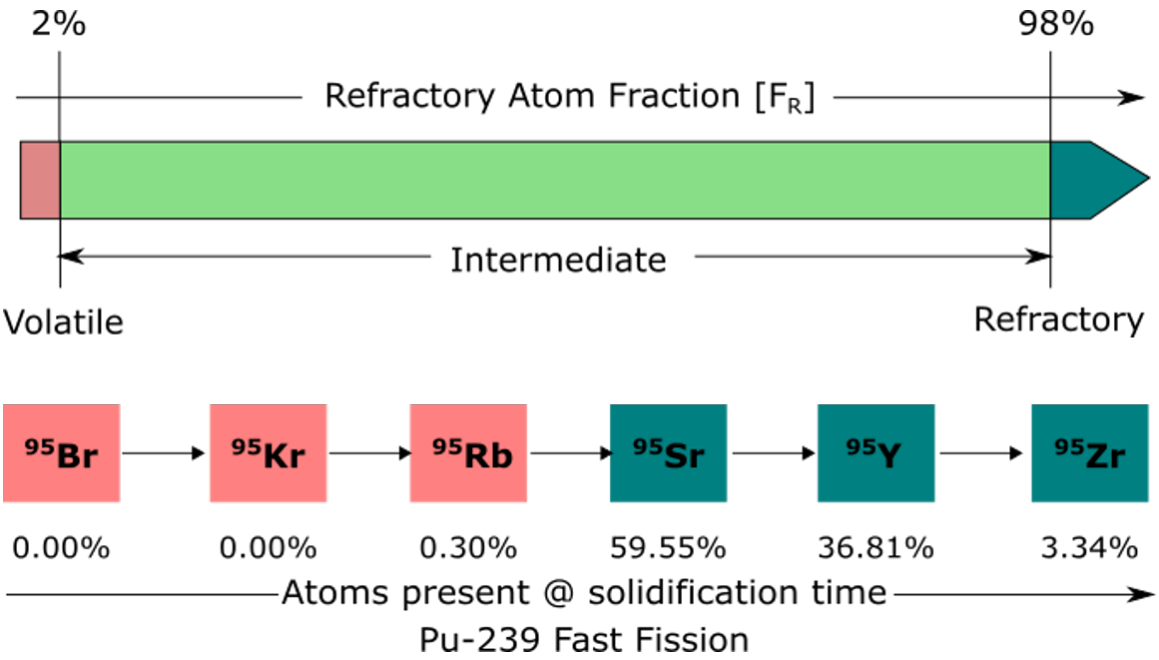


Figure 3.5: Freiling ratio bounds and mass chain 95 which is considered pure refractory.

Computational methods for fractionation were developed using the ORIGEN code. ORIGEN has the capability to output the isotope inventory of gamma ray emitters. A Freiling ratio can be set ($F_R$) or calculated for each photon energy group. The formulation for the $r_{i,R}$ and Freiling ratio is shown below in Eq. 3.12.

$$\begin{aligned} F_R &= \frac{atoms_i}{atoms_i^{total}} \\ r_{i,R} &= \frac{Fissions_i}{Fissions_R} = \frac{\frac{a_i}{Y_i}}{\frac{a_R}{Y_R}} \end{aligned} \tag{3.12}$$

where:

$atoms_i$ atoms of mass chain $i$ volume distributed at solidification time

$atoms_i^{total}$ total atoms in mass chain $i$

$Fissions_i$ is the number of fissions producing isotope i

$a_i$ is the number of atoms of isotope i

$Y_i$ is the cumulative fission yield of isotope i in mass chain

R subscripts indicate purely refractory mass chain

Typically, $F_R$ is dependent on fuel type, carrier solidification temperature, and time which is determined by yield of the device. A mass chain that has an $F_R$ value higher than 0.98 is referred to as refractory while lower than 0.02 is known as volatile. Values between these two bounds are defined as mixed chains [26]. Fig. 3.5 demonstrates the definition of $F_R$ or the fractional amount of the mass chain which is refractory. Mass chain 95 is considered purely refractory as 99.7$\%$ of the mass chain is refractory at the time of solidification.

Because of the different elemental condensation temperatures, particles are volume or surface distributed throughout or on the carrier material. Particle size was found to follow a lognormal distribution from early above ground nuclear testing. The distribution is shown

below [26].

$$N(r) = \frac{N_t}{(2\pi^{1/2})\beta r} e^{-\frac{1}{2}[\frac{ln(r)-\alpha_0}{\beta}]^2} \tag{3.13}$$

where:

$N(r)$ is the number of particles of radius r

$N_t$ is the total number of particles

$\alpha_0$ is the natural logarithm of median radius

$\beta$ is the logarithmic standard deviation

The volumetric and surface activity-size distributions also follow a lognormal distribution through higher moments of the lognormal function which is conveniently another lognormal function shown below. The surface distribution follows the same lognormal distribution but is represented by the $2^{nd}$ moment of the lognormal distribution or $\alpha_2 = \alpha_0 + 2\beta^2$.

$$A_v(r) = \frac{f_v A_t}{(2\pi^{1/2})\beta r} e^{-\frac{1}{2}[\frac{ln(r)-\alpha_3}{\beta}]^2} \tag{3.14}$$

where:

$\alpha_3 = \alpha_0 + 3\beta^2$ or 3rd moment of the lognormal distribution

$f_v$ is the fraction of activity volumetrically distributed

These relationships [26] were used to volumetrically or surface distribute the ORIGEN gamma inventory or determine the $F_R$ for each gamma energy bin. Monte Carlo based SA was used to determine the sensitivities of $F_R$. The $r_{V,R}$ value was also set to mimic a location in the fallout field and corresponding gamma spectrum. This method is fully described in section 3.3.5.

Different fractionation samples were also generated and used to calculate time and energy dependent total/first-order sensitivity indices. Freiling determined chemical fraction-

ation is modeled with a logarithmic relationship found in Eq. 3.15.

$$\begin{aligned} &\ln(r_{i,R}) = a_i + (1 - b_i)\ln(r_{V,R}) \\ &\text{where} \\ &a_i = 0; \\ &b_i = \sqrt{F_R}; \\ &\text{substituting and yielding:} \\ &r_{i,R} = (r_{v,R})^{1-\sqrt{F_R(i)}} \end{aligned} \tag{3.15}$$

Using the formulation in Eq. 3.15, $r_{i,R}$ values can be calculated for each mass chain by setting $r_{V,R}$. Values considered in this research were $r_{V,R} = 0.1$, 0.2, and 0.5. The range of values chosen was due to the short time scale. A $r_{V,R}$ value of 0.1 is considered highly refractory and would be found closer to ground zero while 0.5 is considered volatile. Each isotope constituent of mass chain $i$, was multiplied by the corresponding $r_{i,R}$ value for mass chain $i$. This method yields a "fractionated" sample for a total/first-order sensitivity indices calculation. The high temperatures during the prompt front-end time period require use of the unfractionated sample total/first-order sensitivity indices. Although, use of the total/first-order sensitivity indices for fractionated samples provide insight into delayed variable sensitivities focusing field collection methods.

Importantly, the derived unfractionated sample relationships developed from this simplified model accelerates the MCF calculation. Without prior relationships, the MCF variable sample space is large which requires many samples to adequately cover the sample space. Consequently, the high amount of samples does not guarantee the actual configuration to be represented. Using the point-source model relationships allows the uncertainty in the sample space to shrink which increases the likelihood of the true configuration to be represented and sampled.

### 3.3.2 Peri-Detonation Monte Carlo Filtering Acceleration Scheme – Section (i)

The acceleration scheme is developed from analysis of the point-source SA results that include the detector response and integral counts between 1.00E-05 and 1.00E-01 seconds. Integral counts and detector response functions created a more realistic representation of the data. Notably, nuclear data uncertainties were not considered because each data point would require hundreds of runs to quantify the total uncertainty in just one data point. The acceleration scheme, while crude, highlights the effect of inputting known distributions into a predictive algorithm. Noteworthy, yield information can be obtained from other sources, but for the sake of this research, an acceleration scheme was not developed for yield or blast energy information. While global sensitivity analysis methods reveal more information on variable behavior, local methods were used for acceleration development because of smaller computation times.

Regression analysis, related to local sensitivity methods/metrics, applied to the detector response and integrated counts between 1.00E-05 and 1.00E-01 seconds allowed for determination of the MCF acceleration relationships. This method was completed by applying a linear fit over all possible energy ratios (independent variable) versus the fractional mass (dependent variable) and maximizing the resulting correlation coefficient. To complement the regression analysis, a fractional "purity" metric was developed for each energy range and nuclide shown in Eq. 3.16. This trend coupled with calculation of the correlation coefficients allowed development of the MCF relationships.

$$S^k_{Purity} = \frac{S^k_i}{|S^k_T - S^k_i|} \tag{3.16}$$

where:

$S^k_{Purity}$ is the purity metric for nuclide $k$,

$S^k_i$ is the main effect sensitivity index for nuclide $k$,

$S^k_T$ is the total sensitivity index for nuclide $k$,

$|S^k_T - S^k_i|$ is the interaction amount of nuclide $k$ with other variables.

The top energy ranges were chosen by eliminating energy ranges with high computational uncertainty ($>$ 3 MeV), energies lower than 100 keV which natural background and electronic noise affect, and energies around 511 keV which is the energy associated with positron annihilation. Once these constraints were applied, the purity values combined with the correlation coefficients indicated which energy ratios were the most effective in determining rapid fuel-type estimation.

### 3.3.3 Peri-Detonation Front-End Time Period – Section (ii)

The importance of the Section (ii) calculation stems from the device emitting characteristic signatures being still mostly an intact configuration. Analysis of these components following detonation become more challenging when particle collection is involved. Prompt signatures originating from the fuel and other structural components are highly dependent on the configuration due to photon/neutron leakage which can provide insight into sophistication. Later peri-detonation emissions following the disassembly can also provide insight into sophistication.

The prompt front-end curve highlights the prompt hypothetical unboosted fission and activation photons emitted during the Gaussian shaped power excursion. These photons were generated using the 1-D Criticality Safety Analysis Sequences (CSAS) within the Scale 6.2 package. Importantly, the CSAS module outputs photon/neutron leakage values which are transported to the problem boundary and used to determine a detector response. This module uses the XSDRNPM for cross-section weighting/collapsing and determination of the neutron multiplication factor ($k_{eff}$) in 1-D spherical coordinates. XSDRNPM is a 1-D discrete-ordinates transport code. This research employed the ENDF/B-VII.1 coupled 200 neutron and 47 gamma group cross-section library. Inputs into the CSAS module were fuel/reflector type, mass, and density. These inputs dictate the energy output/physics within the system inherently affecting the photon spectrum. From the CSAS output, the

Rossi alpha and total energy output (device yield) were calculated for development of the power curve and ORIGEN irradiation.

*Rossi Alpha and Total Energy Output*

Passive emission magnitudes are determined from physical properties and design specifications. To replace hydrodynamic calculations and generate a realistic emission profile, a simplified reactor accident relationship is used along with the prompt Rossi alpha constant. These values are calculated from the 1-D spherical transport calculation results. Furthermore, the hypothetical prompt emission curve width is held constant assuming a symmetric - Gaussian - burnup profile while the magnitude increases or decreases according to the Rossi alpha constant.

The Rossi alpha constant is dependent on several system properties and determines the speed and magnitude of the reaction or energy output ultimately dictating the passively measurable signature magnitude and profile. Beginning with the point reactor kinetics equation for neutron density in Eq. 3.17a, the prompt Rossi alpha, $\alpha_p$, can be derived when delayed neutrons are neglected.

$$\frac{d\hat{n}}{dt} = \frac{\rho - \beta}{l}\hat{n}(t) + \sum_{i=1,6} \lambda c_i; \tag{3.17a}$$

where:

$$\rho = \frac{(k_{eff} - 1)}{k_{eff}}; \beta \equiv \text{Delayed neutron fraction;} \tag{3.17b}$$

$$l = \frac{k_{eff}}{l_0}; l \equiv \text{Mean generation time; } l_0 \equiv \text{Prompt neutron lifetime;} \tag{3.17c}$$

neglecting delayed neutrons yields:

$$\frac{d\hat{n}}{dt} = \frac{\rho}{l}\hat{n}(t) \tag{3.17d}$$

substituting above definitions:

$$\frac{d\hat{n}}{dt} = \frac{k_{eff} - 1}{l_0}\hat{n}(t) \tag{3.17e}$$

gives the solution:

$$\hat{n}(t) = \hat{n}_0 \exp[\frac{k_{eff} - 1}{l_0}t]; \text{where } \frac{k_{eff} - 1}{l_0} \equiv \alpha_p \text{ (Prompt Rossi Alpha)} \tag{3.17f}$$

The above equation is expressed in terms of power due to the time dependence of neutron density on the system mean fission cross-section [27]. The Rossi alpha value is directly related to the sophistication or design level of the device as it ultimately dictates burnup with the exponential rise in power. Modeling the exponential power rise offers the researcher with a simplified emission profile, which affects time-dependent detection limits and sensitivity indices.

Modeling hydrodynamic phenomena, such as pressure and density changes within the core, are neglected. Avoiding complex hydrodynamics has multiple benefits mainly reducing computation time. Spatial density, temperature, and pressure changes inherently change the Rossi alpha value. A symmetric constant width Gaussian burnup/emission profile is assumed. The calculated Rossi alpha value determines the magnitude of the constant width Gaussian profile. To fix the width (burn time) of the Gaussian, the time upper bound of the power curve is set to one-microsecond (1.00E-06 seconds) giving a $\mu$ value of 5.00E-07 seconds or when the max power emission occurs. The standard deviation, $\sigma$, is calculated to be 5.00E-08 seconds by Eq. 3.18.

$$\begin{aligned} \mu + 20\sigma &= t_{stop} \\ \mu - 20\sigma &= 0 \\ t_{stop} &= 1.00x10^{-6} seconds \end{aligned} \tag{3.18}$$

Next, the total energy output is calculated using Eq. 3.19. This equation provides the basis

of emission magnitudes as the emission width is fixed to 1.00E-06 seconds.

$$E \propto \frac{(\delta\rho)^3 R^2}{l^2} \tag{3.19}$$

where:

$E$ is the total energy output

$R$ is the core radius

$l$ is the prompt neutron lifetime

$\delta\rho$ is the reactivity change or $\frac{k_{effective}-1.0}{k_{effective}}$

For severe reactor accidents, Eq. 3.19 stems from the pressure in the core being proportional to the total energy output. The pressure gradient produced causes the assembly to expand eventually causing the reaction to stop. This happens when $\frac{r_t}{R_{initial}} \propto \delta\rho$ at which the total energy output is found in Eq. 3.19 [28]. The prompt burnup power curve is formulated from this simplified equation.

Integrating the Gaussian power curve yields the total energy output from Eq. 3.19. The Gaussian is the probability density function (PDF) of the power in the system. Setting the integral of a PDF equal to the total energy output allows for the power curve to be formulated. This is possible because the $\mu$ and $\sigma$ values were set previously. Eq. 3.20 shows the PDF and cumulative distribution functions (CDF).

$$\begin{aligned} P(t) &= \frac{1}{\sigma\sqrt{2\pi}} e^{\frac{-(t-\mu)^2}{2\sigma^2}} \\ \int_0^{1.00x10^{-6}} P(t)dt &= E_{total} \\ C(t) &= \frac{1}{2}(1 + erf[\frac{t-\mu}{\sigma\sqrt{2}}]) \end{aligned} \tag{3.20}$$

The cumulative distribution function (Eq. 3.20) is set to the total energy output. Estimating the derivative, $\frac{dE}{dt}$ or power, yields the power curve desired for simulations. For illustration, a 1 kiloton (kt) - 4.18E+12 Joules - blast equivalent is shown below in Figs. 3.6 and 3.7.

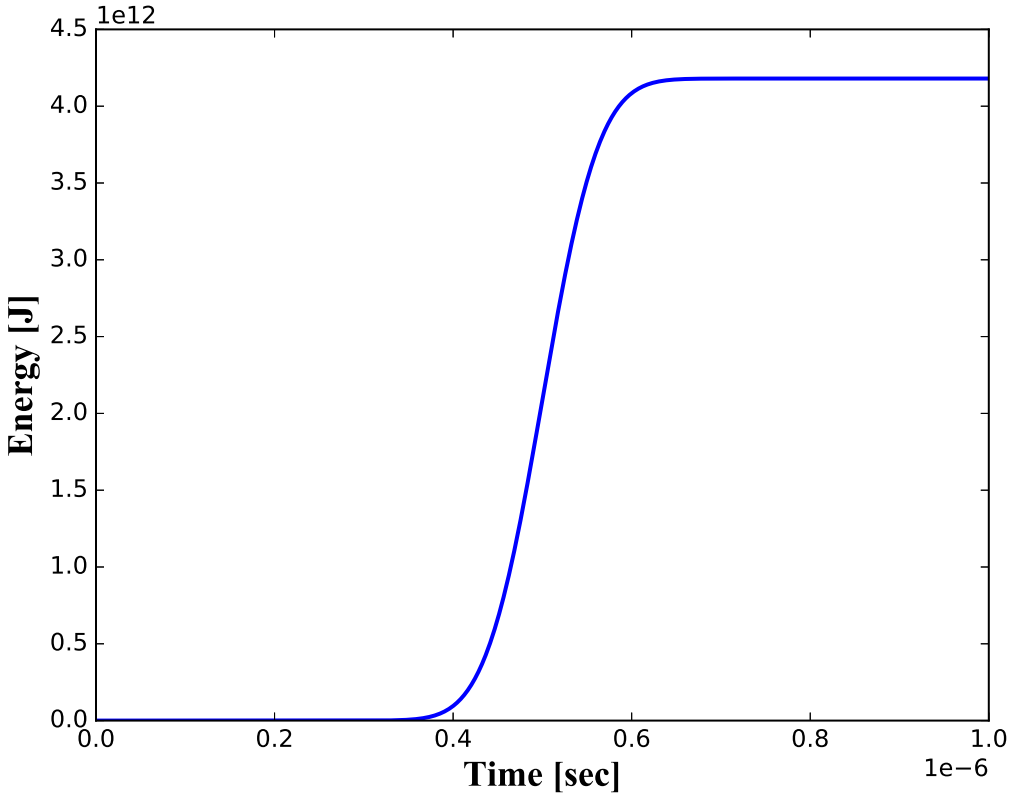


Figure 3.6: Cumulative distribution function of energy output from 1 kt blast.

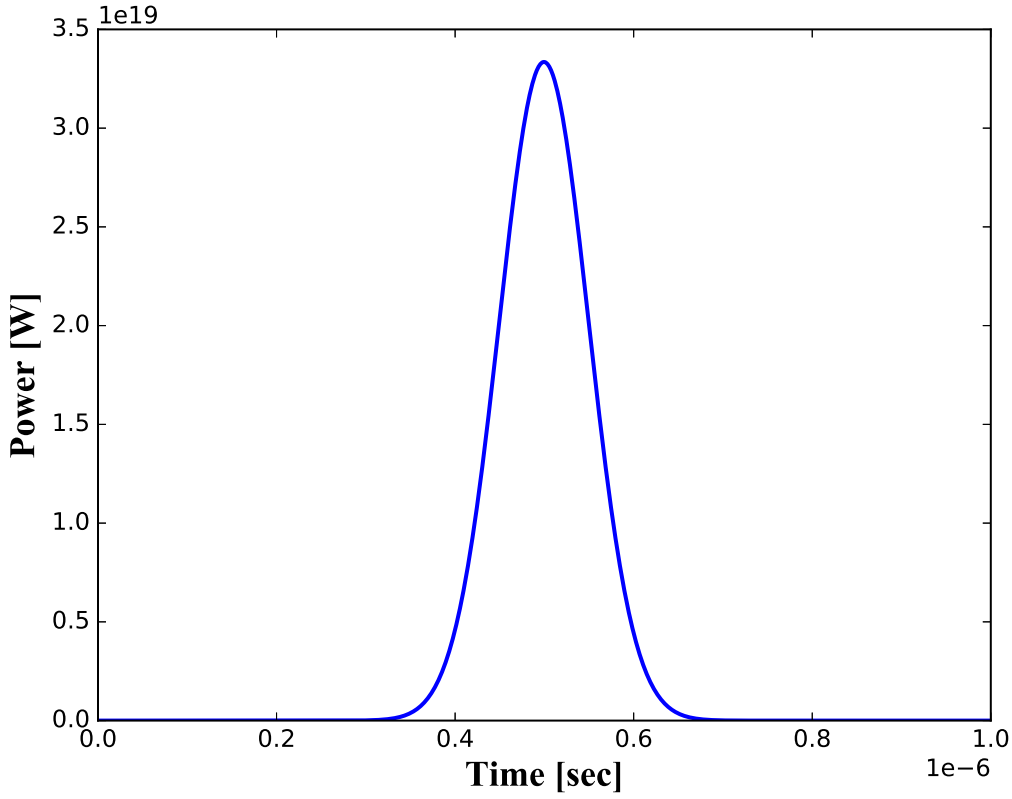


Figure 3.7: Formulated power curve probability density function from 1 kt blast.

These power curve formulations/simplifications side-step hydrodynamic calculations offering computational speed-up and removal of potential sensitivities. Once the photons have been generated, scaled to the power, and transported to the boundary of the problem, a detector response function is used to generate the photon spectrum.

*Detector Response*

Applying detector responses to the generated photon emissions provides a realistic representation of detection capabilities/limitations and the effects on data quality and availability. Detector response functions were generated using the Monte Carlo N-Particle Transport (MCNP) 6.1 code package. The $LaBr_3$(Ce) detector response was modeled after the detector used in the experimental portion of this research. The radius and height of the modeled detector was 3.81 centimeters (cm). No secondary components of the detection system

were modeled. Because of the timing importance, the same integration time employed in the experimental portion was used to realistically model the pulse collection limitations of the detector. The inverse of integration time, $\frac{pulses}{second}$, was taken as the upper rate limit the detector was capable of handling at each time step. The decay time used was 0.016 microseconds, based off Saint Gobain's $LaBr_3$(Ce) properties [29]. This number was increased by a factor of 10 to incorporate pulse decay times. To incorporate baseline determination and the pulse rise time, the number was further increased by 20 nanoseconds yielding a total integration time of 180 nanoseconds. The 47-group photon energy structure was used for calculating the detector response. The photon energy group structure is shown below in Table 3.4 and an unnormalized comparison is shown in Figure 3.9.

Table 3.4: ENDF/B-VII.1 47 group photon energy bounds used for sensitivity analysis.

| Energy Bounds [MeV] | Group Number | Energy Bounds [MeV] | Group Number |
|---|---|---|---|
| 2.000E+01 - 1.400E+01 | G1 | 1.400E+01 - 1.200E+01 | G2 |
| 1.200E+01 - 1.000E+01 | G3 | 1.000E+01 - 8.000E+00 | G4 |
| 8.000E+00 - 7.500E+00 | G5 | 7.500E+00 - 7.000E+00 | G6 |
| 7.000E+00 - 6.500E+00 | G7 | 6.500E+00 - 6.000E+00 | G8 |
| 6.000E+00 - 5.500E+00 | G9 | 5.500E+00 - 5.000E+00 | G10 |
| 5.000E+00 - 4.500E+00 | G11 | 4.500E+00 - 4.000E+00 | G12 |
| 4.000E+00 - 3.500E+00 | G13 | 3.500E+00 - 3.000E+00 | G14 |
| 3.000E+00 - 2.750E+00 | G15 | 2.750E+00 - 2.500E+00 | G16 |
| 2.500E+00 - 2.350E+00 | G17 | 2.350E+00 - 2.150E+00 | G18 |
| 2.150E+00 - 2.000E+00 | G19 | 2.000E+00 - 1.800E+00 | G20 |
| 1.800E+00 - 1.660E+00 | G21 | 1.660E+00 - 1.570E+00 | G22 |
| 1.570E+00 - 1.500E+00 | G23 | 1.500E+00 - 1.440E+00 | G24 |
| 1.440E+00 - 1.330E+00 | G25 | 1.330E+00 - 1.200E+00 | G26 |
| 1.200E+00 - 1.000E+00 | G27 | 1.000E+00 - 9.000E-01 | G28 |
| 9.000E-01 - 8.000E-01 | G29 | 8.000E-01 - 7.000E-01 | G30 |
| 7.000E-01 - 6.000E-01 | G31 | 6.000E-01 - 5.120E-01 | G32 |
| 5.120E-01 - 5.100E-01 | G33 | 5.100E-01 - 4.500E-01 | G34 |
| 4.500E-01 - 4.000E-01 | G35 | 4.000E-01 - 3.000E-01 | G36 |
| 3.000E-01 - 2.600E-01 | G37 | 2.600E-01 - 2.000E-01 | G38 |
| 2.000E-01 - 1.500E-01 | G39 | 1.500E-01 - 1.000E-01 | G40 |
| 1.000E-01 - 7.500E-02 | G41 | 7.500E-02 - 7.000E-02 | G42 |
| 7.000E-02 - 6.000E-02 | G43 | 6.000E-02 - 4.500E-02 | G44 |
| 4.500E-02 - 3.000E-02 | G45 | 3.000E-02 - 2.000E-02 | G46 |
| 2.000E-02 - 1.000E-02 | G47 | | |

Fundamentally, photon detection requires the photon to interact in the detection medium whether inorganic, organic, or a semiconductor. The detection is determined by the properties of the detection medium. Because photons are electromagnetic radiation, they readily interact with negatively charged electrons. For photons, high-Z material increases the probability for interaction due to the increased electron density. Detection is possible because the photon transfers energy to an electron. The electron ionization produces more electrons from atomic collisions which is detectable by charge collection [30]. The relevant photon interactions to detection are: photoelectric absorption, Compton scattering, and pair production. Photoelectric absorption is the most desired as all of the photon's energy is deposited into the detector leading to distinct full energy peaks. Compton scattering within the detection medium produces less distinct peaks as energy is only partially deposited. The photoelectric absorption, Compton scatter, and pair production photon interaction cross sections are found in Fig. 3.8 for the $LaBr_3$(Ce) detector.

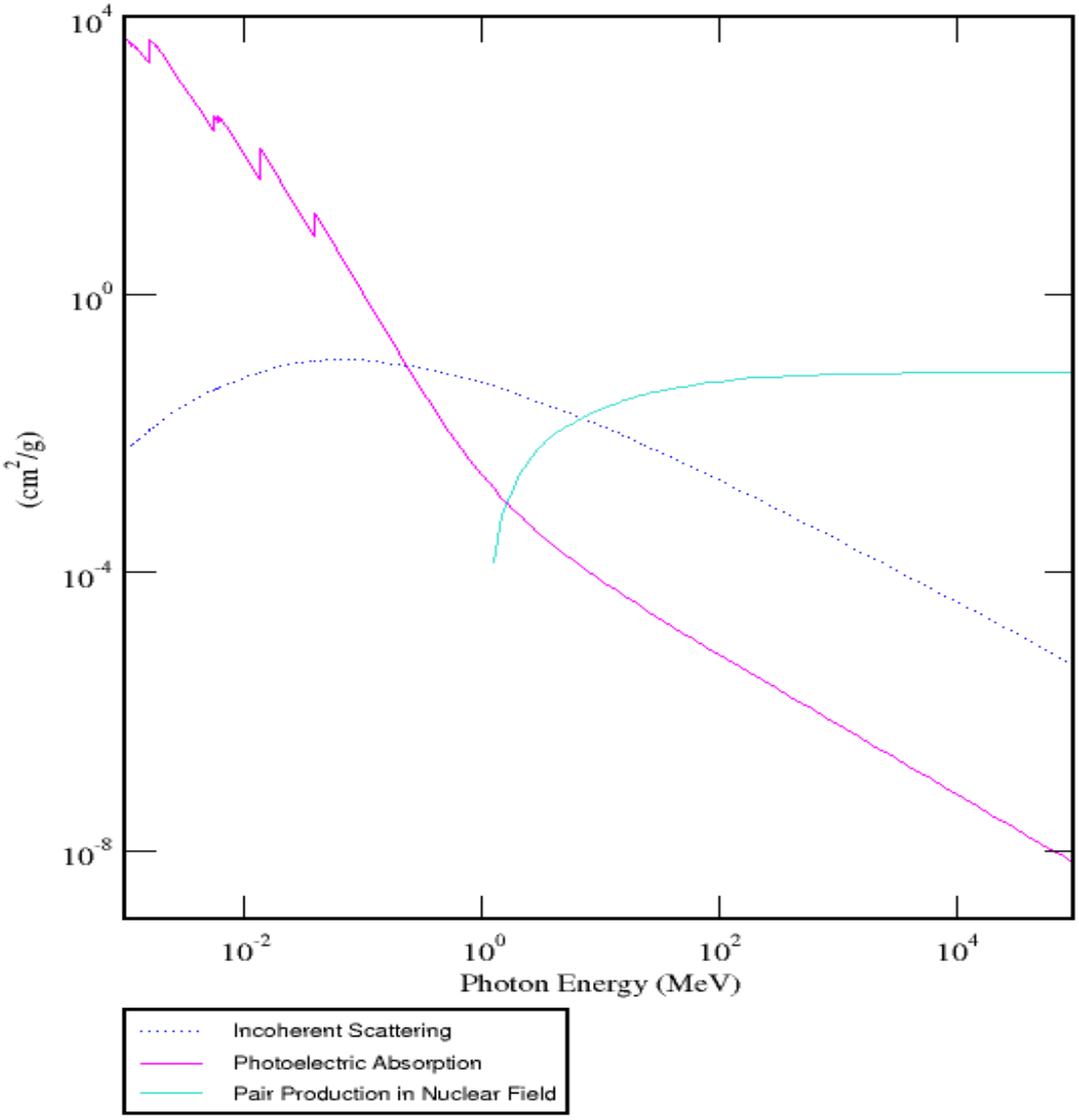


Figure 3.8: $LaBr_3(Ce)$ photon interaction cross sections for photoelectric absorption, Compton scattering, and pair production. Generated from National Institute of Standards and Technology (NIST) photon cross-section database (XCOM) [31].

MCNP mimics detection physics by Monte Carlo random number sampling to statistically buildup/converge a reaction rate or pulse height within the detector volume. The total detector response is found below in Eq. 3.21 [23]. The MCNP pulse height tally provides a physical analog to pulses created in a detector volume through random number

sampling. Once the energies have been discretized to the 47-group structure, the total energy deposition in the detector volume can be determined by aggregating all tracks within the volume of a generated particle. Simply, the pulse height tally creates an energy distribution of pulses occurring within the detector volume. Particles were simulated across each energy range within the 47-group structure impinging on the detector volume. Each generated source particle energy range creates a distribution of pulses in other energy ranges producing a pulse distribution for each 47-group energy range.

$$R = \int_{V_d} \int_{E} \sigma_d(\vec{r}, E)\phi(\vec{r}, E) dE dV \tag{3.21}$$

where:

$R$ is the total detector response

$\phi$ is the scalar flux,

$\sigma_d$ is the desired detector response function

Figure 3.9 shows a raw photon spectrum and a photon spectrum with an applied detector response function at 1.00E-06 seconds following detonation. This time is dominated by photons originating from early-time fission products. Applying detector response functions to SA analyses are meant to highlight the effect on the sensitivity indices or variable importance and additionally providing a more realistic treatment of phenomena generating more relevant sensitivity indices.

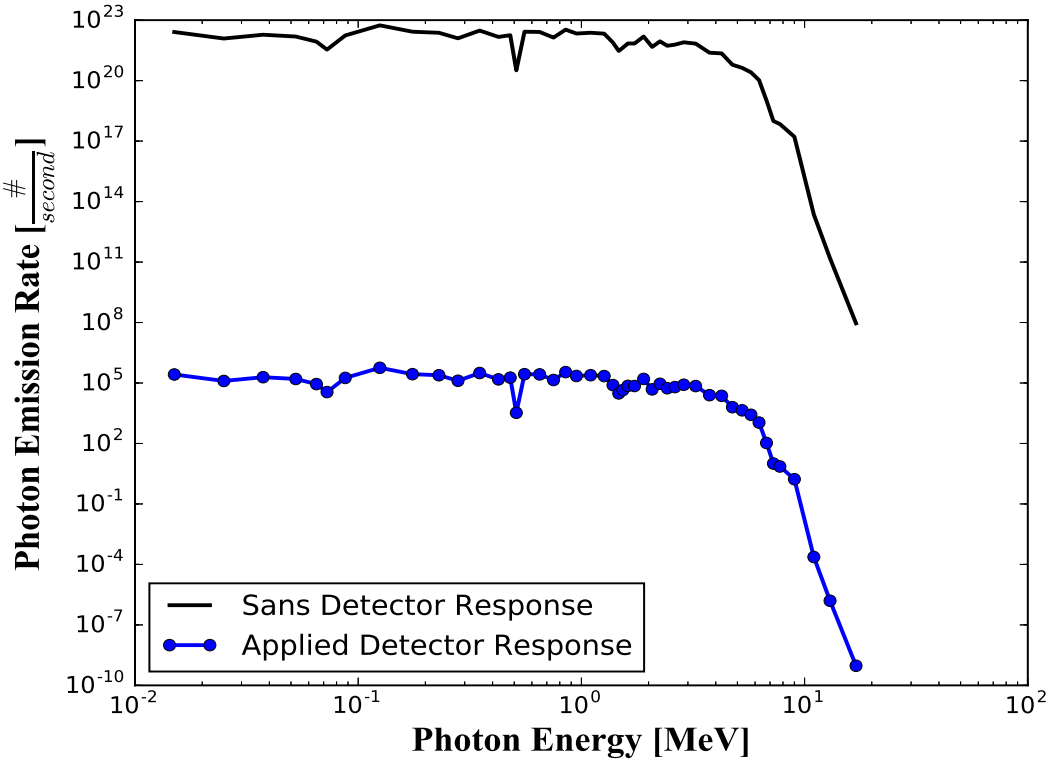


Figure 3.9: Comparison of photon spectra with and without application of detector response function.

Towards the end of the Gaussian emission curve, fission product photon emission dominates the prompt photons marking the start of prompt back-end time period. Noteworthy, delayed neutrons are present in the nuclear cloud creating secondary photon reactions that contribute to the total photon signal in the back-end period or Sections (iii) - (v).

### 3.3.4 Peri-Detonation Back-End Time Period Photon Production – Section (iii)

Completion of the CSAS module for front-end photon emission signals the back-end sequences to begin. ORIGEN point source neutron and photon spectra are generated and stored for injection into a 1-D volumetric source problem. Prior to the volumetric calculation, a system of ordinary differential equations (ODE) are solved to produce material compositions/densities, temperatures, and nuclear cloud dimensions which serves as the

1-D geometry and material specifications.

The 1-D transport calculation provides the basis input settings for back-end photon production. These calculated constants and distributions are fed into the ORIGEN point source model which yield photon and neutron sources from the calculated time-dependent nuclide concentrations. Specifically, the power curve/distribution, fuels, and masses obtained from the CSAS 1-D model output were used in the ORIGEN depletion sequence outputting time and energy dependent nuclide inventories, photon and neutron spectra. These spectra are highly important for secondary reactions, attenuation, and propagation through the nuclear cloud which ultimately affects detectability of nuclear cloud signatures.

ORIGEN determines time dependent nuclide concentrations with the associated radiation source terms which determines emission detectability. The time rate of change of a nuclide, $N_i$ is shown in Eq. 3.22 below [23].

$$\frac{dN_i}{dt} = \sum_{j=1}^{m} l_{ij}\lambda_j N_j + \bar{\phi}\sum_{k=1}^{m} f_{ik}\sigma_k N_k - (\lambda_i + \bar{\phi}\sigma_i)N_i, (i\text{=}1,...,\text{m}),$$

where:

$N_i =$ atom density of nuclide, $i$,

$\lambda_i =$ disintegration constant of nuclide, $i$,

$\sigma_i =$ spectrum-averaged neutron absorption cross section of nuclide, $i$,

$\bar{\phi} =$ space and energy averaged neutron flux,

$l_{ij} =$ decay branching fractions for nuclide, $i$, from other nuclides, $j$,

$f_{ik} =$ branching fractions for neutron absorption by other nuclides, $k$, that form species $i$. (3.22)

The time dependent nuclide concentrations yield the desired emissions for use in the 1-D volumetric calculation. Source magnitudes generated from the ORIGEN calculation are inserted into the 1-D volumetric source problem.

### 3.3.5 Peri-Detonation Nuclear Cloud Rise – Sections (iv-v)

The time-dependent neutron and photon spectra generated from Section (iii) are stored and injected into a CSAS volumetric source problem. For time-dependent dimensions, temperatures, and material specifications used in the volumetric source problem, a simplified DELFIC model was developed for determination of urban environment mass entrainment and radial dimension using equations in Section 3.3.5 up to 1 minute after detonation. Modeling urban debris uptake in a nuclear detonation is necessary because of photon attenuation and subsequent activation resulting from the delayed neutrons present in the nuclear cloud; all of which, contribute and create noise in the total photon signal.

*Peri-Detonation Nuclear Cloud Rise and Mass Entrainment [32]*

The Defense Land Fallout Interpretive Code (DELFIC) was developed by several contributors under the Department of Defense. This code is used for research and prediction of local fallout from a nuclear detonation commencing once the fireball pressure equals the atmospheric pressure. The nuclear cloud is treated as a bubble of hot air entrained with water and ground material. For the purposes of this research, the neutron and gamma source is distributed uniformly through the nuclear cloud. Debris masses, densities, temperatures, and cloud dimensions are found using the following set of ordinary differential equations (ODE) segregated into "wet" and "dry" equations or when water is condensed and not condensed, respectively.

**Base Equations**

Momentum

$$\frac{du}{dt} = (\frac{T^*}{T_e^*}\beta' - 1)g - (\frac{2k_2 v T^* \beta'}{H_c T_e^*} + \frac{1}{m}\frac{dm}{dt})u;$$

Cloud Center Height

$$\frac{dz}{dt} = u;$$

Net Mass Change (3.23)

$$\frac{dm}{dt} = \frac{dm_{ent}}{dt} - F;$$

Kinetic Energy Density

$$\frac{dE}{dt} = \frac{2k_2 T^* \beta' u^2 v}{T_e^* H_c} + \frac{u^2}{2}\frac{dm_{ent}}{mdt} - E\frac{dm_{ent}}{mdt} - \epsilon;$$

Soil Mass Mixing Ratio

$$\frac{ds}{dt} = -\frac{1}{\beta'}\frac{1+x}{1+x_e}s\frac{1}{m}\frac{dm_{ent}}{dt} - \frac{1+x+s+w}{m}\frac{s}{s+w}F;$$

DELFIC treats nuclear cloud rise as an entraining buoyant hot mass of air that is intermixed with soil particles. The momentum balance equation is meant to provide the cloud's center rate of rise through calculation of its acceleration [33]. After the initial soil, water, and air masses entrained in the cloud are determined, their respective mass mixing ratio equations are solved, ultimately yielding time-dependent densities for the 1-D volumetric source problem. The time-dependent soil, water, and air masses affect the buoyancy, trajectory, and temperature of the cloud. The temperature equation is obtained from an enthalpy balance because entrainment is a constant pressure process. The time-dependent temperature provides a switch for using the dry and wet equations and is important in fractionation of the device debris [33]. Temperature is also used in the 1-D volumetric source problem.

**Dry Equations**

Temperature

$$\frac{dT}{dt} = -\frac{\beta'}{\bar{c}_p(T)}\Big[\frac{T^*}{T_e^*}gu + \Big(\int_{T_e}^{T} c_{pa}(T)dT\Big)\frac{1}{\beta' m}\frac{dm_{ent}}{dt} - \epsilon\Big];$$

Mass Entrainment

$$\frac{dm_{ent}}{dt} = \frac{\beta' m}{1 - \frac{\beta'}{T^*\bar{c}_p}\int_{T_e}^{T} c_{pa}(T)dT}\Big\{\frac{S\mu v}{V} + \frac{\beta'}{T^*\bar{c}_p}\Big[\frac{T^*}{T_e^*}gu = \epsilon\Big] - \frac{gu}{R_a T_e^*}\Big\};$$

Kinetic Energy Density

$$\frac{dE}{dt} = \frac{2k_2 T^*\beta' u^2 v}{T_e^* H_c} + \frac{u^2}{2}\frac{dm_{ent}}{mdt} - E\frac{dm_{ent}}{mdt} - \epsilon;$$

Water Vapor Mixing Ratio

$$\frac{dx}{dt} = -\frac{1 + x + s}{1 + x_e}\Big(x - x_e\Big)\frac{1}{m}\frac{dm_{ent}}{dt};$$

Condensed Water Mixing Ratio

$$\frac{dw}{dt} = 0;$$

(3.24)

**Wet Equations**

Temperature

$$\frac{dT}{dt} = -\frac{\beta'}{1 + \frac{L^2 x\xi}{c_p R_a T^2}}\Big[\Big(\big(T - T_e\big) + \frac{L(x - x_e)}{c_p}\Big)\frac{1}{m\beta'}\frac{dm_{ent}}{dt} + \frac{T^*}{T_e^*}\frac{g}{c_p}u\Big(1 + \frac{Lx}{R_a T}\Big) - \frac{\epsilon}{c_p}\Big];$$

Mass Entrainment

$$\frac{dm_{ent}}{dt} = \frac{\beta' m}{1 - \frac{1}{T^*}\Big[\frac{\beta'}{1 + \frac{L^2 x\xi}{c_p R_a T^2}}\Big]\Big[T - T_e + \frac{L(x - x_e)}{c_p}\Big]}\Big\{\frac{S\mu v}{V} + \frac{\beta'}{T^*(1 + \frac{L^2 x\xi}{c_p R_a T^2})}\Big[\frac{guT^*}{T_e^* c_p}(1 + \frac{Lx}{R_a T}) - \frac{\epsilon}{c_p}\Big] - \frac{gu}{R_a T_e^*}\Big\};$$

Water Vapor Mixing Ratio

$$\frac{1}{x}\frac{dx}{dt} = \big(1 + \frac{x}{\xi}\big)\frac{L\xi}{R_a T^2}\frac{dT}{dt} + \big(1 + \frac{x}{\xi}\big)\frac{gu}{R_a T_e^*};$$

Condensed Water Mixing Ratio

$$\frac{dw}{dt} = -\frac{1}{\beta'}\big(\frac{1 + x}{1 + x_e}\big)\big(w + x - x_e\big)\frac{1}{m}\frac{dm_{ent}}{dt} - \frac{dx}{dt}$$

(3.25)

Dry equations are used prior to water saturation which means no water mass is lost to condensation. Conversely, the wet equations are used once the water has saturated and is lost

to condensation. Further explanation of constants, empirical equations, and initial conditions can be found in the DELFIC fundamentals manual or Refs. [32] and [33]. Definitions are found at the end of this section. Solving the above system of ODEs yields material compositions, temperatures, densities, and dimensions of the nuclear cloud. Notably, the material density is calculated from the time-dependent soil/water/air mixing ratios and the nuclear cloud total mass resulting from the mass entrainment equations.

**Definitions**

$W =$ Device yield;

$$q(x) = \frac{1 + \frac{x}{\xi}}{1 + x};$$

$$q_e(x) = \frac{1 + \frac{x_e}{\xi}}{1 + x_e};$$

$$T^* = Tq(x);$$

$$T_e^* = Tq_e(x);$$

$$\beta' = \frac{1 + x}{1 + x + s + w};$$

$$g = 9.8\frac{m}{s^2};$$

$$k_2 = max\big[0.004, min(0.1, 0.1E^{-\frac{1}{3}})\big];$$

$$v = max(u, \sqrt{2E});$$

$$z' = z_0 - \frac{H_{c0}}{\mu};$$

$$H_c = \mu(z - z');$$

$$\epsilon = \frac{0.175(2E)^{\frac{3}{2}}}{H_c};$$

$$\bar{c}_p = \beta c_p(T) + (1 - \beta')c_s(T)\frac{Joules}{kg - K};$$

$$c_p(T) = \frac{c_{pa}(T) + xc_{pw}(T)}{1 + x}\frac{Joules}{kg - K};$$

$$c_{pa} = \frac{Joules}{kg - K}\text{Specific heat of dry air at constant pressure;}$$

$$c_{pw} = \frac{Joules}{kg - K}\text{Specific heat of water vapor at constant pressure;}$$

$$c_s = \frac{Joules}{kg - K}\text{Specific heat of soil at constant pressure;}$$

$$\mu = max\big[max(0.12, 0.1W^{0.1}), 0.01W^{\frac{1}{3}}\big];$$

$$R_a = 287.0\frac{Joules}{kg - K};$$

$$L = 2.5E + 06/2.83E + 06\frac{Joules}{kg}\text{Latent heat of vaporization of water or ice;}$$

$$\xi = \frac{18}{29};$$

(3.26)

The system of ODEs is solved for temperature, cloud dimensions, material compositions, and cloud density between 3 and 60 seconds. The generated photon source is then inserted into a 1-D transport code with the calculated DELFIC factors. Each of these fac-

tors affect propagation/absorption of passively measurable signatures within the nuclear cloud. The behavior within the cloud determines what is available for detection placing limitations on conclusions.

Once the 1-D volumetric calculation is run using DELFIC calculated values, the energy- and time-dependent photon fluxes are gathered at the boundary. These fluxes are scaled down to the detector geometry and a detector response function, discussed earlier, is applied.

The randomly generated spectra from the prompt front-end and back-end time period are then compared to the reference Fat Man and Little Boy spectra. The process is then repeated N times and the resulting "passed" configurations are post-processed which yield configuration distributions (i.e. masses, fuels, height-of-burst, etc.) with associated uncertainties.

### 3.4 Peri-Detonation Sensitivity/Uncertainty Analysis Results

Traditional post-detonation nuclear forensic science contains many limiting factors that affect timely decisions. The relevance of the science contributing to actionable nuclear information at early-times is a debated issue [12]. Computational and experimental peri-detonation analyses of passively measurable signatures may contribute to early-time nuclear information following a domestic nuclear detonation.

The complexity of peri-detonation nuclear forensics requires SA to sort through noisy data which can obscure subtle characteristics. Local, global variance reduction, and MCF methods were combined to illustrate application versatility and accuracy/precision. A combination of local and global sensitivity methods were completed on an ORIGEN generated point-source model for MCF acceleration.

### 3.4.1 Peri-Detonation Uncertainty Analysis Results

Computational modeling errors fundamentally display how much the answer fluctuates. In this case, the uncertainty causes fluctuations in the photon emissions which are used for inferring characteristics of the detonation. The error magnitude is inversely proportional to conclusion confidence; i.e., high error produces low confidence. The photon emission uncertainty considered in this research was associated with nuclear data. MCF acceleration/filtering schemes applied the quantified uncertainty to the reference cases photon emissions. Logically, all MCF runs would contain an uncertainty in the photon emissions requiring a multitude of calculations. To avoid this requirement, detailed uncertainty calculations were performed on the two reference cases. These uncertainties were applied to each MCF run for acceleration/filtering results. The nuclear data uncertainty in conjunction with detector limitations places bounds on early-time conclusions.

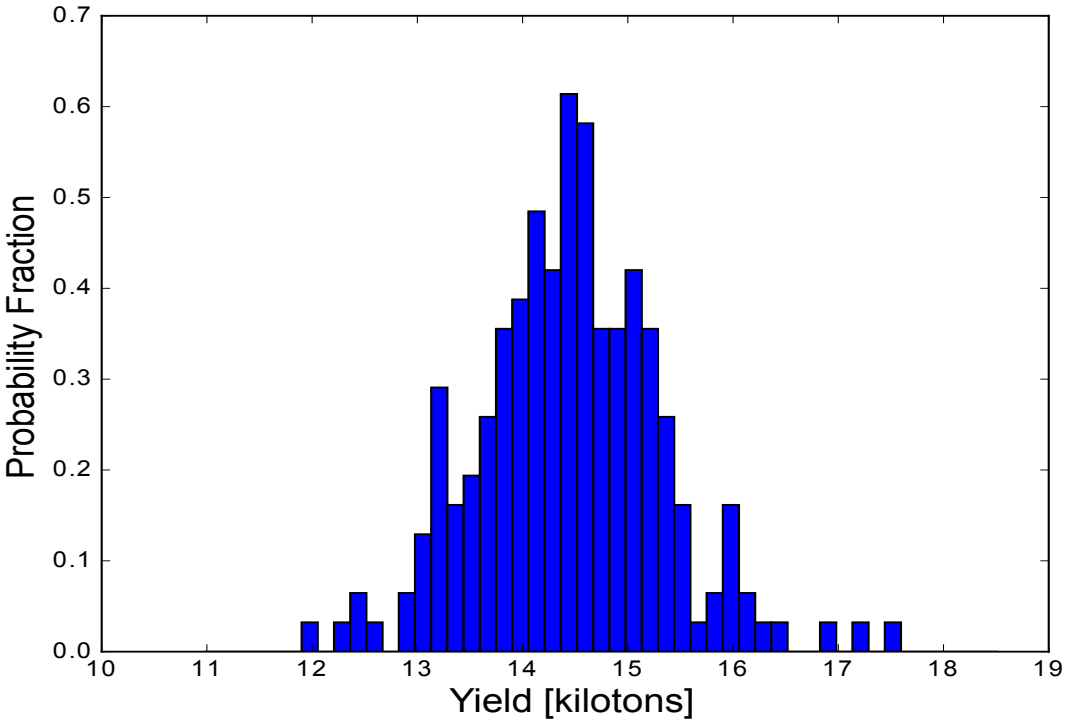


Figure 3.10: Yield distribution from cross-section uncertainties.

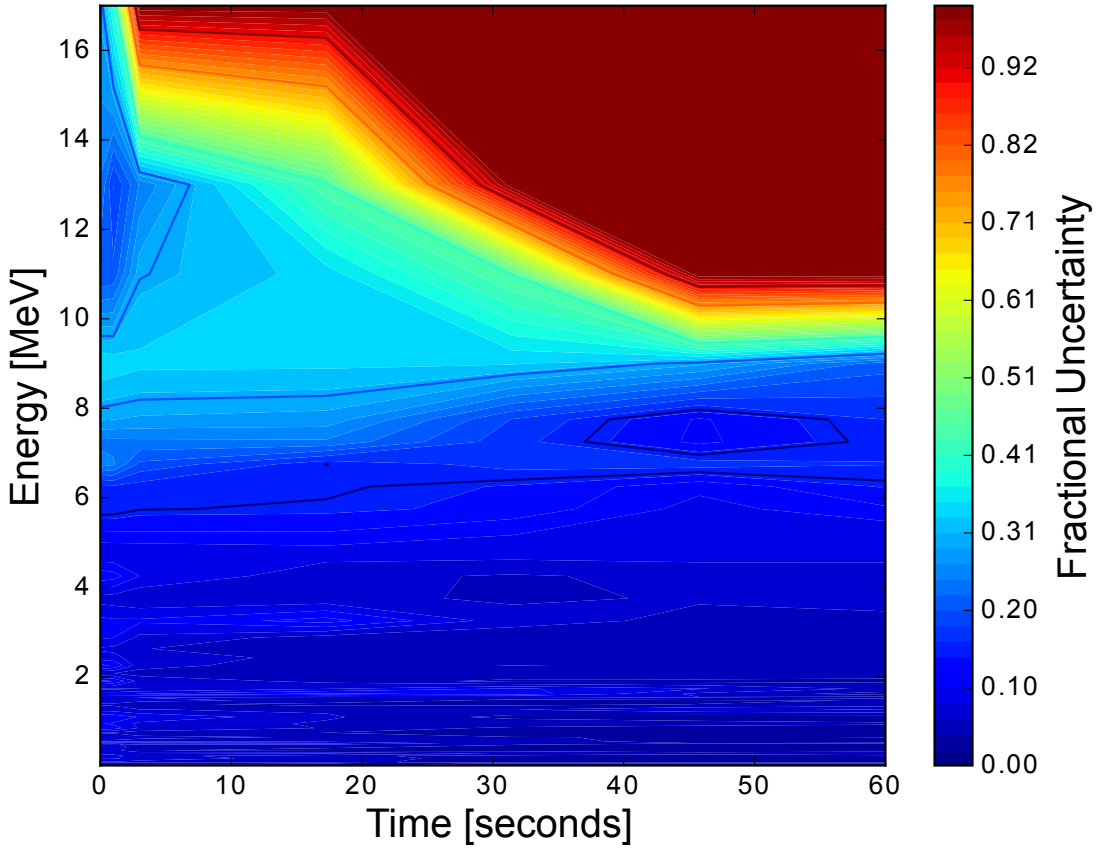


Figure 3.11: Fat Man design derivative time-dependent photon emission absolute uncertainty fraction between 0.0 and 60.0 seconds.

The uncertainty associated with the power calculation is shown in Fig. 3.10 and includes cross-sections, fission product yields, and decay uncertainty. Figure 3.11 shows the time-dependent photon emission uncertainty for the Fat Man reference spectrum including compounded uncertainty from the power curve calculation. Higher energy emissions contain large uncertainties, some equaling 100% at later times. Lower absolute uncertainties lie under approximately 6 MeV. The reference uncertainty affects conclusions based on the results from the MCF calculation and acceleration scheme. Lower overall error would reduce the amount of matched cases increasing the predictive power.

Uncertainty analysis was also used in determining an effective distance of photon detection. The generalized peri-detonation time period encompasses all phenomena and emis-

sions up to 60 seconds following detonation. The distance away from the blast are very important because of detectability which dictates information availability and quality. Uncertainty increases as the counting statistics decrease which inherently reduces conclusion confidence. Effective distance calculations were run for the Fat Man and Little Boy device derivatives from approximately 400 meters to 8050 meters (0.25-5.0 miles) with the $LaBr_3$(Ce) detector response function. The uncertainty arising from the nuclear data and integrated counts were used as a metric for determining the maximum distance allowed for passive emission detection. Effective distance should be maximized because of fireball dynamics which may impact detection equipment and the associated data.

The uncertainty ($1\sigma$) associated with the integrated counts over 60 seconds clearly show limits on detectability. Higher energy bins over 10 MeV contain over $100\%$ error at the onset of calculation or the 400 meter mark. Fortunately, none of the energy bins used for MCF acceleration and fractional mass indicators are above this energy. The error remains negligible in the lower energy bins but noticeably begins to increase around 1200 meters. Interestingly, the uncertainty spikes to over $100\%$ in every energy bin except the 0.01-0.02 MeV range at 3300 meters. The 0.01-0.02 MeV range uncertainty climbs to $90\%$ at 4600 meters. Figures 3.12 and 3.13 show the uncertainty behavior with distance for the 0.01-0.02 and 1.0-1.2 MeV energy ranges, respectively.

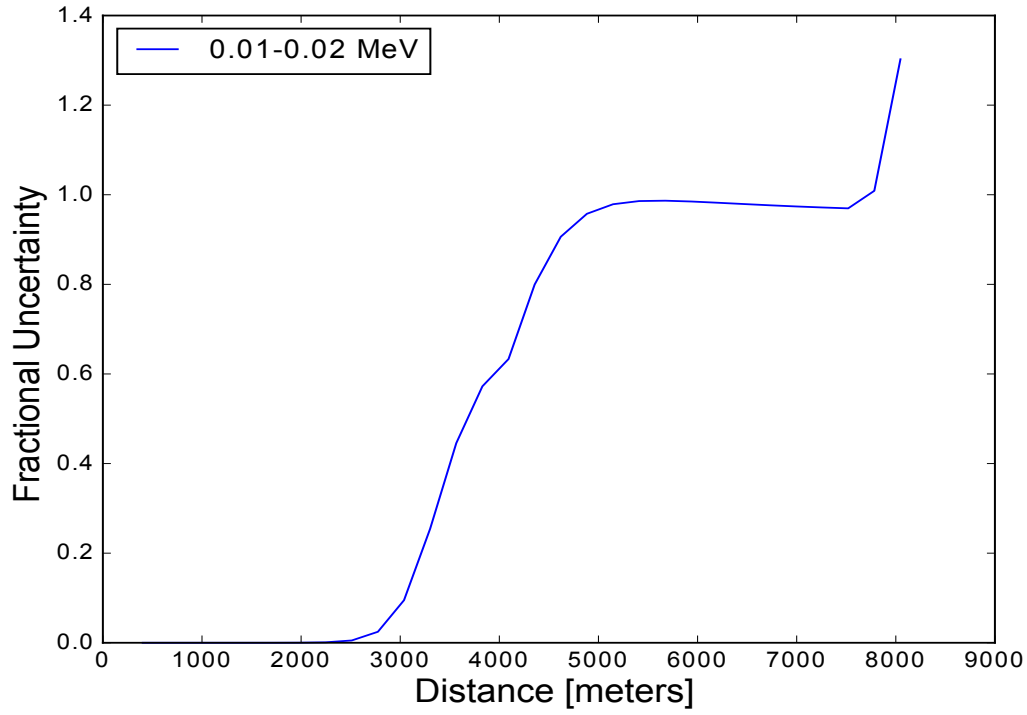


Figure 3.12: Fractional uncertainty behavior for the 0.01-0.02 MeV energy range.

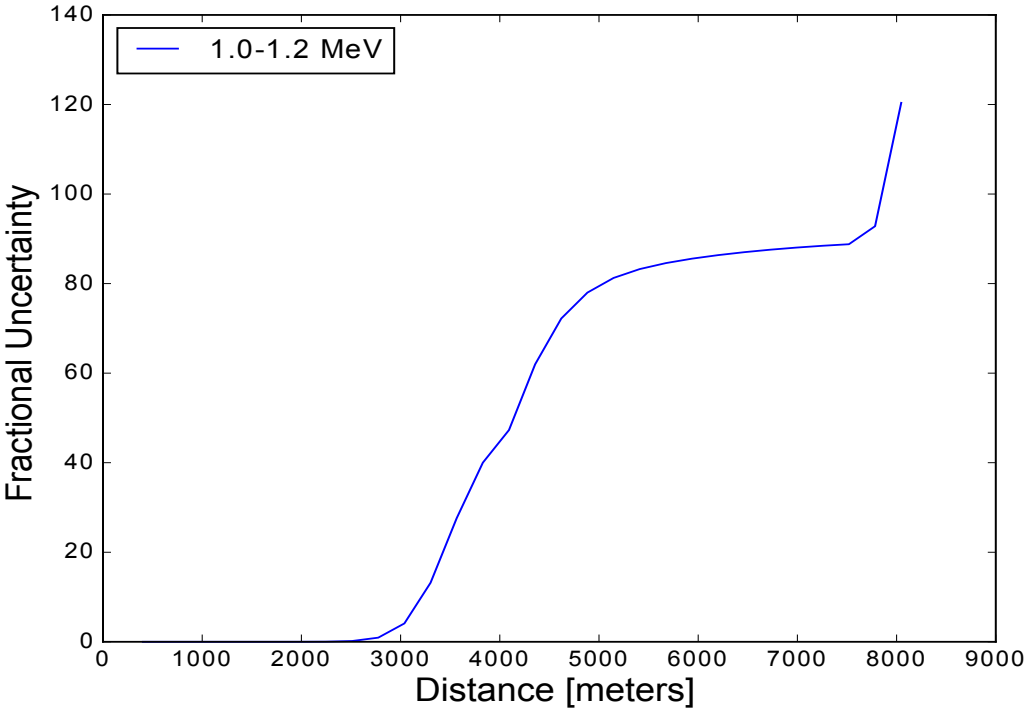


Figure 3.13: Fractional uncertainty behavior for the 1.0-1.2 MeV energy range.

The error trend associated with distance are similar between the two energy ranges. However, the error rises significantly faster with the 1.0-1.2 MeV energy range which is mainly attributed to the counting statistics as the data uncertainty ranges between 2 to 11% for the 1.0-1.2 MeV energy bin. Notably, the data uncertainty for the 0.01-0.02 MeV energy bin ranges between 3 to 8%.

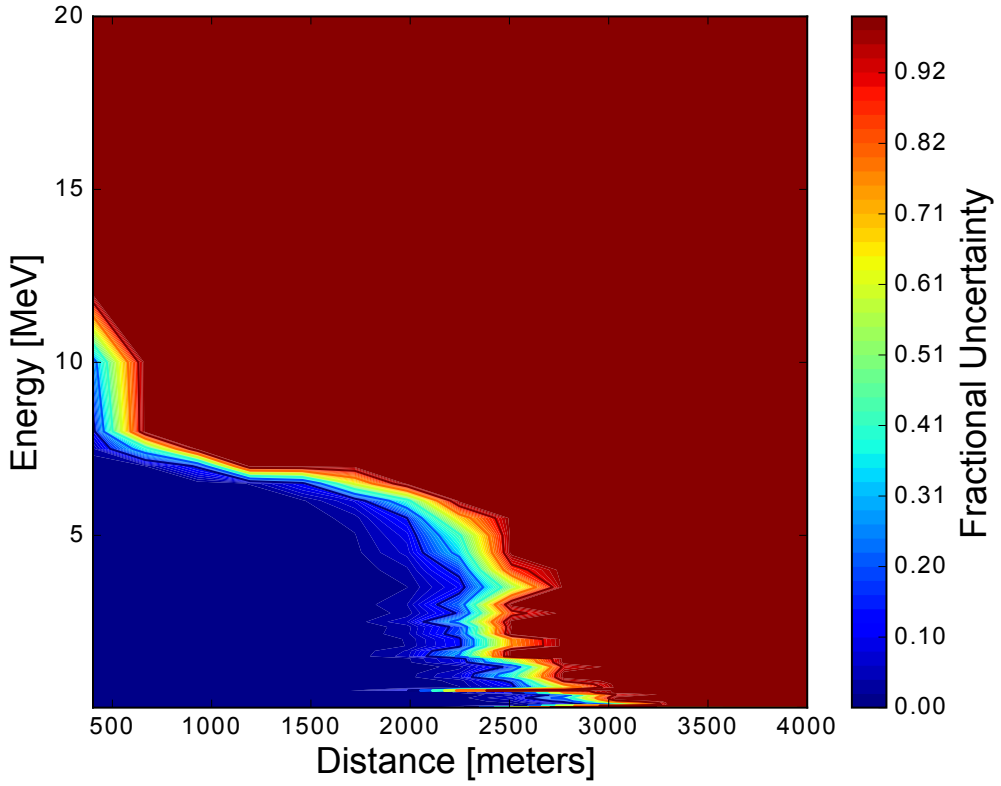


Figure 3.14: Fat Man design derivative heat map of integral detection uncertainty associated with distance from ground zero.

Figure 3.14 shows the detection uncertainty associated with distance away from ground zero for a Fat Man design derivative. The goal of passive measurement is to gain information about the device and circumstances surrounding the detonation. The distance used for the MCF algorithm was 400 meters which in reality would be destroyed shortly after detonation. In order for the detector system to convey information about the device, it must survive long enough to relay the pertinent data. Uncertainty associated with the data is important for drawing conclusions on the device. In the case of this research, nuclear

data uncertainty is compounded with uncertainty from the integral counts between 0 and 60 seconds.

The quoted uncertainties, 50%, 25%, and 5%, demonstrate the effect of distance on detectability and requiring a threshold uncertainty level which is ultimately up to the policy maker. Passive measurement uncertainty from the Fat Man design derivative reached an ultimate cut-off at 3300 meters. The energies between 1 and 6 MeV showed effective distances (with previous uncertainty levels) of 1900(50%), 1700(25%), and 1400(5%) meters while under 1.0 MeV gives distances of 1900(50%), 1900(25%), and 1700(5%) meters. For comparison, a Little Boy design derivative was modeled with the same energy output (yield) as the Fat Man derivative which produced different results.

Because the bare assembly did not contain a reflector, more of the photon emission leak out and are transported to the detector. This higher leakage is shown by energies below 1 MeV producing larger effective distances of 2200(50%), 1900(25%), and 1700(5%) meters when compared to the Fat Man derivative. The energies between 1 and 6 MeV produced effective distances of 1900(50%), 1900(25%), and 1700(5%) meters. Clearly, the shielding of photons by structural components effects the optimum distance of detection by the increase in the Little Boy derivative effective distance. The uncertainty of the Little Boy derivative is shown below in Fig. 3.15 out to 4000 meters.

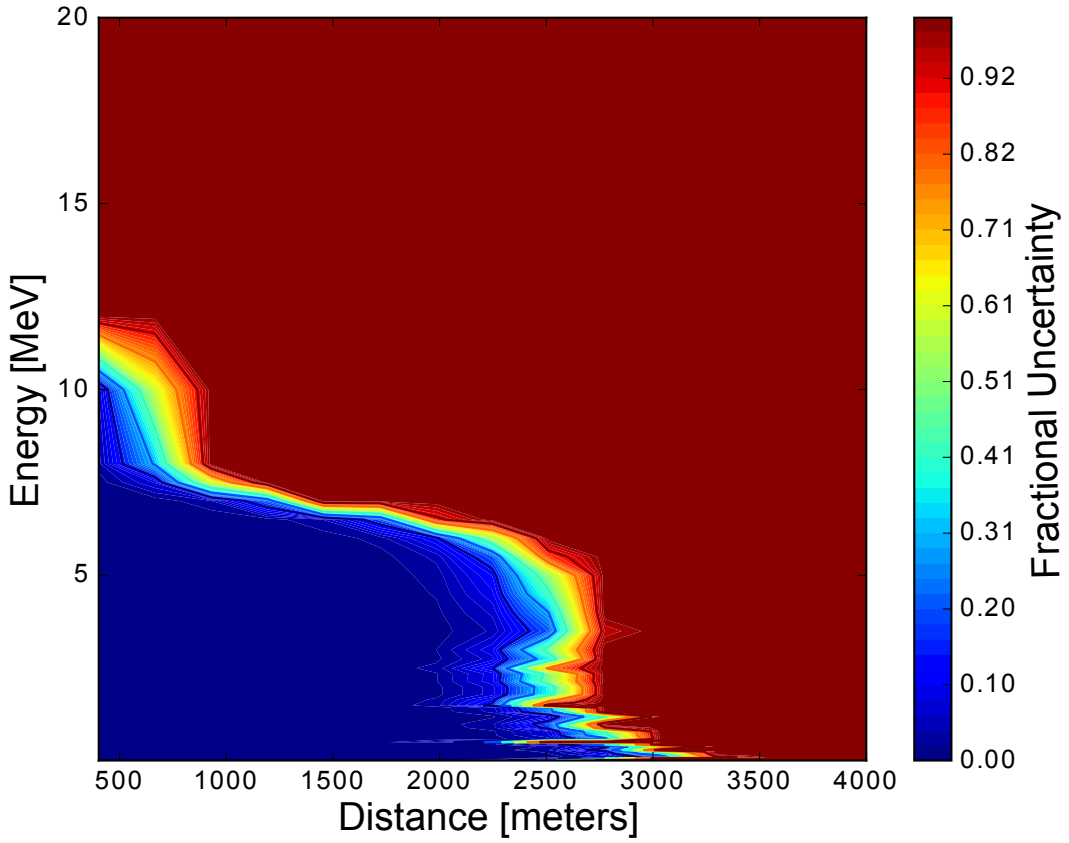


Figure 3.15: Little Boy design derivative heat map of detection uncertainty associated with distance from ground zero.

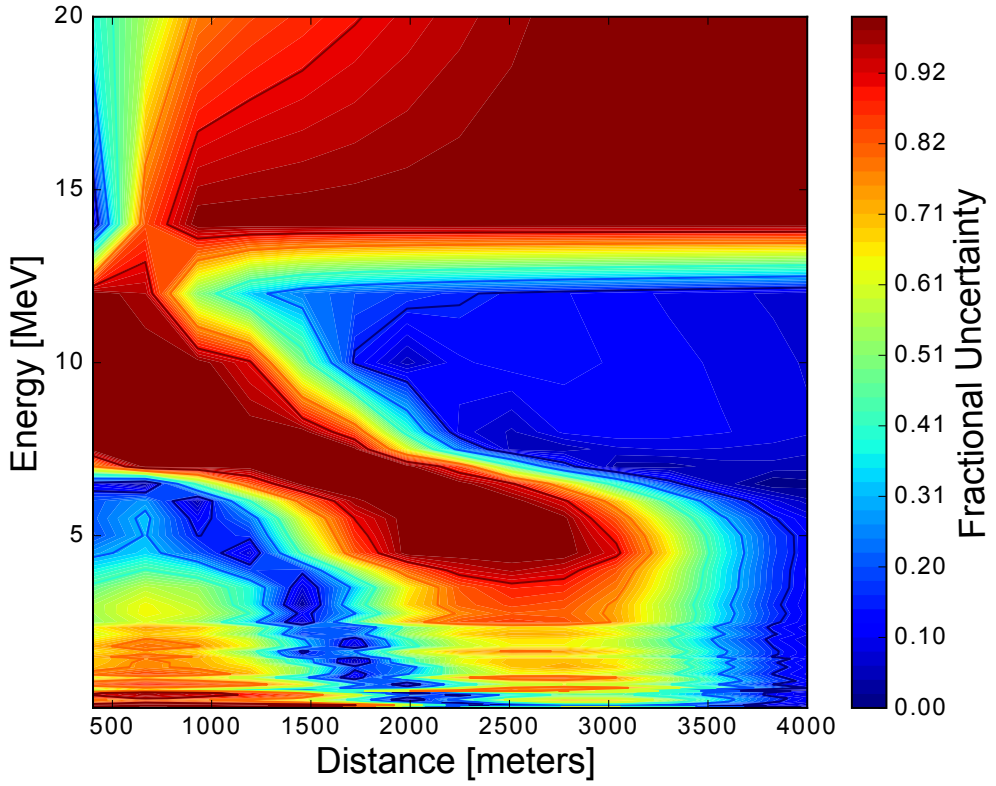


Figure 3.16: Uncertainty fractional difference between Fat Man and Little Boy design derivatives heat map associated with distance from ground zero.

The two design derivatives produce different effective distance results. These differences are shown in Fig. 3.16. The intensity scale is the fractional difference between the two device derivatives which can be attributed to the slight differences in energy output and reflection/shielding. Interestingly, there are high fractional differences between 6 and 12 MeV at short distances. Between 1500 and 3000 meters the fractional difference increases spanning from approximately 3 to 7 MeV. Starting at approximately 5 MeV, there is a band of low fractional difference that resembles a sigmoidal function extending out between 2000 and 2500 meters. Because the design is unknown during an event, effective distances must be conservative. This conservative requirement demands using the Fat Man design derivative lesser effective distances.

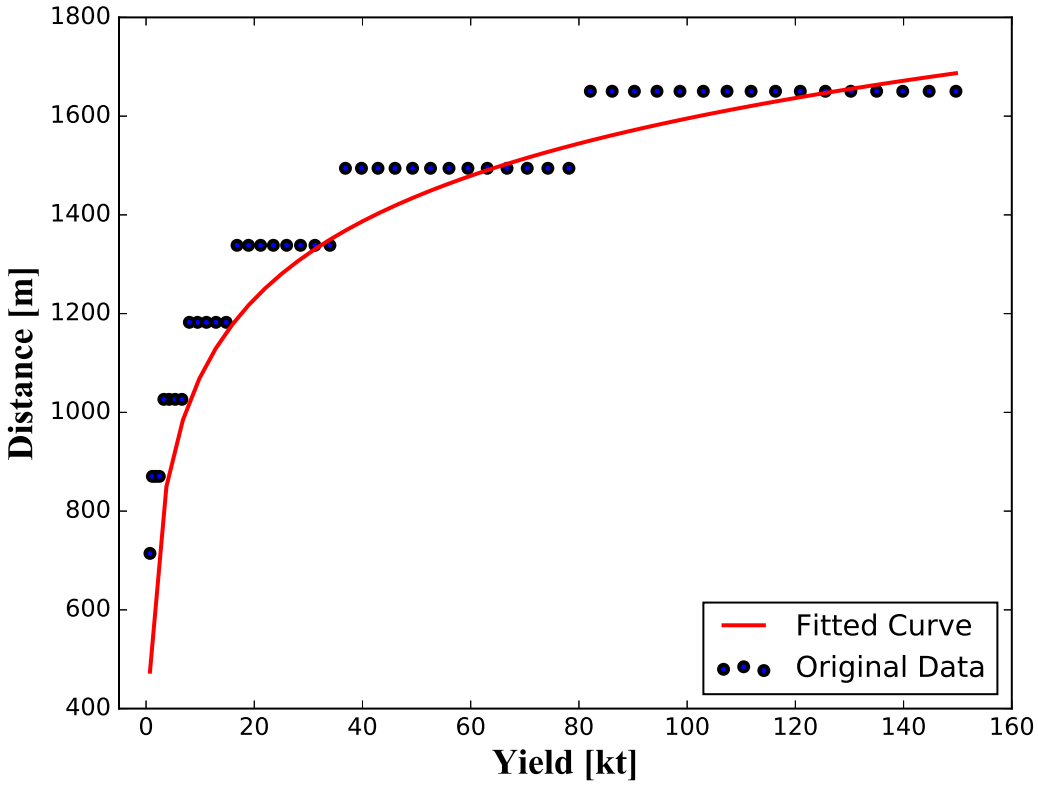


Figure 3.17: Fat Man design derivative yield and distance relationship with error set at 10%.

Figure 3.17 shows the device yield relationship to effective distance of detectability. The effective distance was determined by setting the aggregate error from the counts and cross-sections to 10%. To provide a conservative estimate of effective distance, the max yield for each distance estimate (horizontal lines) was fitted with a logarithm function shown below in Equation 3.27.

$$D = 227.30 \ln(3.34W) \tag{3.27}$$

where:

$D$ is the effective distance of detectability for 10% error,

$W$ is the device yield in kt.

The conservative fit will lower the effective distances for lower yields which is a safe assumption considering the grouping of the distances. Grouping or setting the data to $10\%$ caused the horizontal distances to be discretized into the trend shown in Fig. 3.17. The developed effective distance formula aids placement of a scintillation detection system at a prescribed device yield.

### 3.4.2 Point-Source Model Sensitivity Analysis Results

Variance decomposition methods, developed by Sobol, highlighted input variable behavior within the complex system well. Relationships shown in this section were used to accelerate MCF in the spatial model. To understand the behavior of the input variables on energy and time-dependent photon spectra, first-order and total sensitivity indices were examined with raw rates ($\frac{photons}{second}$) in the photon energy bin over 60 seconds.

#### *Unfractionated Sample Sensitivity Analysis Results*

An unfractionated sample represents all photons generated from ORIGEN depletion calculation. This portion of the SA is used for MCF acceleration and does not include fission or activation photons. Consequently, the relevant times in this SA are following the Gaussian burnup (1.0E-06 seconds) and before the initialization time of nuclear cloud rise (approximately 3.0 seconds). Because of these constraints, the time period examined is between 1.0E-05 and 1.0E-01 seconds.

For brevity, all first-order and total sensitivity indices raw values for the variables: neutron spectrum (shape), flux (magnitude), and fuel-type ($^{238}$U, $^{235}$U, $^{233}$U, $^{239}$Pu) are not shown. The number of variables, energy groups (47), and time steps prohibit displaying within reason. Instead, the main effect and total sensitivity indices are averaged, including $2\sigma$ bounds, over each photon energy bin.

Figure 3.18 shows the mean $S_i$ indices for the flux, spectrum, $^{238}$U, and $^{235}$U for the unfractionated sample with no applied detector response. Overwhelmingly, the flux has

the highest importance towards each photon energy bin. The small $2\sigma$ standard deviation indicates little fluctuation in the $S_i$ main effect index across photon energy bins. Spectrum shape is the next highest importance but is roughly 2 orders of magnitude less than the flux $S_i$ value. Other aforementioned variables $S_i$ values are extremely small hence not contributing to the output variance and therefore not displayed.

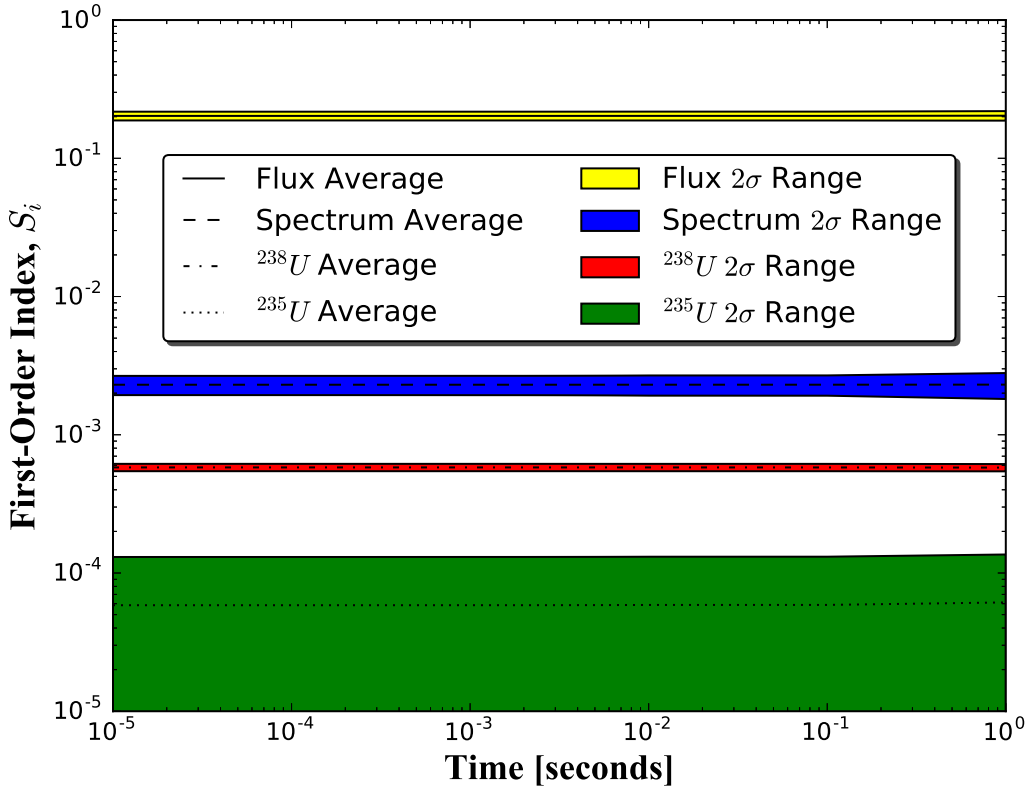


Figure 3.18: Unfractionated $S_i$ values averaged over photon energy bins for flux, spectrum, $^{238}$U, and $^{235}$U with flux variable being the highest contributor to photon production.

For clarity, the mean value of the flux $S_i$ value is approximately 0.2 across time. This value indicates knowing the true flux value would only explain roughly 20% of the variance in each of the photon energy bin emissions. The low value of correlation is attributed to nonlinearities or interactions between the other input variables. Further insight is gained through examining the total sensitivity indices, $S_T$.

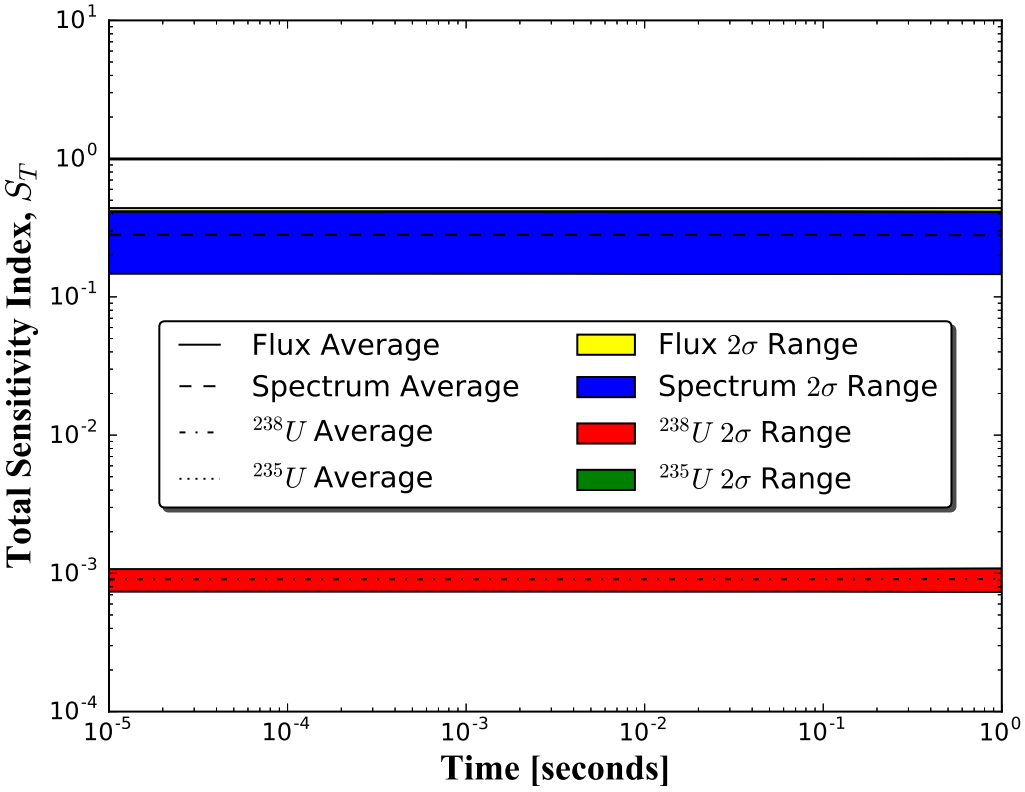


Figure 3.19: Unfractionated $S_T$ values averaged over photon energy bins for flux, spectrum, $^{238}$U, and $^{235}$U with $^{235}$U having the highest value.

Figure 3.19 shows the mean total sensitivity indices, $S_T$, for the same input variables. Interestingly, $^{235}$U increases approximately 5 orders of magnitude from its $S_i$ value. This dramatic increase is attributed to heavy interactions between the other input variables or strong nonlinear relationships to photon emission. Noteworthy, $^{233}$U and $^{239}$Pu $S_T$ values increased to approximately 1.0. Flux and spectrum values increased approximately 2 and 1000 times, respectively. Again, these increases are attributed to interactions between the input variables and nonlinearities. These indices provide clues to the underlying data structure and relationships.

There are 47 photon energy groups and many time steps for which relationships can be derived. For concision, energy bins and times are arbitrarily chosen for method demonstration. From the previous flux $S_i$ and $S_T$ values some amount of linear correlation exists

between the flux and photon rates. The difference between the $S_i$ and $S_T$ values indicate there are possible interactions and nonlinearities associated. For example, Figure 3.20 illustrates the nonlinearity relationship to the photon rate in the 1.0-1.2 MeV photon bin at 1.0 second following detonation.

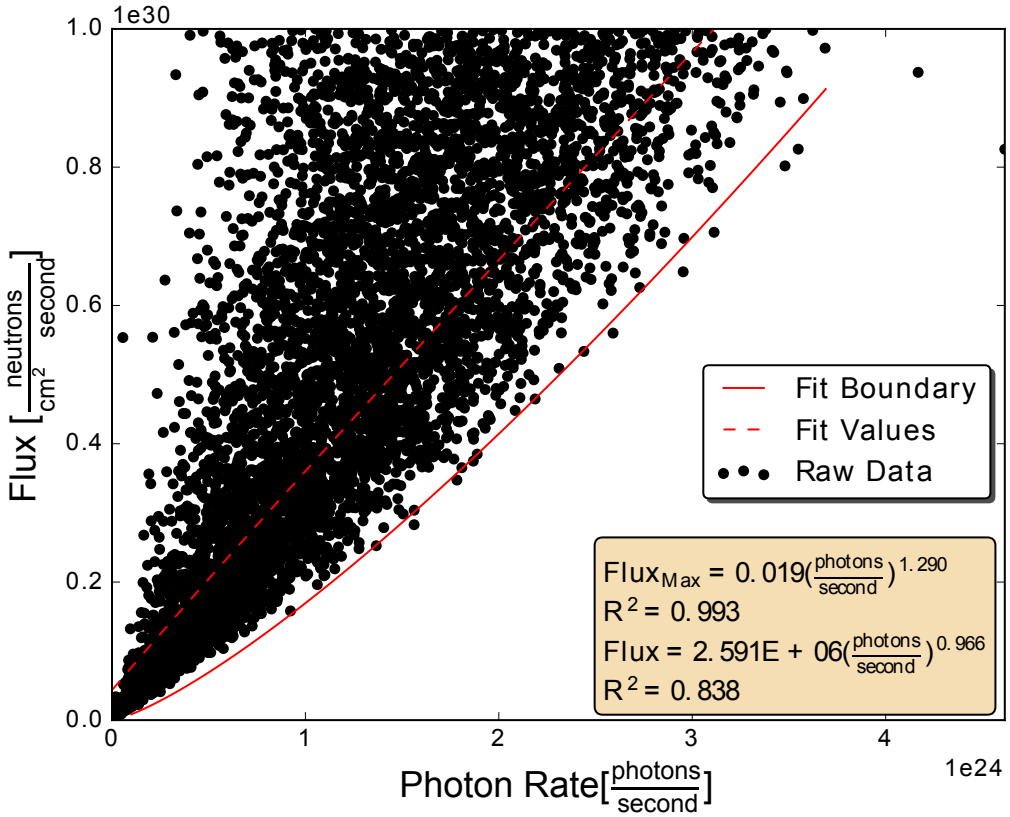


Figure 3.20: Unfractionated flux association with 1.0-1.2 MeV photon energy bin rate at 1.0 second.

Because the $S_i$ values for the flux are the highest - relative - for all variables, correlation to the photon rates is more likely. A power law relationship to the photon rate in the 1.0-1.2 MeV was found between the flux. This flux relationship presents more error to the prediction value obtained from the formula because of the $R^2$ value. The higher error can also be seen in the low $S_i$ values for the flux. Nevertheless, predictions using the formulas in Fig. 3.20 still lower the distribution of flux values given to the MCF method. Because the $S_i$ values for the spectrum, $\bar{E}_{neutron}$, are quite low, the relationship to the photon rate is nonexistent as shown in Fig. 3.21. Notably, these relationships were developed from ran-

dom unstratified Monte Carlo sampling and do not incorporate detector response functions. This type of sampling produces nonphysical configurations and outputs.

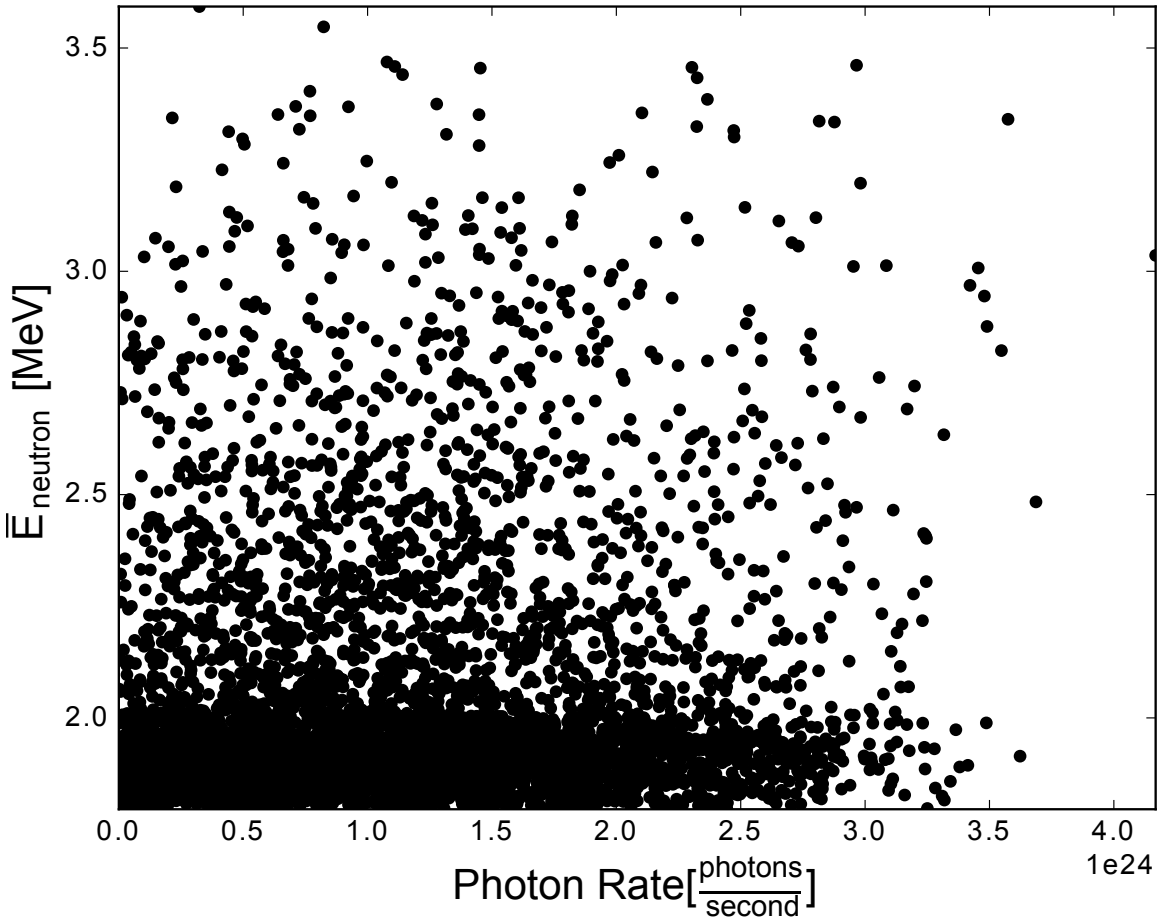


Figure 3.21: Unfractionated spectrum association with 1.0-1.2 MeV photon energy bin rate at 1.0 second.

For the purposes of MCF acceleration, the total energy output (yield) and a rough indication of fuel-type is important. Figure 3.22 shows yield scales almost linearly to the photon rate in the 1.0-1.2 MeV photon bin. Because activation and attenuation information are not present, mass information is difficult to deduce shown in Fig. 3.23.

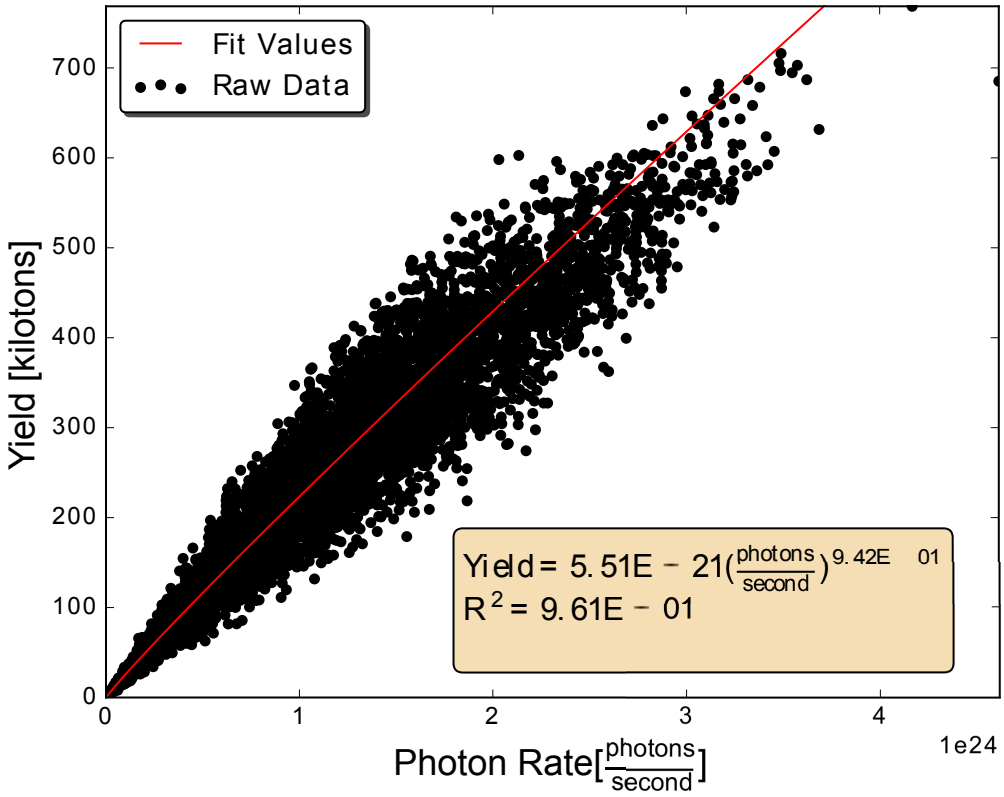


Figure 3.22: Unfractionated yield association with 1.0-1.2 MeV photon energy bin rate at 1.0 second.

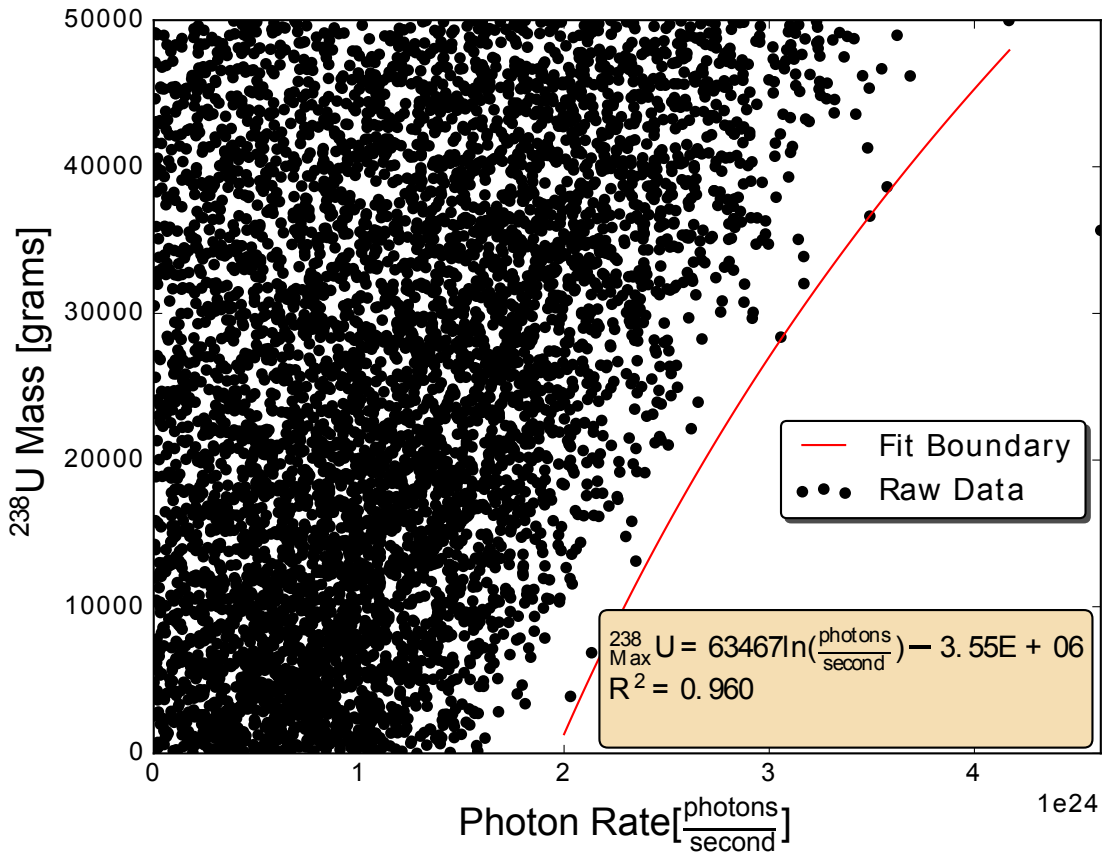


Figure 3.23: Unfractionated $^{238}$U mass association with 1.0-1.2 MeV photon energy bin rate at 1.0 second.

Although the $^{238}$U mass estimates appear scattered, there is a clear outer photon rate and mass boundary. This outer boundary can further be fit to reveal the upper amount of $^{238}$U mass. Because these relationships do not consider detector response, the relationships cannot be used for the MCF acceleration scheme. Also, the Monte Carlo sampling used for these relationships was unstratified meaning that some nonphysical samples were generated. This unstratified sampling also prohibited the use of relationships in this section for MCF acceleration. Relationships developed and used are shown in Sec. 3.4.3.

*Fractionated Samples Sensitivity Analysis Results*

Chemical fractionation occurs at approximately the carrier material solidification temperature. Because the sample is not fractionated before this point, the time period examined

is between 3.0-60.0 seconds. Fractionation levels of 0.1 and 0.5 were examined to show refractory and volatile behavior. Because of the brief time period each sample, 0.1 and 0.5, will have a presence in the nuclear cloud. Similarly, all first-order and total sensitivity indices raw values for the variables: neutron spectrum (shape), flux (magnitude), and fuel-type ($^{238}$U, $^{235}$U, $^{233}$U, $^{239}$Pu) are not shown.

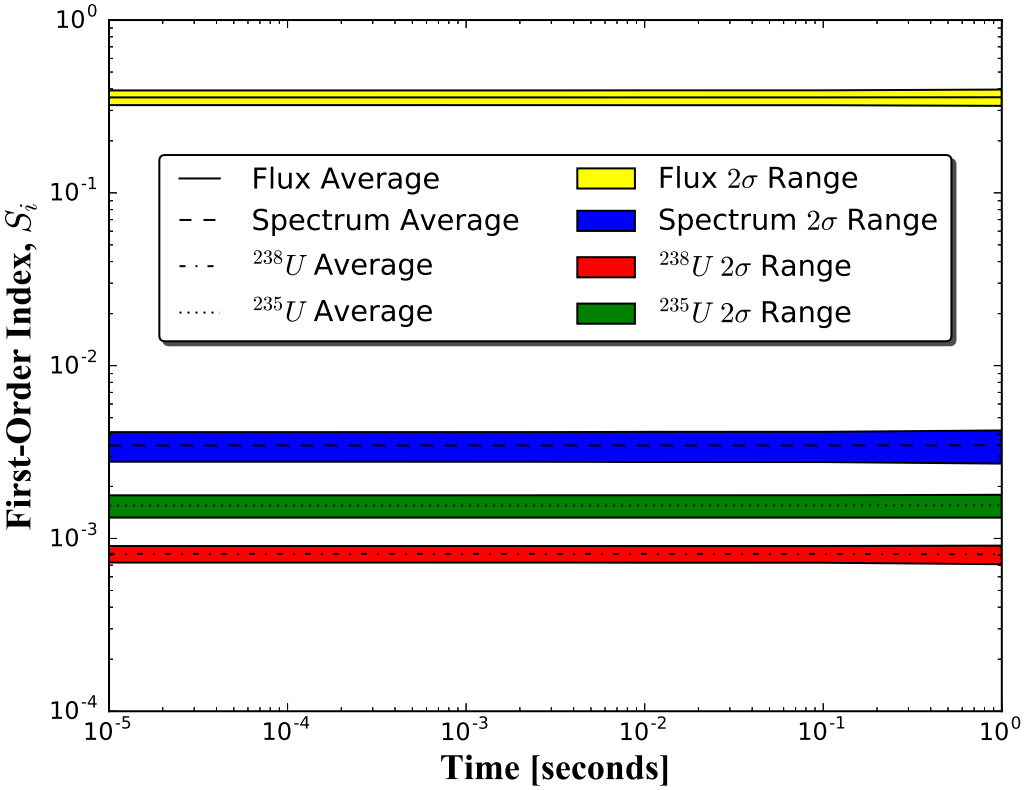


Figure 3.24: Fractionated - 0.1 - $S_i$ values averaged over photon energy bins for flux, spectrum, $^{238}$U, and $^{235}$U with flux variable being the highest contributor to photon production.

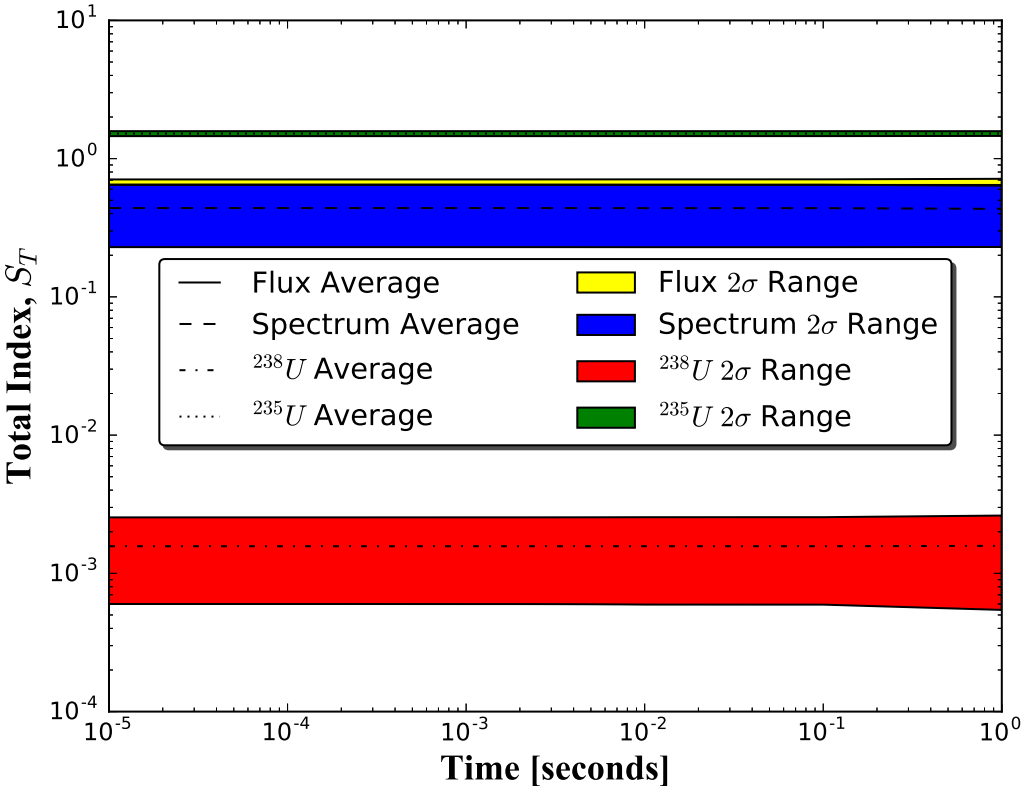


Figure 3.25: Fractionated - 0.1 - $S_T$ values averaged over photon energy bins for flux, spectrum, $^{238}$U, and $^{235}$U with $^{235}$U variable with the highest $S_T$ index value.

Figs. 3.24 and 3.25 represent the average $S_i$ and $S_T$ over energy with upper and lower bounds. $^{235}$U sensitivity indices change drastically between main and total effects. This change is indicative of heavy interaction ($S_T$ value over 1) between the input variables and nonlinearities in the relationship. Interestingly, $^{238}$U's sensitivity indices remain negligible, meaning removing $^{238}$U from the model would not affect the energy photon emission rate. The flux and spectrum indices move upwards but remain under 1 indicating nonlinearities and interactions. Previous flux plots, Fig. 3.20, have confirmed nonlinearities by the found power law relationships. The spectrum relationship is mostly attributed to interactions with other variables because of the similar $S_i$ and $S_T$ values and previous plots (Fig. 3.21). The flux yields the highest importance for both the 0.1 and unfractionated samples.

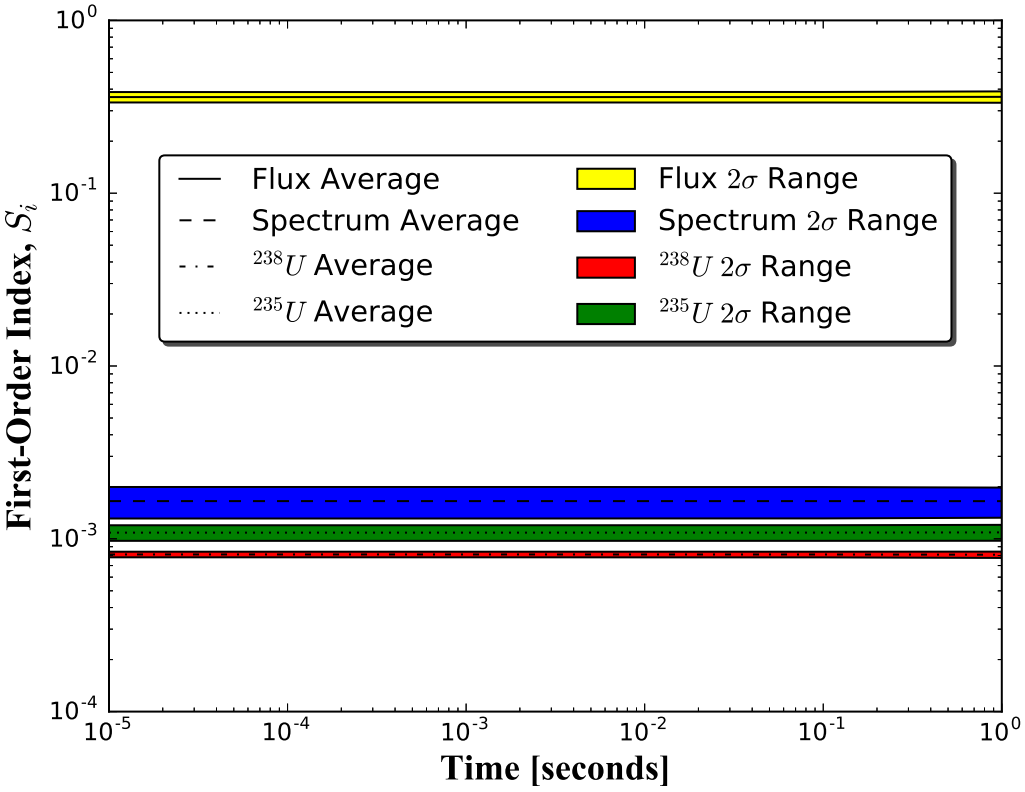


Figure 3.26: Fractionated - 0.5 - $S_i$ values averaged over photon energy bins for flux, spectrum, $^{238}$U, and $^{235}$U with flux variable being the highest contributor to photon production.

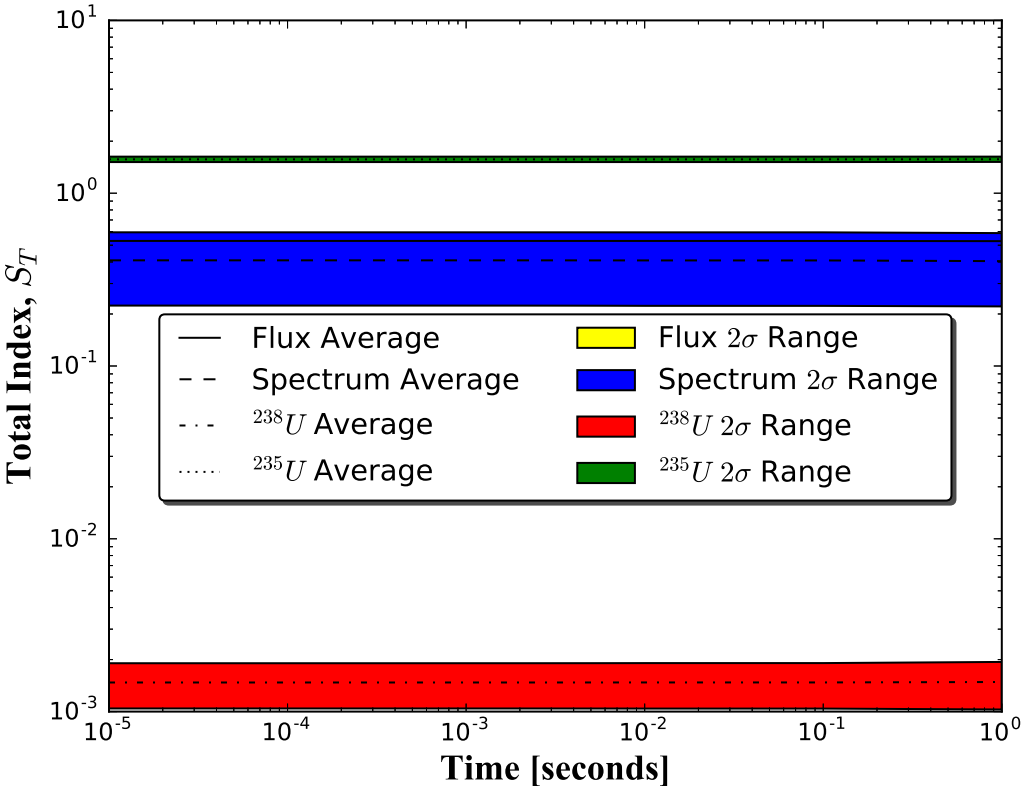


Figure 3.27: Fractionated - 0.5 - $S_T$ values averaged over photon energy bins for flux, spectrum, $^{238}$U, and $^{235}$U with $^{235}$U variable with the highest $S_T$ index value.

Similarly, Figs. 3.26 and 3.27 show the same behavior over the given time period. The flux maintains the highest main effect to the rate within the energy bin while $^{238}$U maintains the lowest. Interestingly, the spectrum variable $S_T$ bounds hide the flux variable. Because of these higher $S_T$ values shown in Figs. 3.27 and 3.25, model reduction by setting these values to zero is not possible. This trend is also present with the $^{233}$U and $^{239}$Pu variables, which are absent from the Figures for their overlap of $^{235}$U values. Alternatively, $^{238}$U can be set to zero without affecting the energy bin photon emission rate. Seemingly, the behavior across each sample (unfractionated, 0.1, and 0.5) is similar.

### 3.4.3 Spatial Model Monte Carlo Filtering Results

Reference cases were generated to mimic Little Boy and Fat Man devices from known open source mass estimates with randomly selected densities. MCF techniques typically require sampling of the entirety of the known input space. In this case, the sample space encompasses many configurations with varying fuel types, reflectors, and densities. To narrow down the MCF input space, point-source model SA results/relationships are used to accelerate the search substantially reducing computation time.

*Unaccelerated Monte Carlo Filtering Results*

For demonstration, the MCF algorithm was run, without any acceleration scheme or uncertainty, against the Fat Man design derivative reference spectrum using 5000 randomly generated samples. Only the first check results are shown which were checked against the reference spectrum shape. Pass fractions above 0.40 were accepted as possible configurations.

Out of the 5000 random simulations, 80 matched the spectrum shape with the above constraints or 1.6%. Each of the possible fuel types, $^{235}$U, $^{233}$U, $^{239}$Pu, were matched with varying masses and reflectors. The 80 matched samples contained a multitude of yields shown in Fig. 3.28.

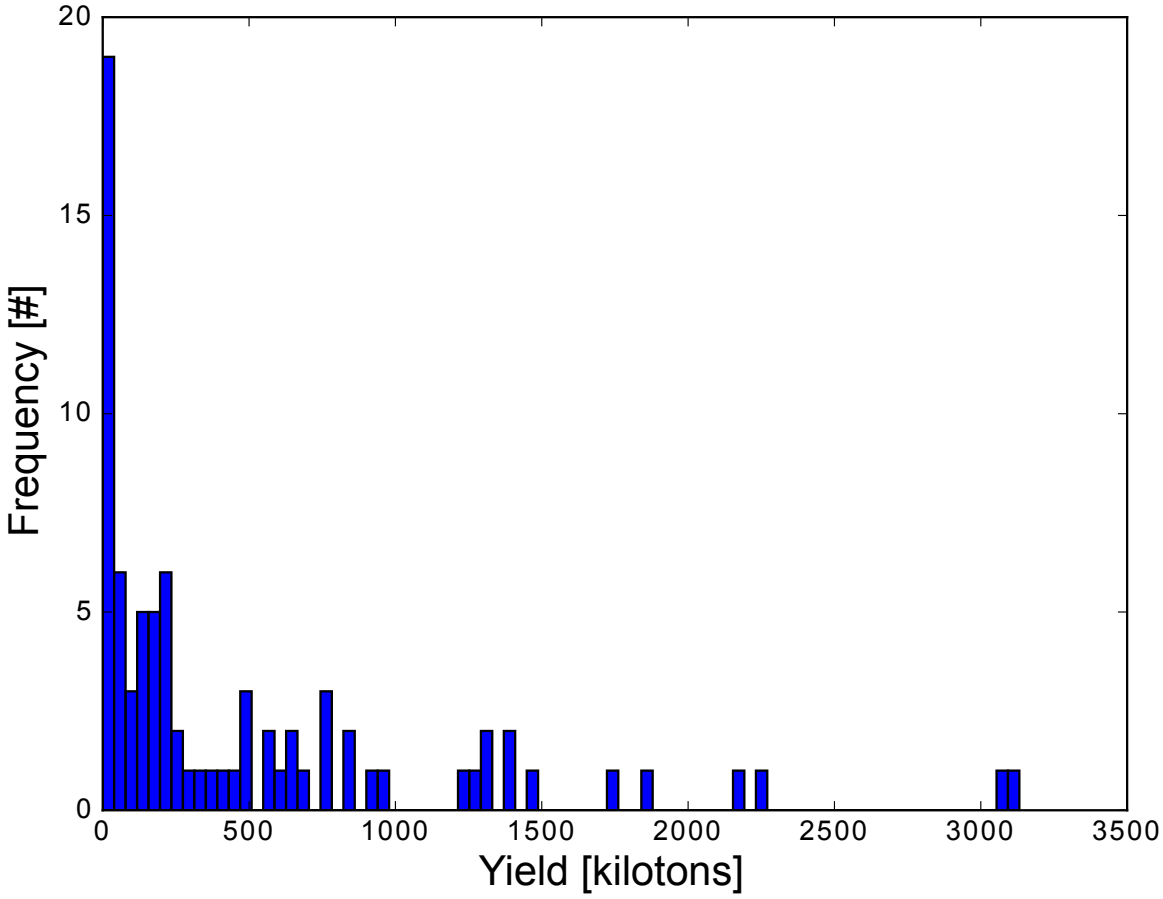


Figure 3.28: Yield distribution of unaccelerated Monte Carlo Filtering results from 80 matched samples.

The yield distribution contained a range of yields from 1.0E-03 to 3.1E+03 kilotons. Interestingly, most of the yields occur under 1.0E+03 kilotons. Although the yield distribution can narrow the scope and contribute to early-time information, the goal of matching spectrum shape is to provide clues regarding fuel, structural components, density, and mass. Examining macro level behavior can also become important. For example, the fissile or primary fuel mass distribution is shown in Fig. 3.29 while the reflector mass is shown in Fig 3.30.

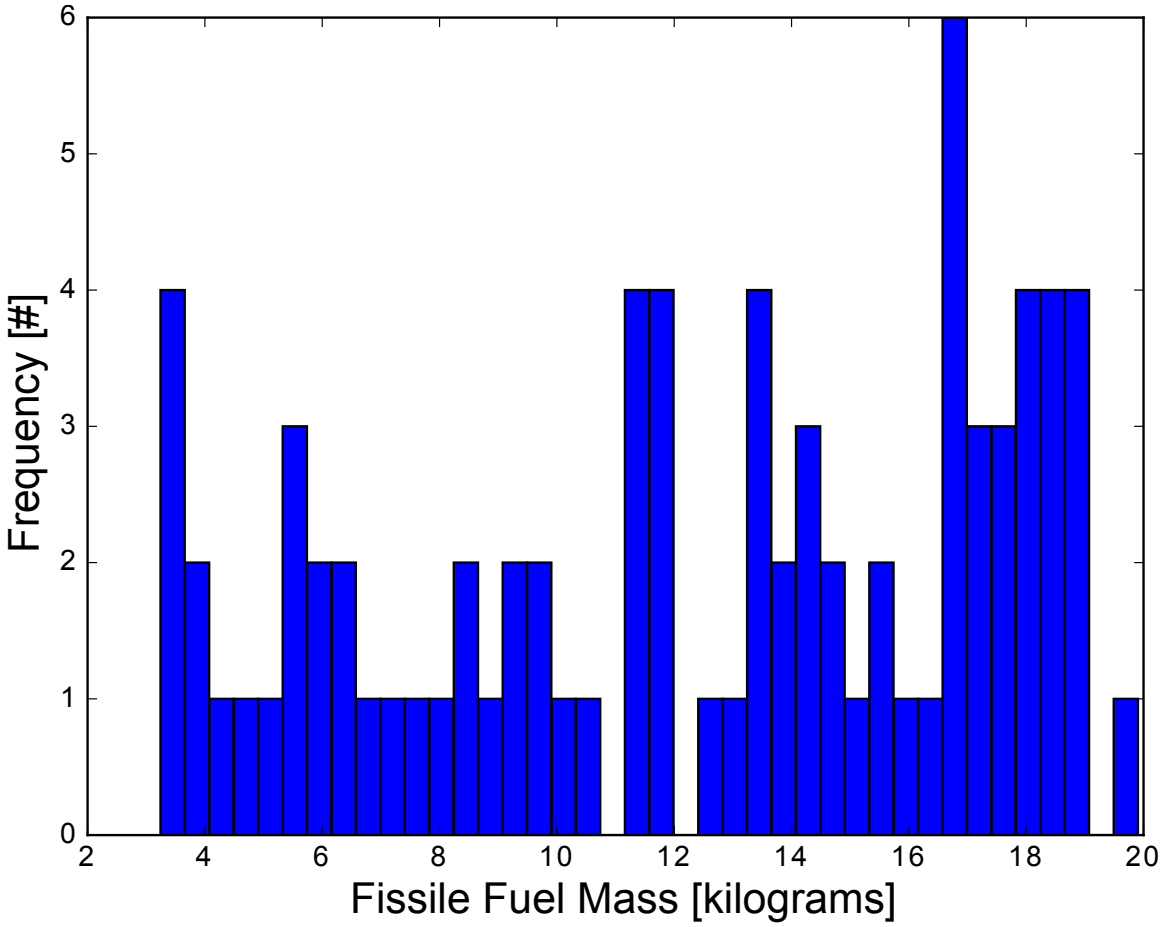


Figure 3.29: Fissile fuel mass distribution of unaccelerated Monte Carlo Filtering results from 80 matched samples.

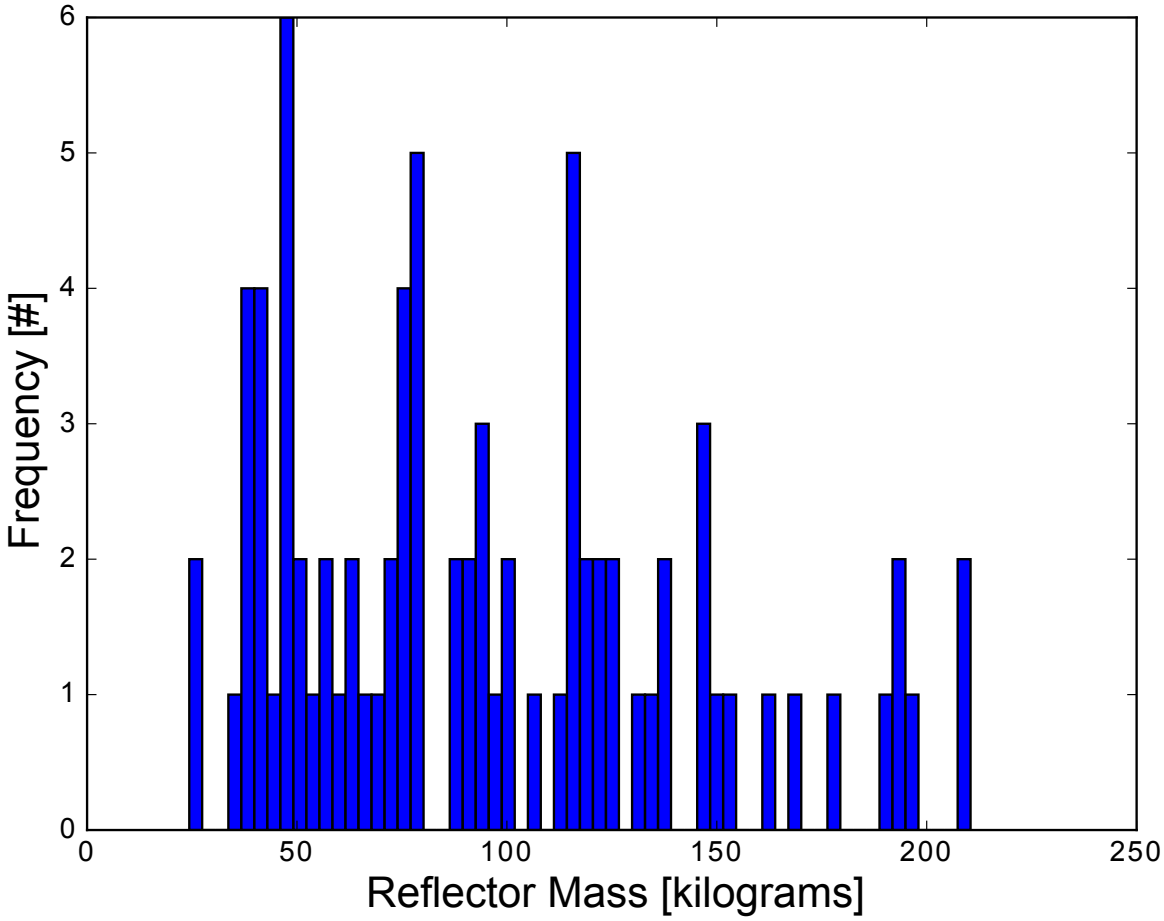


Figure 3.30: Reflector mass distribution of unaccelerated Monte Carlo Filtering results from 80 matched samples.

Matched fissile and reflector masses were widely distributed in the above plots. The fissile mass ranged from 3.2E+00 to 2.0E+01 kilograms while the reflector mass ranged from 2.4E+01 to 2.1E+02 kilograms. In fact, the weighted average of the fissile mass distribution equates to 1.2E+01 kilograms. The weighted average of the reflector mass was calculated to be 9.5E+01 kilograms. The "true" values are 6.2E+00 and 1.0E+02 kilograms for the fissile and reflector masses, respectively. These calculated masses equate to 100% and 5% differences for the fissile and reflector masses. Although the distributions seem uninformative, probability distributions can easily be derived and further refined through other MCF runs.

Interestingly, approximately 73% of the matched cases were $^{239}$Pu fissile fuel and 52%

matched as $^{238}$U reflector. The mass results were less reliable for the fissile fuel yet the type of fuel matched 73% of the time. Conversely, the reflector weighted mass was within 5% of the "true" value while the type was only matched 52% of the time. Noteworthy, a Tungsten reflector matched 46% of the samples.

The whole input space was sampled without an acceleration scheme or nuclear data uncertainty. Without the acceleration scheme, reflector mass was matched to within 5% and fissile fuel type was matched 73% of the time. Applying the acceleration scheme shrinks the possible input distributions placing the samples generated in closer proximity to the "true" configuration.

*Monte Carlo Filtering Acceleration Results*

Previous relationships derived in Section 3.4.2 cannot be used for acceleration because of the absence of the detector response function and unstratified sampling which generates nonphysical configurations. The results presented in this section have applied detector response functions using stratified sampling. Because of the short time line, results are obtained from an unfractionated sample encompassing the aggregate fission product photon emission. The time period examined for the acceleration was between 1.00E-05 and 1.00E-01 seconds or the onset of the back-end time period discussed previously. This time period was chosen to highlight fission product photon emission relationships minimizing nuclear cloud rise effects/distortions. SA indices, $S_i$ and $S_T$, were not determined for each possible ratio; therefore, sensitivities were determined by regression analysis and maximizing the each energy groups "purity" metric. These sensitivities provided the metrics for relationship development by maximizing the correlation coefficient between fractional mass and energy ratios and "purity" values.

Applying a detector response function to the photon emission data drastically changes the relationships shown in Sec. 3.4.2. This change is attributed to the limitations of the detector affecting the amount of data available for inference. Regardless, any informa-

tion obtained is beneficial to accelerate the MCF algorithm. The relationships shown in Figs. 3.31-3.34 were developed using the integral count sensitivities between 1.00E-05 and 1.00E-01 seconds including the detector response function which allowed calculation of a purity metric. Regression analysis was also used in determining the relationships by maximizing the correlation coefficients of each possible ratio. Energy group boundaries can be found in Table 3.4. Figures 3.31-3.34 show the fissile/fissionable fuel fractional mass predictive relationships. The formulas resulting from the fits were used for the MCF acceleration. All the associated purity metrics show highly interactive denominator values while numerator values indicated lower interactions. The energy range purity values used in the MCF acceleration fits found in Figs. 3.31-3.34 are shown below in Tables 3.5-3.8.

Table 3.5: $^{233}$U sensitivity "purity" calculated from $S_i$ and $S_T$ values.

| Energy Range [MeV] | Purity |
|---|---|
| 9.000E-01 - 8.000E-01 | 0.0102 |
| 7.000E-01 - 6.000E-01 | 0.001386 |

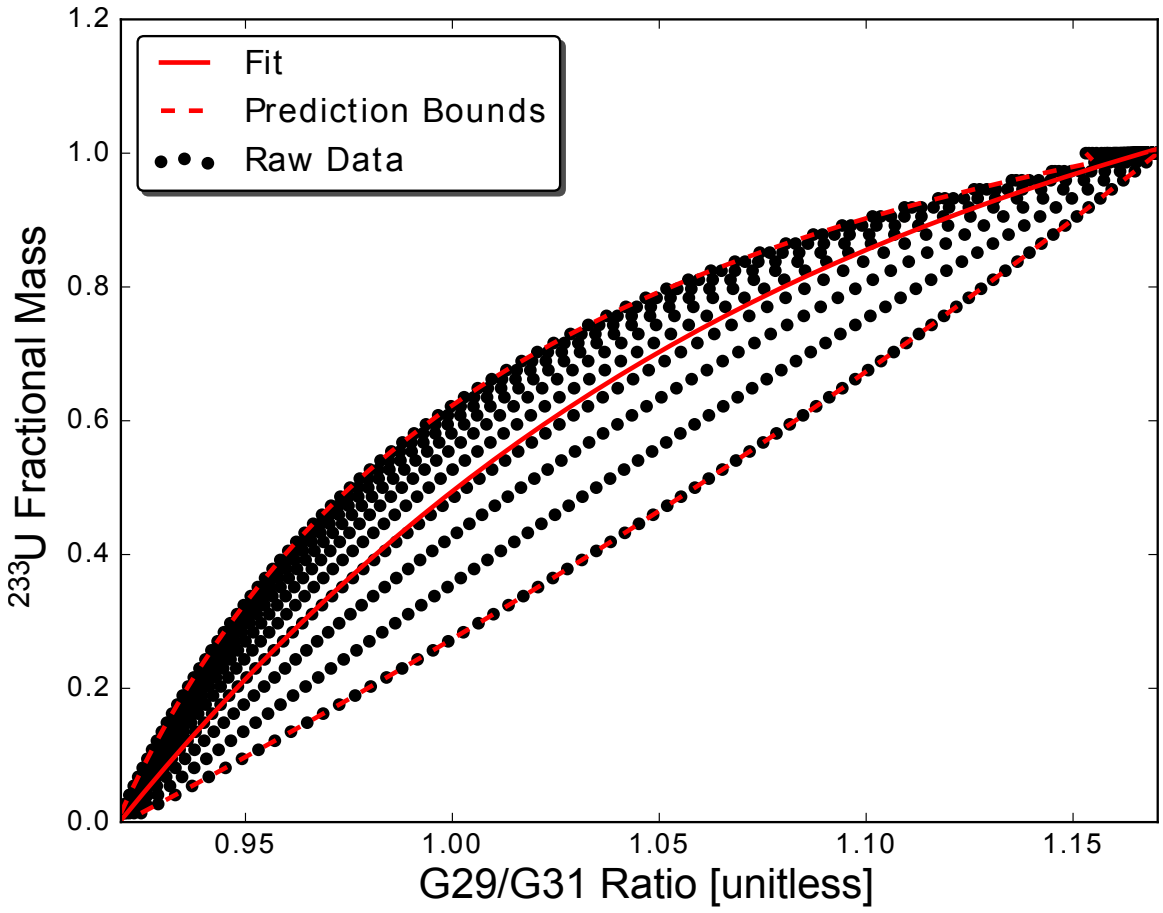


Figure 3.31: $^{233}$U fractional mass from the $\frac{G29--0.80-0.90MeV}{G31--0.60-0.70MeV}$ ratio with associated prediction bounds.

Table 3.6: $^{235}$U sensitivity "purity" calculated from $S_i$ and $S_T$ values.

| Energy Range [MeV] | Purity |
|---|---|
| 2.000E+00 - 1.800E+00 | 0.002081063 |
| 1.800E+00 - 1.660E+00 | 0.0003886 |

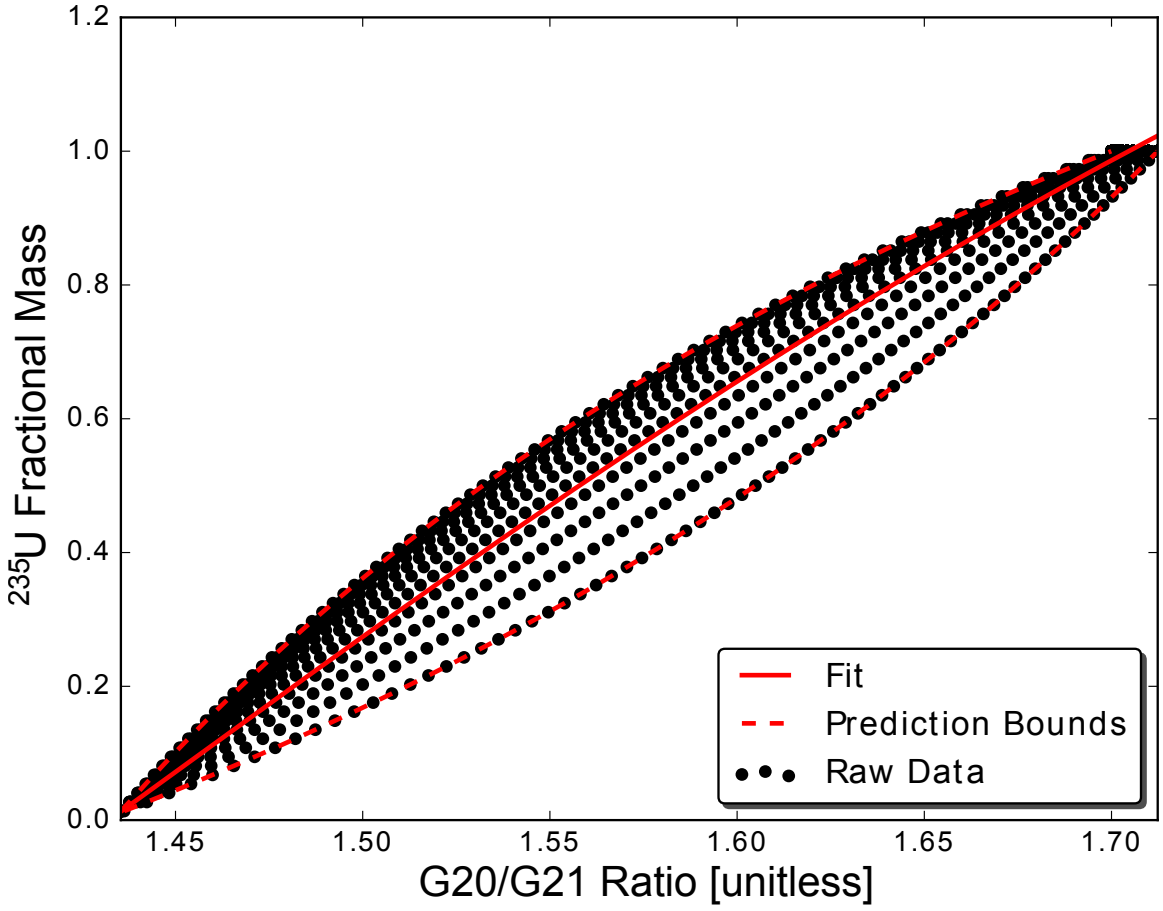


Figure 3.32: $^{235}$U fractional mass from the $\frac{G20--1.80-2.0MeV}{G21--1.66-1.80MeV}$ ratio with associated prediction bounds.

Table 3.7: $^{238}$U sensitivity "purity" calculated from $S_i$ and $S_T$ values.

| Energy Range [MeV] | Purity |
|---|---|
| 2.500E+00 - 2.350E+00 | 28.7353 |
| 2.150E+00 - 2.000E+00 | 0.7875 |

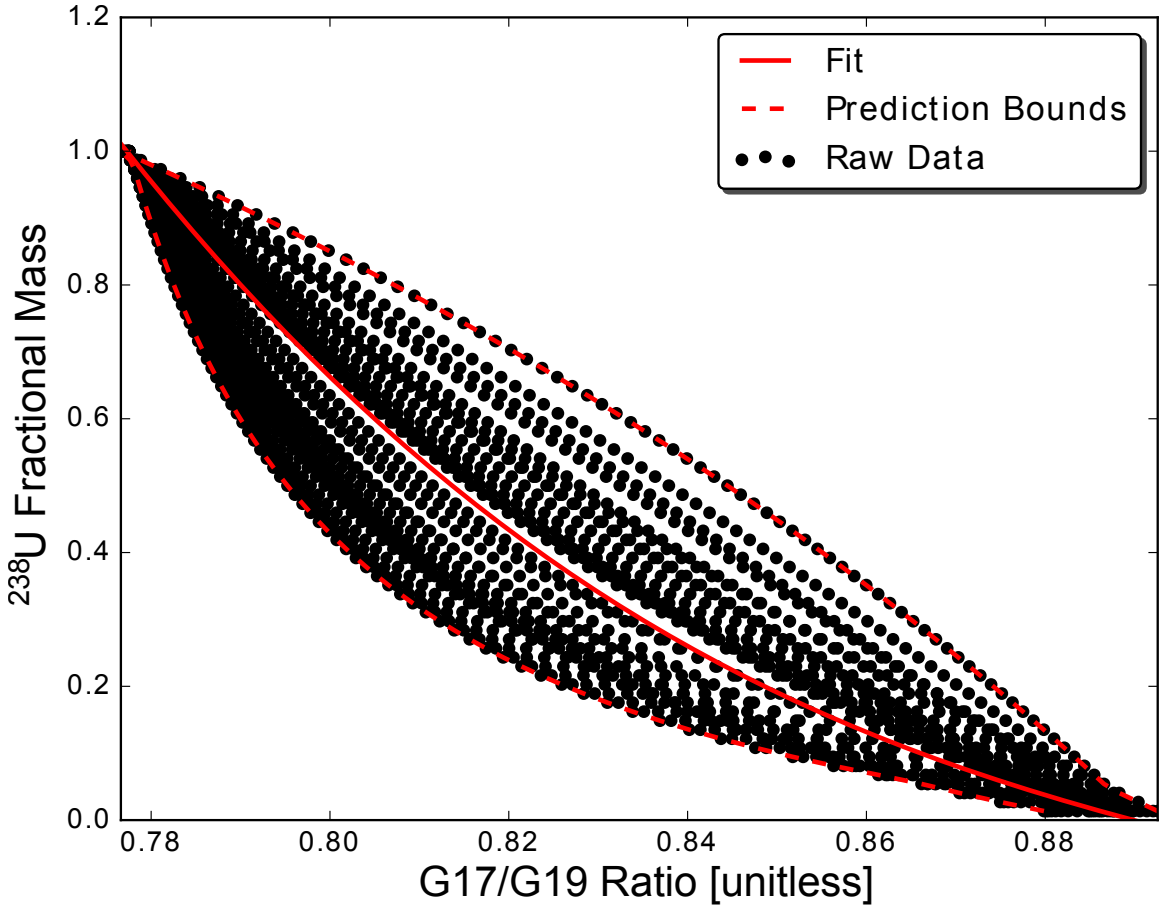


Figure 3.33: $^{238}$U fractional mass from the $\frac{G17--2.35-2.50MeV}{G19--2.00-2.15MeV}$ ratio with associated prediction bounds.

Table 3.8: $^{239}$Pu sensitivity "purity" calculated from $S_i$ and $S_T$ values.

| Energy Range [MeV] | Purity |
|---|---|
| 3.000E+00 - 2.750E+00 | 0.0912 |
| 1.660E+00 - 1.570E+00 | 0.000354 |

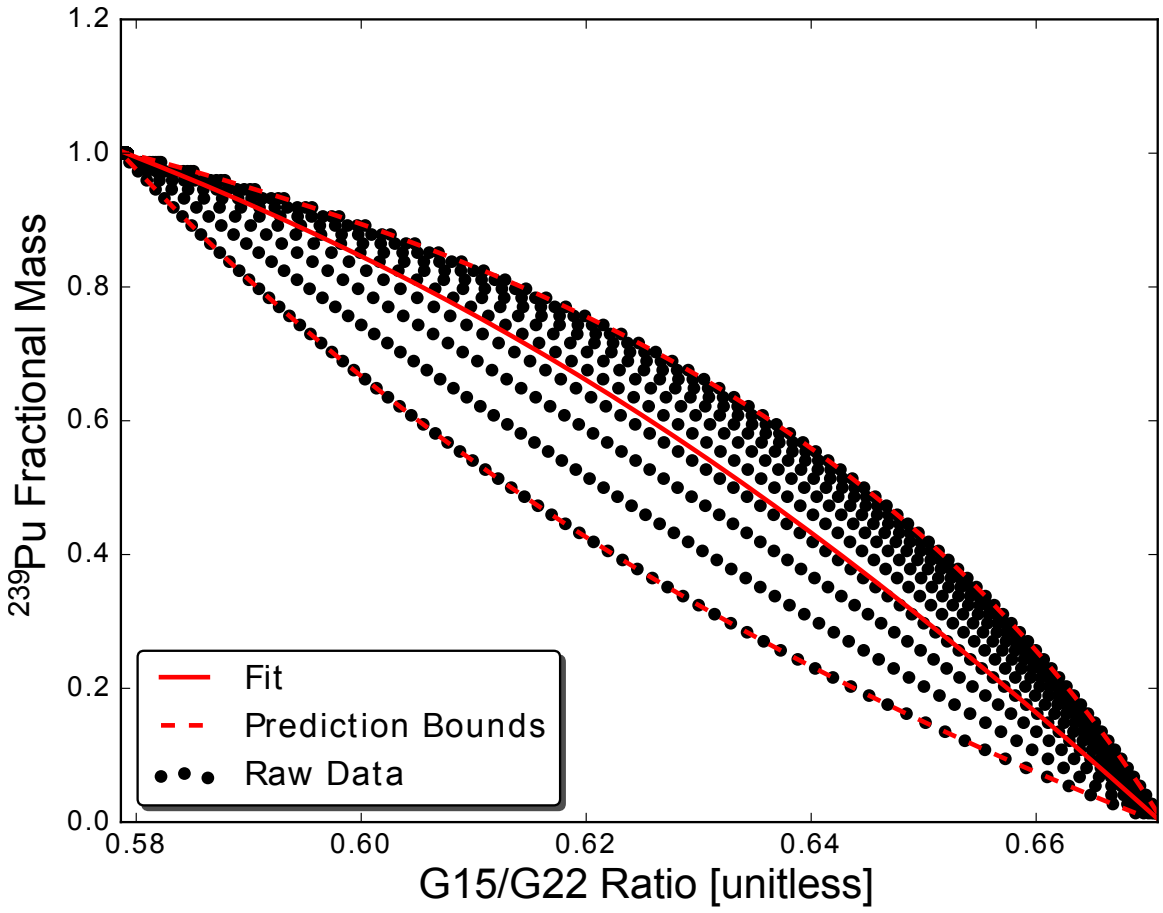


Figure 3.34: $^{239}$Pu fractional mass from the $\frac{G15--2.75-3.00MeV}{G22--1.57-1.66MeV}$ ratio with associated prediction bounds.

The patterns shown in Figs. 3.31-3.34 are a result of the stratified sampling employed. Stratified sampling was used to cover the entirety of the input space with proportionately varying masses and flux values. Statistically including the predictive bounds in the above figures allows a fuel fractional mass distribution to be obtained with no prior knowledge of the flux. Simply, the uncertainty in the flux requires an upper and lower bounded function. Also, values of zero fractional mass were omitted from the fits. Removal was due to the well behaved trend of zero values - no interference with bounds or average values. Table 3.9 shows the predicted values for the two reference cases.

Table 3.9: Monte Carlo Filtering acceleration fractional mass results for Fat Man (FM) and Little Boy (LB) reference cases.

| Nuclide - Reference Case [Ratio] | Lower Limit | Average | Upper Limit |
|---|---|---|---|
| $^{233}$U - FM [G29/G31] | -0.0744 | -0.0536 | -0.0257 |
| $^{233}$U - LB [G29/G31] | -0.2946 | -0.1747 | -0.07246 |
| $^{235}$U - FM [G20/G21] | 0.0307 | 0.0475 | 0.0657 |
| $^{235}$U - LB [G20/G21] | 0.6141 | 0.7736 | 0.8372 |
| $^{238}$U - FM [G17/G19] | -0.0173 | -0.0138 | 0.1065 |
| $^{238}$U - LB [G17/G19] | 0.0257 | 0.0577 | 0.1887 |
| $^{239}$Pu - FM [G15/G22] | -0.0744 | -0.0536 | -0.0257 |
| $^{239}$Pu - LB [G15/G22] | -0.0496 | -0.0324 | -0.0149 |

Logically, unanimous negative values indicate absence of that fuel type. The negative values stem from removal of the zero values from the fitting function. The fractional mass is a bounded function between zero and one, but the function used for fitting is not bounded between these limits. Including zeros would require a sigmoidal fitting function which increases uncertainty in the fit. Nevertheless, zero values are possible for the above fits but are omitted because there is no overlap with the main fitting function. If overlap occurred, fitting bounds would increase and possibly include values between zero and one, irrespec-

tive of the fit. Any values above or below these limits lie outside the parameter space. Results in Table 3.9 are used to accelerate the MCF algorithm.

Interpretation of the above results requires some prior knowledge of the methods and physics. The ORIGEN module used for the acceleration scheme irradiates a point-source of fuel or fuel mixture. During this time period, fission product photon emission contributes to the signal in these energy bins. These fission products originate from fission events or mass to energy conversions. Because ORIGEN irradiates the fuel(s) equally (in this case), the fractional mass can be thought of as fractional fissions or the isotope most contributing to the fission product inventory/photon emissions.

*Accelerated Monte Carlo Filtering Results*

Acceleration results allowed for input space reduction to expedite the MCF algorithm. A stratified sampling technique was used to sample from different fuel, reflector, and densities for complete coverage. The grading scheme described in Sec. 3.2 was used on all samples. At the onset of the MCF algorithm, smaller sample sizes were sampled to further narrow down the possible configurations.

The Fat Man like configuration contained 6.2 kilograms of pure $^{239}$Pu and 100.0 kilograms of $^{Nat}$U. Running the abbreviated sampling space with loosened scoring requirements yielded matches for WGPu, pure $^{239}$Pu, and FGPu all with $^{Nat}$U reflectors. The algorithm was then run on the specific configurations with tightened scoring and more samples. Results are shown in Table 3.10. WGPu, pure $^{239}$Pu, and FGPu results have been combined for all calculated estimates.

Table 3.10: Monte Carlo Filtering algorithm results for Fat Man configuration. Weighted and non-weighted estimates of fuel and reflector mass, yield, height-of-burst, and density.

| | $^{239}$Pu/$^{Nat}$U | $^{239}$Pu/$^{Nat}$U (HOB Weighted) |
|---|---|---|
| Fuel Mass [kg] | $6.84 \pm 1.17$ | $6.84 \pm 1.18$ |
| Reflector Mass [kg] | $112.66 \pm 24.23$ | $112.68 \pm 24.23$ |
| Yield [kt] | $15.37 \pm 0.93$ | $15.37 \pm 0.93$ |
| HOB [cm] | $10226.72 \pm 206.92$ | $10226.57 \pm 207.06$ |
| Density [$\frac{g}{cm^3}$] | $31.60 \pm 3.59$ | $31.60 \pm 3.59$ |

The weighted and non-weighted averaged estimates shown in Table 3.10 encompass the "true" values of the reference case. The height-of-burst (HOB)/cloud rise module (CRM) calculation uses the same scoring system but requires tedious calculation involving a system of ODE equations. Peri-detonation HOB/CRM calculations were run between 3.0 and 60.0 seconds. Because of the computational intensity of these calculations, the CRM calculation commences after the initial burn period has been scored and passed. The CRM/HOB calculation uses the same scoring system, the scores of the calculation serve as weights to the non-weighted averaged values. With unlimited resources, many different configuration combinations would earn a passing score but the HOB calculation would further eliminate the erroneously matched configurations. Essentially, the CRM/HOB calculation provides a secondary check to the matched configurations and increases accuracy. The CRM/HOB weighting/filtering scheme did not change the matched values because of the front-end time period scoring accuracy. Optimistically, the CRM/HOB weighting scheme and data could be used if prompt measurements were not available.

Table 3.11 shows the Little Boy configuration results. The Little Boy configuration did not contain a reflector. Yield and HOB results are spread over a large area and contain significant error. The high error is attributed to the bare fuel with no reflector. More of the photon emissions are escaping the assembly which immediately floods the detector even at

small power levels. Conversely, the fuel mass matched closer to the true mass and addition of the HOB weighting scheme decreased the associated error.

Table 3.11: Monte Carlo Filtering algorithm results for Little Boy configuration. Weighted and non-weighted estimates of fuel and reflector mass, yield, and height-of-burst.

| | $^{235}$U/Air | $^{235}$U/Air (HOB Weighted) |
|---|---|---|
| Fuel Mass [kg] | 45.06 $\pm$ 4.72 | 44.87 $\pm$ 5.18 |
| Reflector Mass [kg] | N/A | N/A |
| Yield [kt] | 104.86 $\pm$ 114.52 | 109.82 $\pm$ 118.42 |
| HOB [cm] | 18139.58 $\pm$ 5359.15 | 18258.86 $\pm$ 5843.24 |

At first glance, the results presented in Table 3.11 are less reliable and provide little information. Using the score obtained during the CRM period, the results can be filtered down by only accepting the results with passing grades. The results are then closer to the true values shown in Table 3.12. Applying the secondary CRM filter emphasizes the ability to use scores from 2 time periods in order to narrow conclusions. If prompt or front-end data is not available, the back-end CRM period can be used to deduce device characteristics.

Table 3.12: Monte Carlo Filtering algorithm results for Little Boy configuration following secondary cloud rise module scoring requirement. Weighted and non-weighted estimates of fuel and reflector mass, yield, and height-of-burst.

| | $^{235}$U/Air | $^{235}$U/Air (HOB Weighted) |
|---|---|---|
| Fuel Mass [kg] | 39.07 $\pm$ 1.51 | 39.08 $\pm$ 1.52 |
| Reflector Mass [kg] | N/A | N/A |
| Yield [kt] | 11.71 $\pm$ 1.68 | 11.79 $\pm$ 1.66 |
| HOB [cm] | 12429.16 $\pm$ 612.46 | 12457.34 $\pm$ 602.18 |

The MCF algorithm matched Fat Man and Little Boy derivative designs with different confidence levels. Further investigation of the Little Boy design derivative CRM scores in-

creased confidence levels by only accepting "passing" scores ($> 90\%$). The less confident initial results of the Little Boy design derivative are subtly informative. The bare assembly allowed more emissions to escape which saturated the "detection system." In fact, the time steps used for the MCF algorithm were less granular, mimicking a lower quality detection system, which inherently produced less accurate results. The subsequent signatures emanating from the CRM back-end period allowed the results to be filtered, increasing accuracy. The increase in accuracy from the back-end period reveals that early-time distinguishable signatures exist during nuclear cloud rise. Also, the Fat Man derivative design MCF results were more accurate with the less granular time steps. The lack of granularity and high accuracy indicate the possible use of a less sophisticated detection system.

# CHAPTER 4
# PERI-DETONATION EXPERIMENTAL TECHNICAL APPROACH AND RESULTS

Detector technology is a critical factor when considering peri-detonation photon emission due to the short emission time scales and intensities. Detector limitations ultimately constrain the amount of information available at early times. Determining and displaying these limitations allows the researcher to choose the best detection system for the given conditions maximizing the amount of information available for policy maker consideration.

## 4.1 Relevant Detection Equipment and Data Acquisition

There are many different detector types available for photon detection including inorganic/organic scintillators and semiconductors. For this research, EJ-309 and $LaBr_3$(Ce) scintillation and High Purity Germanium (HPGe) semiconductor detectors are examined. The associated properties of these detection systems and the electronics used to process the signal are important because of short time scales of peri-detonation emissions.

### 4.1.1 Radiation Detectors

The multitude of available detector types allows for selection based on environmental and emission conditions. One such type, scintillation detectors, have been used over many years for photon detection. Light produced from the scintillation process is one of the oldest methods for detecting radiation. Inorganic scintillators are the most popular because of high scintillation light output and linearity [34]. Table 4.1 displays some popular inorganic and organic scintillator properties.

Table 4.1: Popular scintillators and properties potentially used in photon detection [35].

| Property | LYSO | BGO | CsI | LaBr | NaI | EJ-309 | $CdWO_4$ | EJ-299-34 | Stilbene |
|---|---|---|---|---|---|---|---|---|---|
| Density (g/cm$^3$) | 7.15 | 7.13 | 4.51 | 5.10 | 3.67 | 0.96 | 7.90 | 1.08 | 1.15 |
| Decay time (ns) | 42 | 300 | 980 | 30 | 250 | 3.5 | 12,000 | 13, 35, 270 | 4.50 |
| Intrinsic Radioactivty | Yes | No | No | Yes | No | No | No | No | No |
| Hygroscopic | No | No | No | Yes | Yes | N/A | No | No | Yes |
| Luminosity (photons/MeV) | 24,000 | 8,000 | 55,000 | 75,000 | 45,000 | 12,300 | 7,800 | 8,600 | 8,700 |
| Energy resolution (@ 661 keV) | 7.1% | 12% | 5.7% | 2.9% | 7.0% | >20% | >20% | >20% | >20% |
| Reference | [36] | [37] | [38] | [39] | [40] | [41] | [42] | [43] | [44] |

For peri-detonation photon detection, the properties listed in Table 4.1 are all important. A high density, fast decay time, and high light yield offer the best properties for peri-detonation detection. From examination of the properties, the $LaBr_3$(Ce) detector offers the best properties for peri-detonation application due to the high density, fast decay time, and high light output. The drawback of this detector is the intrinsic radioactivity from $^{138}La$ which occurs $0.09\%$ naturally and $^{227}Ac$ resulting in approximately 1-2 $\frac{counts}{cm^3-second}$ [34]. Because of the rapid photon emission from a prompt event, this characteristic hinders capturing most of the events attributed to the device. Pulses registered from intrinsic radioactivity prevent other pulses from the device to be registered, if falling within the pulse integration time.

Scintillation detectors offer several advantages for peri-detonation detection. Unfortunately, scintillation detectors have poor energy resolution because the inefficiency in converting radiation energy to electrical signal. Semiconductor detectors overcome this inefficiency and offer superior energy resolution. A drawback of semiconductor detectors is susceptibility to signal degradation from radiation damage [34]. Because of availability, this research employed a HPGe detector. Peri-detonation would require the detector to be present in the field at the time of the event. This presents another drawback for an HPGe detector. The detector must be cooled to a temperature of around 77 K because of the small bandgap (0.7 eV). Higher temperature operation would produce high leakage current [34].

### 4.1.2 Detection Electronics

The electronics used were developed by Costruzioni Apparecchiature Elettroniche Nucleari S.p.A. (CAEN). The digitizers employed were the DT5730 and DT5780. $LaBr_3$(Ce) and EJ-309 detectors were run through the DT5730 while the HPGe utilized the DT5780. Important features of the DT5730 and DT5780 were the high number of channels (8) and the sampling rate of 500 Megasamples (MS)/second and 100 Megasamples/second, respectively. The high sampling rate is important in rapid pulse processing required for

peri-detonation emissions. The digitizers also contain multiple algorithms for digital pulse processing (DPP) including pulse-shape discrimination (PSD) and pulse-height analysis (PHA). Pulse-shape discrimination allows for categorization of photon versus neutron events in the detector. This characteristic becomes important in $LaBr_3$(Ce) and EJ-309 detectors where neutron events are possible.

In the case of organic scintillators (e.g. EJ-309), prompt fluorescence dominates the produced scintillation light with smaller contributions originating from delayed fluorescence. The prompt decay time is within a few nanoseconds while delayed decay spans approximately several hundred [34]. This decay time becomes important when the delayed component is examined. Conveniently, the fraction of light appearing in the delayed component is related to the nature of the excited particle [34]. Neutrons will inherently have larger delayed tails with photons creating smaller delayed tails. This aspect is leveraged by setting a long and short-gate integration areas for capturing neutron and photon pulses, respectively. This setting is shown in Figure 4.1. For peri-detonation, the passively measurable emissions include neutrons and photons which travel further in air and readily interact in organic scintillators.

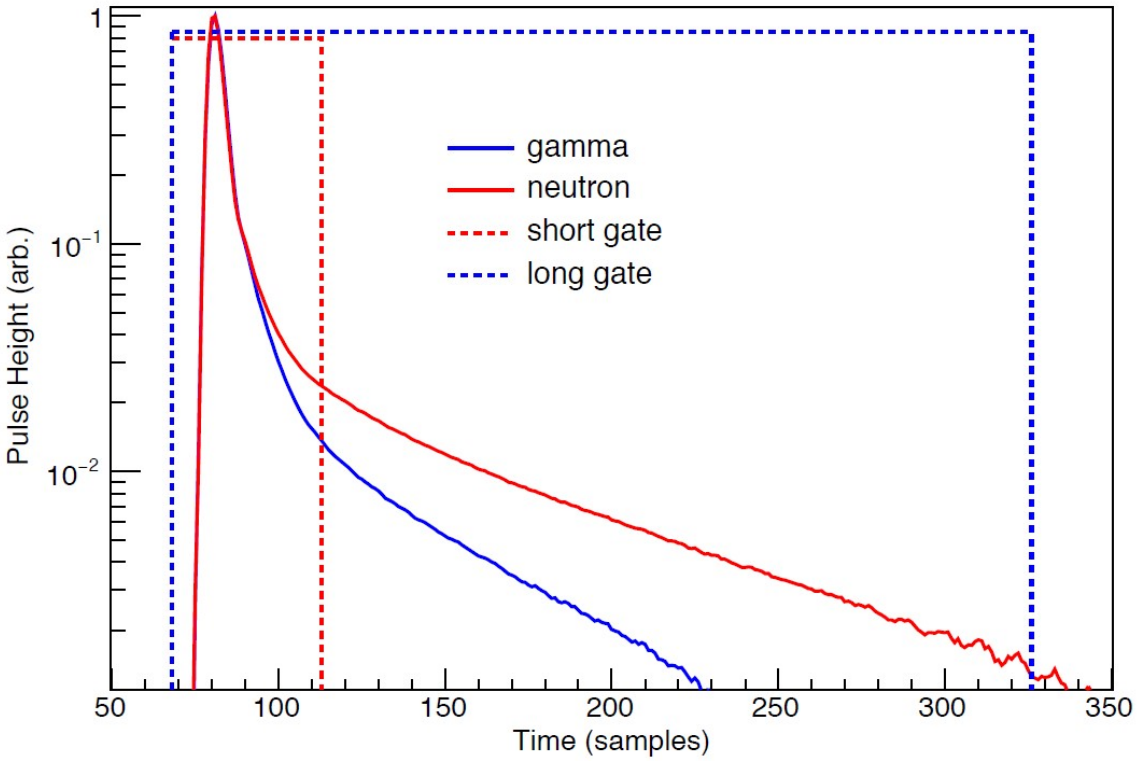


Figure 4.1: Short (photon) and long-gate (neutron) setting depiction for pulse shape discrimination. Ratio of the two gates yields groupings of photon or neutron interactions.

The amount of energy output from prompt neutron and photon emission between fissile materials differ noticeably. For example, photon energy output was 0.0216% and 0.265% for Hiroshima and Nagasaki devices which were primarily $^{235}U$ and $^{239}Pu$ fuels, respectively. The neutron energy outputs were 0.127% and 0.0078% for Hiroshima and Nagasaki [22]. These are exploitable differences relevant to peri-detonation detection.

## 4.2 Pertinent Peri-Detonation Detection Phenomena

Several physical factors exist that make peri-detonation detection challenging. The time scale of the reactions that produce the measurable output is extremely short. Within this short time scale, other competing mechanisms and emissions conflict with the desired measurement. Also, current knowledge of the underlying nuclear reactions driving the high energy output is limited which confuses attributing prompt emissions with a specific physical

mechanism.

### 4.2.1 Reaction and Detection Timing

The diminutive emission time presents the biggest challenge for peri-detection detection. For perspective, 99.9% of a 100 kiloton energy release is obtained in the last 7 neutron generations or approximately 0.07 microseconds equating to 1.00E-08 $\frac{seconds}{generation}$. The total time for a 100 kiloton energy release is approximately 58 generations or 5.80E-07 seconds [3]. This energy release acceleration produces a rapid expansion and the reaction halts due to the increased neutron leakage.

Of the inorganic scintillation detectors, $LaBr_3$(Ce) offers the lowest decay time at 2.60E-08 $\frac{seconds}{pulse}$. The decay time does not include the integration time of the pulse. This research used a 3.36E-07 $\frac{seconds}{pulse}$ integration time. The inverse integration time, 2.98E+06 $\frac{pulses}{second}$, is an upper rate limit of detectability for the $LaBr_3$(Ce) detector. An idealistic example, if 1.00E+20 monoenergetic $\frac{photons}{second}$ were incident on a 100% efficient $LaBr_3$(Ce) detector, 2.98E+06 photons would be detected over a period of 1 second. If the intrinsic radioactivity, 1.5 $\frac{counts}{cm^3-second}$(173.75 $cm^3 - second$) = 260.62 counts, is taken into account this number drops further but not significantly. Detectors with higher decay/integration times lose more prompt fission and activation signatures from the device.

### 4.2.2 Fission Process

The main driver of nuclear energy is the fission process. Fission prompt energy distribution originates from kinetic energies of fission fragments — 165 ± 5 MeV and fission neutrons — 5 MeV, and prompt photons — 6 ± 1 MeV. These byproducts are converted into recoverable heat energy [45]. A typical fission reaction is shown below.

$$^{235}_{92}U + ^{1}_{0}n \longrightarrow ^{236}_{92}U^{*} \longrightarrow ^{95}_{42}Mo + ^{139}_{57}La + 2n$$

Above, $^{235}_{92}U$ absorbing a thermal neutron produces an excited $^{236}_{92}U$ intermediate product before separation. In this case, the excitation energy comes from the unpaired neutron separation energy in $^{235}_{92}U$ plus the absorbed energy from the projectile or thermal neutron.

The kinetics and timing of the fission process can be further explained. Upon excitation, $^{236}_{92}U^*$ in the above case, the nucleus is deformed and fragments at around $10^{-14}$ seconds which creates two neutron rich fragments. These fragments emit the excess neutrons at approximately $10^{-17}$ seconds post-fission followed by prompt photons at 2x$10^{-14}$ seconds post-neutron emission. Once the fragments stop in the medium they are known as fission products which release the remaining delayed fission energy in the form of $\beta$ particles — $8 \pm 1.5$ MeV, antineutrinos — $12 \pm 2.5$ MeV, and photons — $6 \pm 1$ MeV [45].

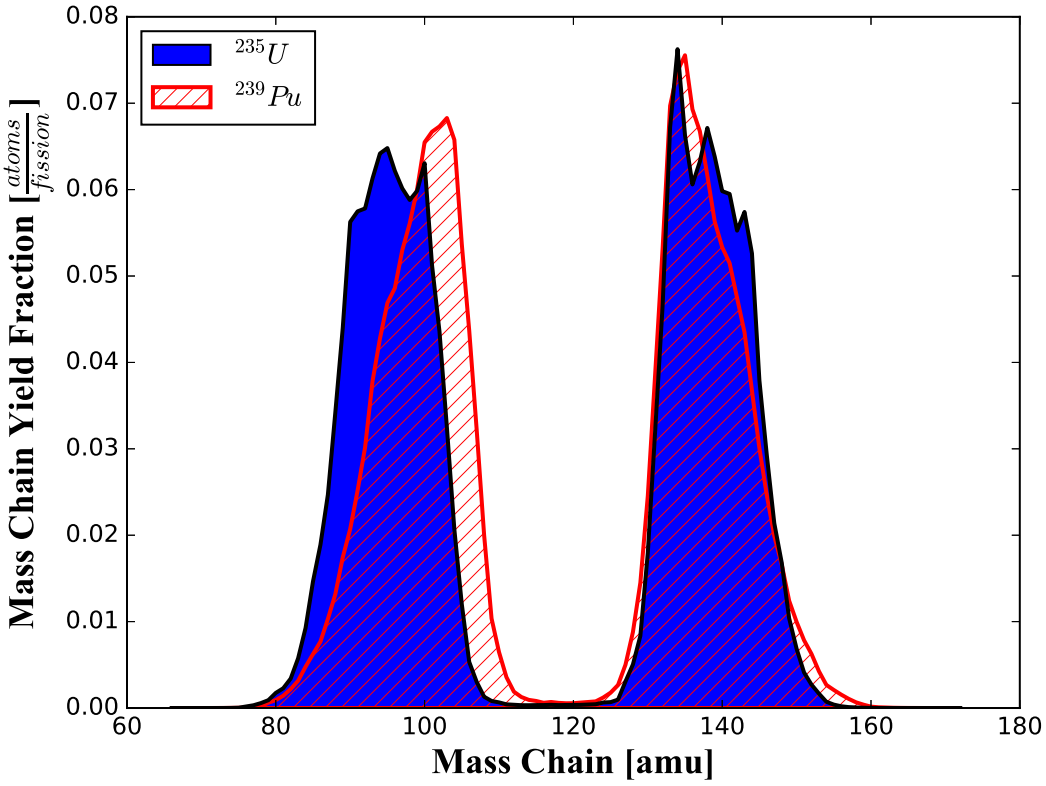


Figure 4.2: Fission product mass chain yields for 2.0 MeV neutrons incident on $^{235}U$ and $^{239}Pu$.

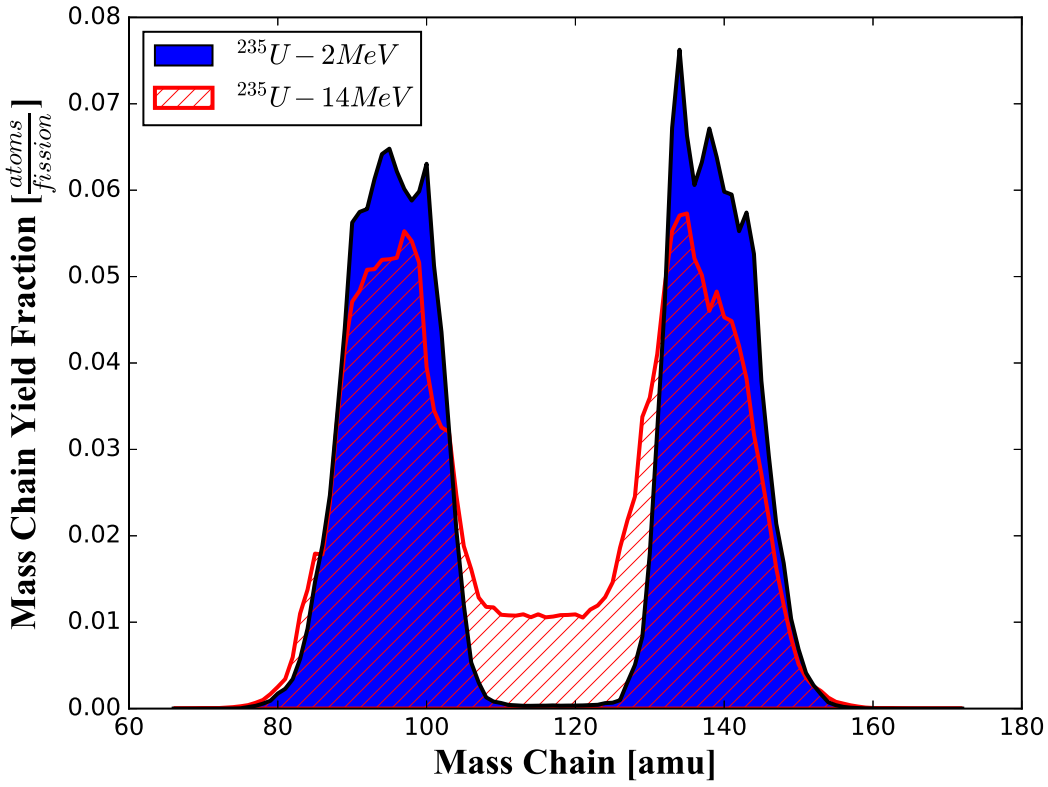


Figure 4.3: Fission product mass chain yields for 2.0 and 14.0 MeV neutrons incident on $^{235}U$.

Figures 4.2 and 4.3 show fission product mass chain yield distributions. The differences between these yield curves are due to the fissile/fissionable targets and the incident neutron energies. These subtle differences reveal clues into device characteristics.

All the recoverable energy is important in peri/post-detonation nuclear forensics. Other forms of prompt radiation relevant in peri-detonation detection are radiative capture and inelastic scatter of neutrons in the device components. Parasitic absorption leads to recoverable photon energies totaling approximately 12 MeV [45].

### 4.2.3 Inelastic Scatter/Radiative Capture Process and Emission

Because there is a distribution of neutron energies within a nuclear device, parasitic capture and inelastic neutron scatter will produce prompt photons. Inelastic scatter is prevalent

when fast neutrons are present while radiative capture will occur with lower energy neutrons. Higher energy neutrons inelastically scatter off a nucleus producing an excited state that emits a characteristic prompt photon and inherently lowers the scattered neutron energy [46]. These lower energy neutrons can be removed by radiative capture process. Once a neutron is captured, the excited nucleus can de-excite by several processes. De-excitation can occur by re-emission of the neutron but heavy nuclides and low energy neutrons causes suppression of this decay mode and photon emission dominates [47]. Neutron capture photon emission spectrum consists of a primary and secondary component. Primary is direct emission from the capture state to the lower excited states while secondary is low-energy emission from those lower excited states [47]. In the case of peri-detonation, heavy nuclides are abundantly present and the neutron distribution contains low and high energy neutrons making prompt activation and inelastic scattering a competing process in a nuclear device. For this application, fission, prompt activation, and inelastic scatter photons are unresolvable because of the detection system's ability to resolve this short time scale; hence, contributing to the detector signal simultaneously.

## 4.3 Experimental Setup

The experimental setup was designed to examine the prompt reactivity insertion from a Deuterium-Tritium (DT) fusion neutron source on fissile/fissionable targets and the resulting prompt photon/neutron emissions. The DT source emits approximately 1.0E+08 14-MeV-neutrons/second with a pulse rate and width of 100 pulses/second and 10 microseconds, respectively.

Fissile/fissionable targets consisted of $^{238}$U, $^{239}$Pu, $^{237}$Np, and a mix of $^{238}$U and $^{239}$Pu. $LaBr_3$(Ce), EJ-309, and HPGe detectors were placed at 90 degrees relative to the target and source beam line. To reduce room scatter, the DT source was surrounded with 5-20$\%$ borated polyethylene and the detectors were surrounded with lead bricks. Views 1 and 2 show positioning of the DT source and detectors and shown below in Figs. 4.4 and 4.5.

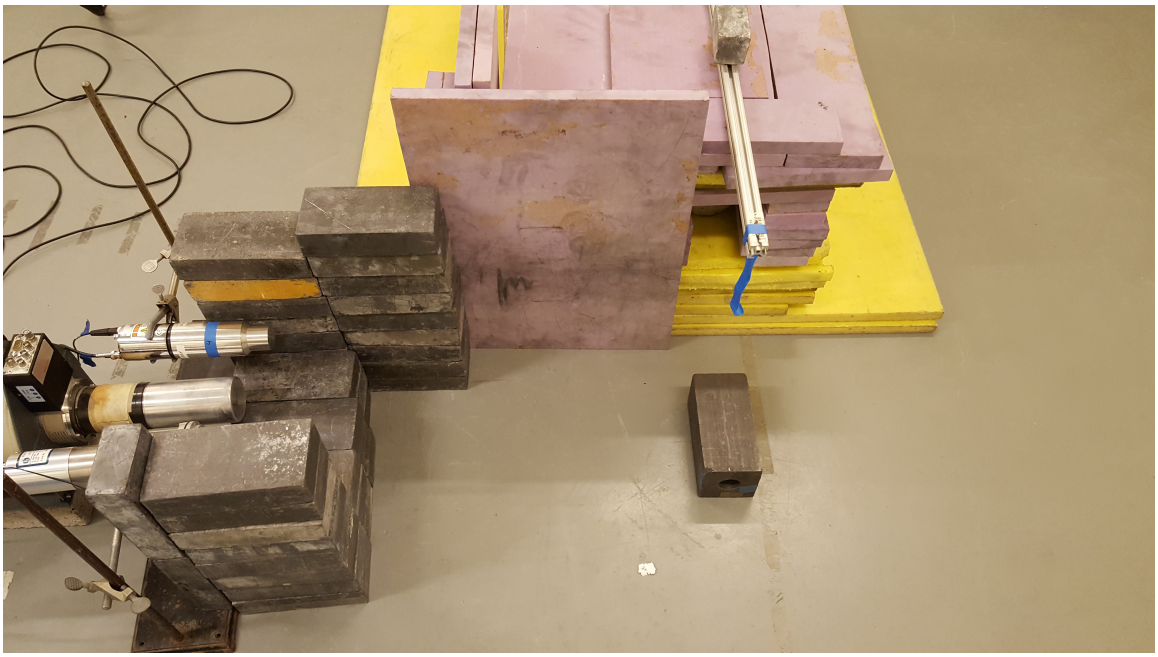

Figure 4.4: View 1 of prompt photon/neutron emission experimental setup.

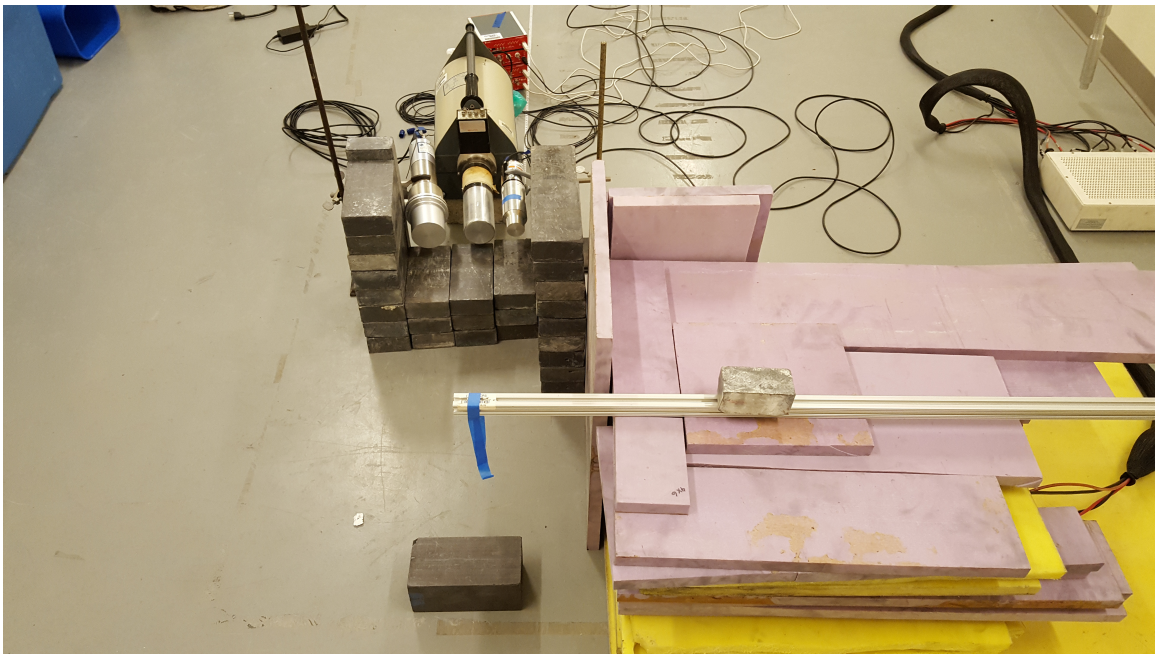

Figure 4.5: View 2 of prompt photon/neutron emission experimental setup.

Fissile/fissionable targets used were $^{239}$Pu, $^{237}$Np, and $^{Nat}$U. The $^{239}$Pu and $^{Nat}$U targets were also combined and irradiated to show the change in photon/neutron emissions. The $^{Nat}$U target slugs weigh 1.92 kilograms each and are encased in aluminum cladding [48].

$^{239}$Pu and $^{237}$Np targets weighed 5 and 0.5 grams, respectively. The four configurations irradiated are shown in Table 4.2.

Table 4.2: Irradiated fissile/fissionable configurations.

| | $^{239}$Pu [grams] | $^{Nat}$U [grams] | $^{237}$Np [grams] |
|---|---|---|---|
| Config. 1 | 5.0 | 0.0 | 0.0 |
| Config. 2 | 5.0 | 3844.6 | 0.0 |
| Config. 3 | 5.0 | 17300.8 | 0.0 |
| Config. 4 | 0.0 | 17300.8 | 0.0 |
| Config. 5 | 0.0 | 0.0 | 0.5 |

## 4.4 Detection Rate Comparisons

$LaBr_3$(Ce) and EJ-309 detectors used the 5730 digitizers which acquired 500 MS/second while the HPGe detector employed the 5780 version acquiring 100 MS/second. The sampling rate is important for peri-detonation nuclear forensics because of the rapid progression of emission events. The 500 MS/second equates to 2 nanoseconds/sample while the 100 MS/second equates to 10 nanoseconds/sample.

The DT source has a pulse frequency of 100 Hertz with a pulse width of 10 microseconds. With respect to the pulse frequency, the 500 MS/second and 100 MS/second equates to 5E+6 and 1E+6 samples/pulse, respectively. The 10 microsecond pulse width equates to 5000 and 1000 samples acquired over the width of the pulse. The 500 MS/second sampling rate captures 5 times more data than the 100 MS/second sampling rate.

### 4.4.1 EJ-309 Rate Results

EJ-309 detectors have the ability to detect neutrons and photons because of the composition and setting of the short and long gate integration times known as pulse shape discrimina-

tion (PSD). Distinguishing between neutron, photon, and pile-up events are important in determining characteristics of the source.

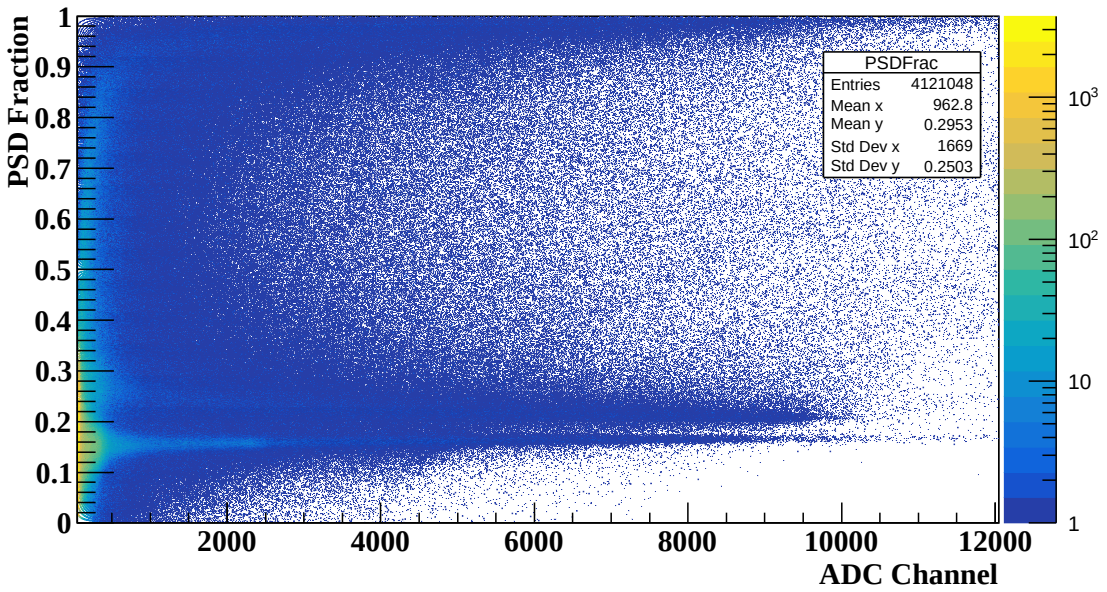


Figure 4.6: Aggregated pulse shape discrimination fraction distribution from pulsed experiment.

Examining and segregating the lobes found in Fig. 4.6 allows for discrimination of neutron, photon, and pile-up events. Pile-up is important for aggregating rates of emission. A pile-up event is determined if the PSD fraction value is outside of the neutron/photon areas or lobes. The pile-up event is conservatively counted as 2 pulses. In reality, this number could be higher but is hard to determine unless waveform data is available. Total neutron and photon emission rates can also be determined by counting only events that are within the PSD fraction bounds. Figs. 4.7 and 4.8 show the neutron and photon emission rates over time.

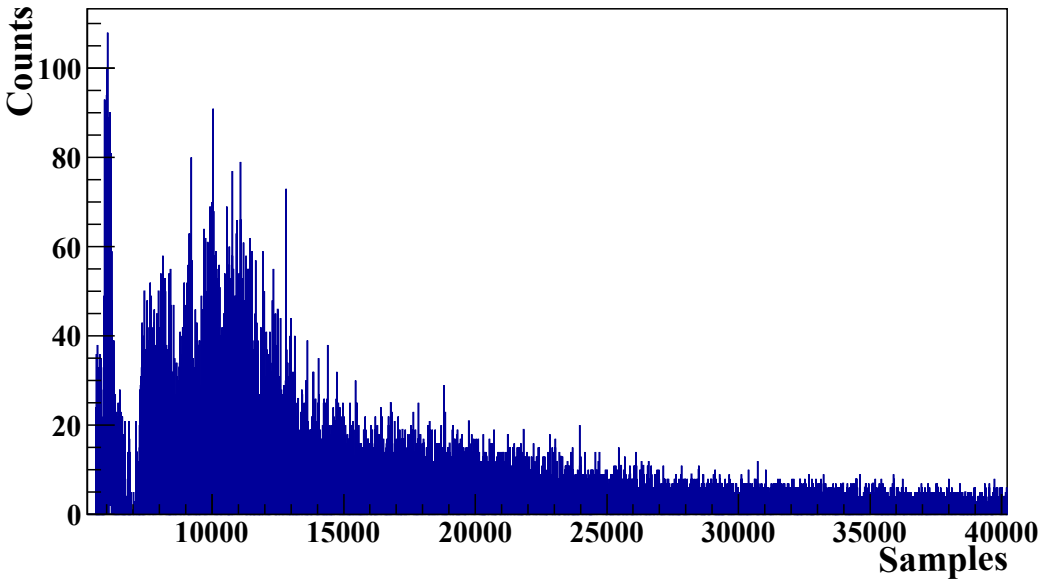


Figure 4.7: Neutron emission rate using an EJ-309 detector with $^{Nat}$U slugs as targets.

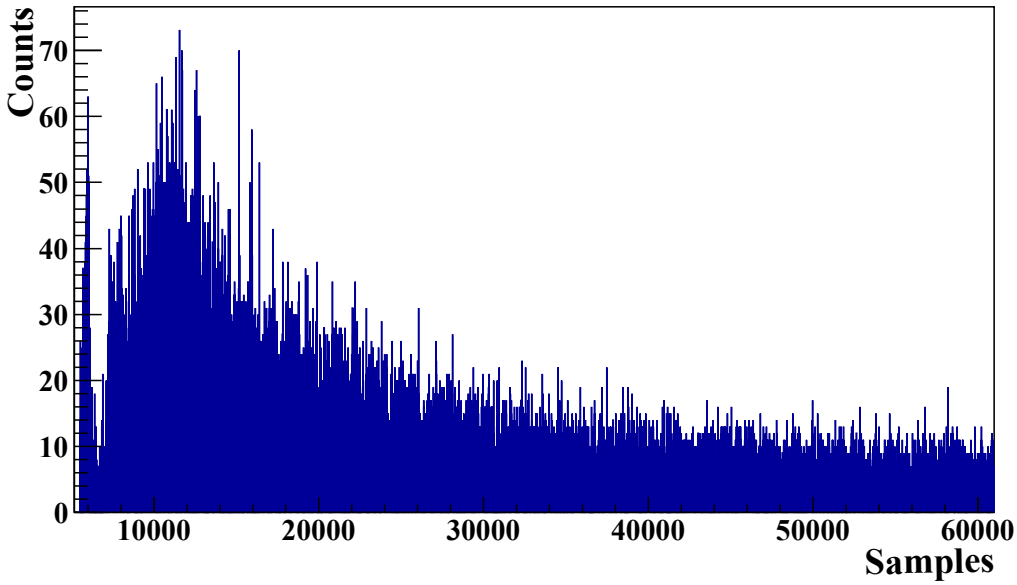


Figure 4.8: Photon emission rate using an EJ-309 detector with $^{Nat}$U slugs as targets.

Because of the low decay time and sampling rate, EJ-309 detectors clearly show the pulse shape of the DT source. The capability is also shown if the pulse time - time of fission - is integrated yielding a photon energy distribution. The magnitude of events hitting the detector is exaggerated during this time and shows the capability of the detector to handle high rates associated with prompt emissions. This attribute is also displayed in Fig. 4.9 and

the ability to resolve photon energy information in the fission time period or when the DT source is running.

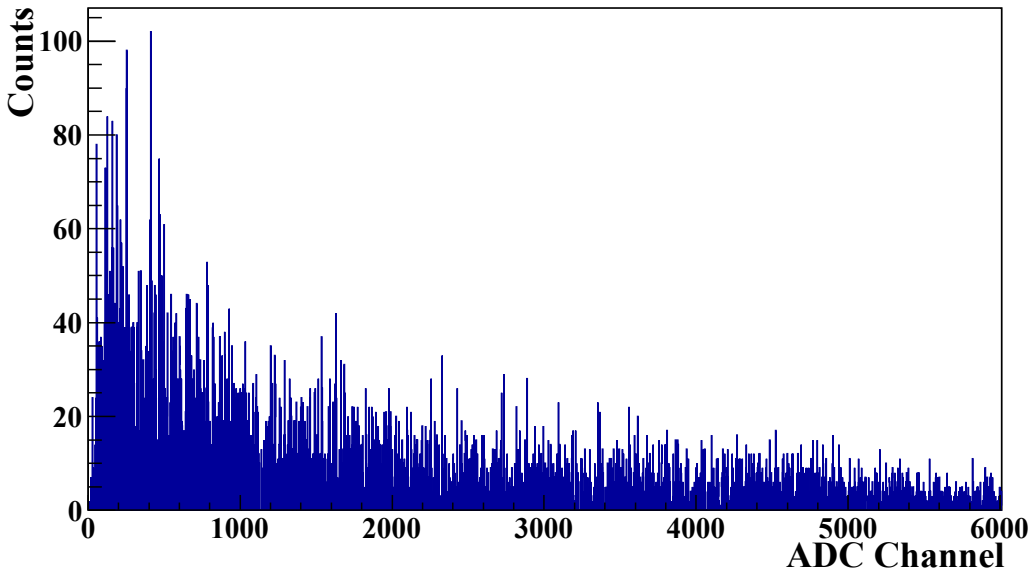


Figure 4.9: Fission photon energy distribution shown by ADC channel using an EJ-309 detector with $^{Nat}$U slugs as targets.

The separability of neutron and photon events permits quantification of time dependent proportional neutron to photon events. Photon and neutron output from fission differ between fissile/fissionable nuclides. This emission signature can be used to strengthen conclusions and results from other detection systems. Characterizing the proportion of neutron to photon events provides a rapid indicator of the dominant fuel type.

Rapid emission rates associated with nuclear detonations require fast detection systems. The EJ-309 detection set-up allows for high rate acquisition and discrimination of neutron/photon events which can be leveraged for gaining fuel-type information by exploiting the differences in neutron/photon output. Unfortunately, the EJ-309 detector lacks energy

resolution but is promising as an adjunct detector. Another candidate for fast detection is the $LaBr_3$(Ce) detector.

### 4.4.2 $LaBr_3$(Ce) Rate Results

Similarly to EJ-309, $LaBr_3$(Ce) has the ability to perform pseudo-PSD. This enables separation into photons and pile-up events as neutron events are less likely. As with EJ-309, a photon rate can be determined by counting events falling within the photon lobe of the $LaBr_3$(Ce). Figure 4.10 shows the photon emission rate from a $^{Nat}$U target.

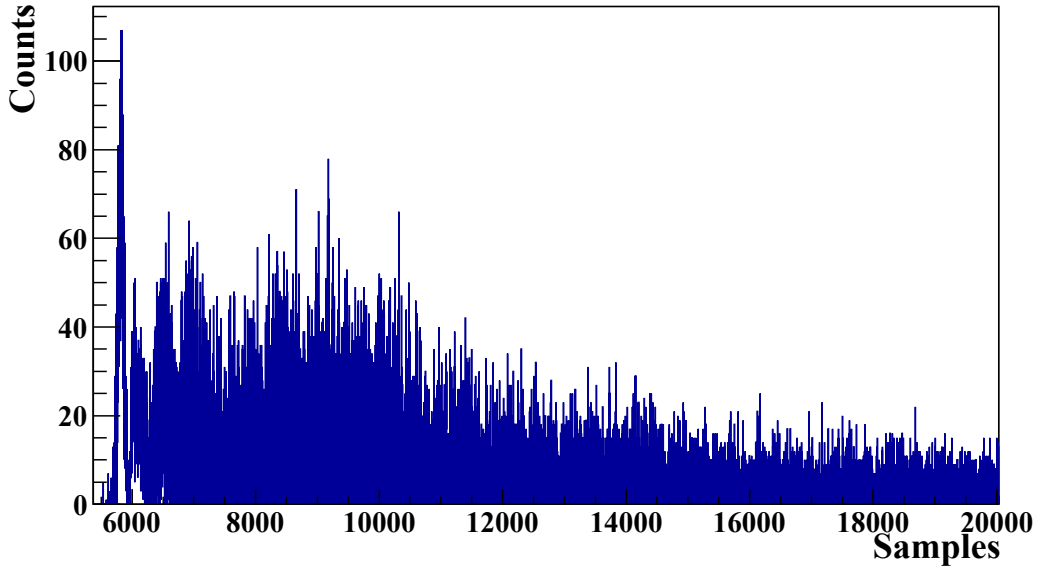


Figure 4.10: Photon emission rate using an $LaBr_3$(Ce) detector with $^{Nat}$U slugs as targets.

More importantly, $LaBr_3$(Ce) excels in high rate environments. Figure 4.11 shows the integrated fission time period with $^{Nat}$U targets. The ability to handle high rates allows for photon energy information to be obtained.

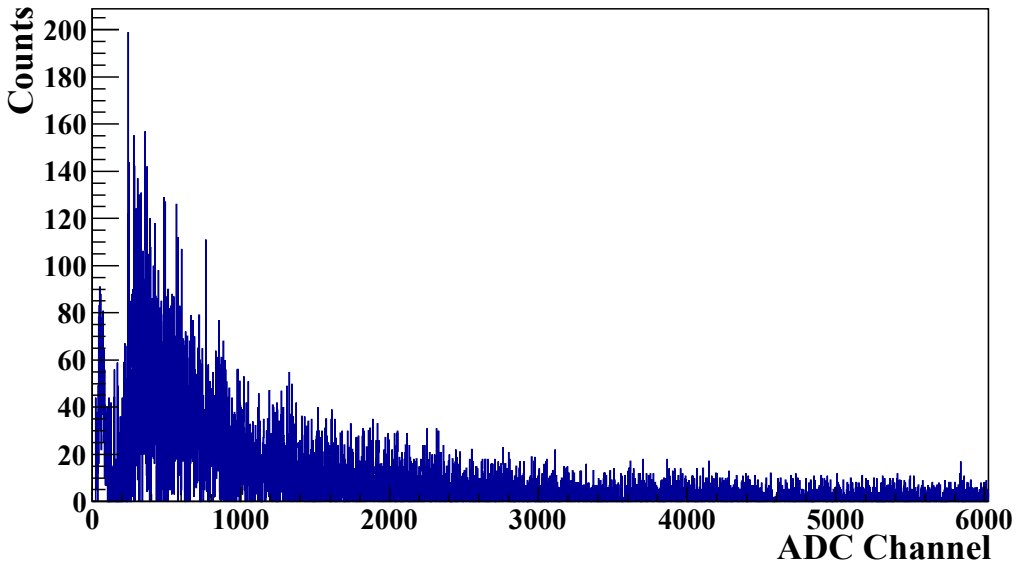


Figure 4.11: Fission energy histogram using an $LaBr_3$(Ce) detector with $^{Nat}$U slugs as targets.

The high-rate capacity coupled to the higher energy resolution (compared to EJ-309) makes this detection system a better candidate for peri-detonation detection. The ability for the detector to obtain energy information at the highest rate period (fission) easily justifies obtaining delayed photon emissions.

### 4.4.3 HPGe Rate Results

The HPGe detection system employed a different digitizer capable of 100 MS/second acquisition. This sampling rate is 5 times less than the digitizers employed with the EJ-309 and $LaBr_3$(Ce) detection systems. HPGe detectors have much longer decay times thus pairing with faster electronics has minimal value for this particular application. Figure 4.12 shows the photon emission rate from the $U^{Nat}$ targets.

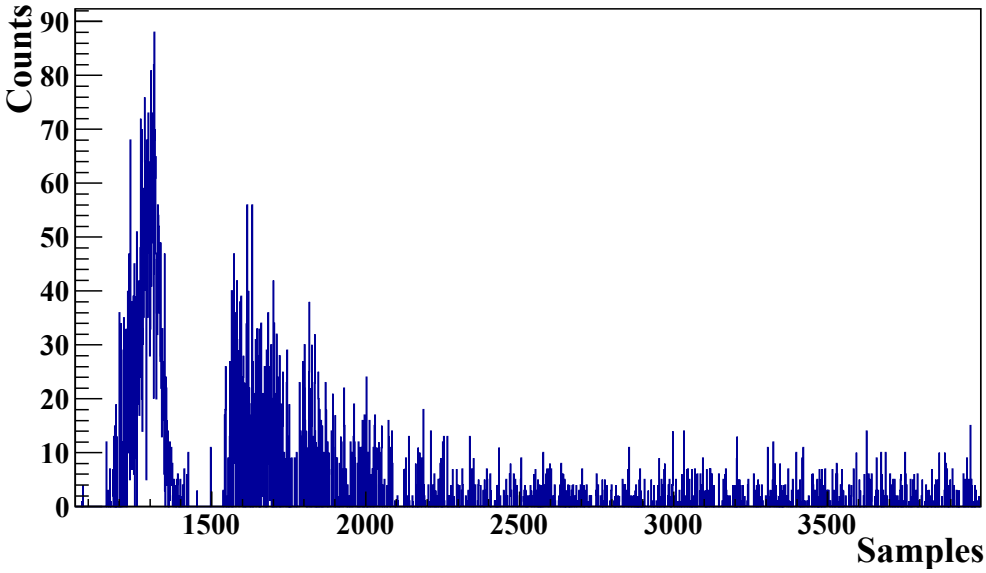


Figure 4.12: Photon emission rate using a HPGe detector with $^{Nat}$U slugs as targets.

The rate of emission is resolvable even with the lower sampling rate. Some detail is lost when compared to the shape obtained in the EJ-309 and $LaBr_3$(Ce) detection systems. This detection system contains a pulse pile-up rejection system bounding the aggregated rate to single photon emissions. The limitation of the HPGe detector is shown in Fig. 4.13.

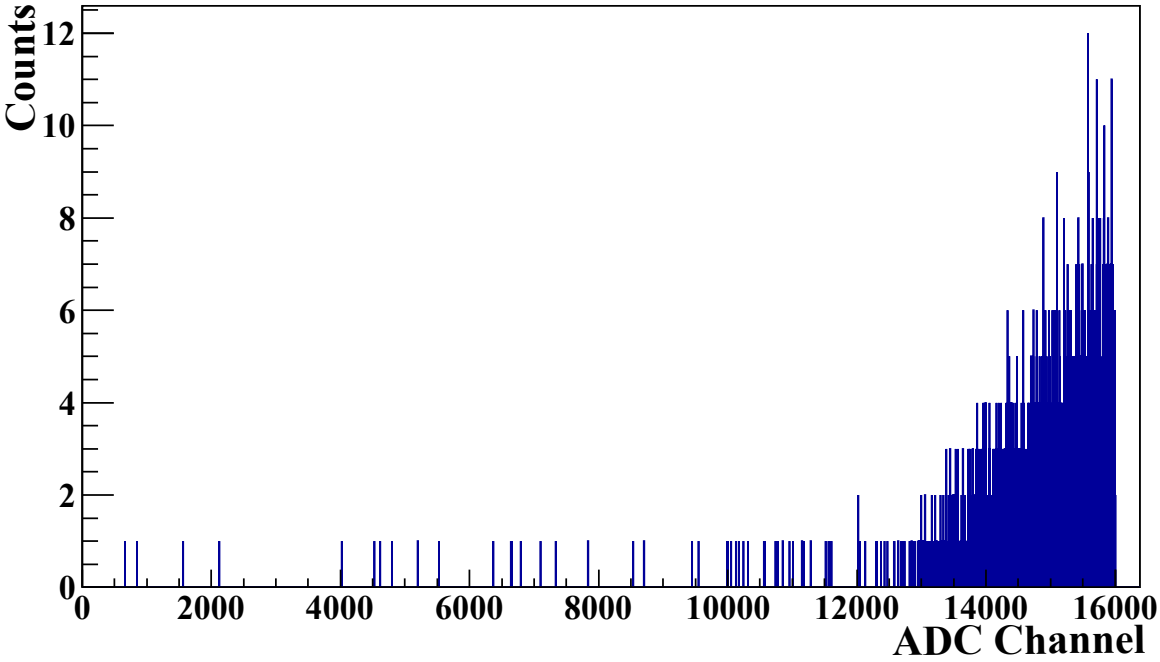


Figure 4.13: Fission energy distribution shown in ADC channel using a HPGe detector with $^{Nat}$U slugs as targets.

When compared to previous fission spectra of the EJ-309 and $LaBr_3$(Ce) detection systems, the HPGe reveals a weakness. All events are shifted towards "high energies." In reality, the events recorded were mostly pile-up that were not rejected and placed in higher energy bins mimicking single high-energy pulses. The shift to higher energies can occur from the fast-shaping filter in the digitizer not being able to separate rapid successive events, a baseline shift due to higher averaging from pile-up, or the pile-up events create higher voltages which saturate the electronics. Because of the high rates, all these reasons likely contribute to such a high shift. Logically, the fission photon spectrum should resemble the shape found in previous Figs. 4.9 and 4.11.

The inability to resolve the fission photon spectrum and cooling requirement make the HPGe detector a weaker candidate for front-end peri-detonation detection. However following the fission period, rates significantly drop allowing the HPGe to resolve delayed photon emission spectra.

### 4.4.4 Rate Conclusions

Considering the rate information in the previous sections, EJ-309 and $LaBr_3$(Ce) detection systems house the capabilities to determine neutron/photon rates and resolve energy information during the fission period. Also, the detectors do not require special cooling requirements for operation. The EJ-309 detection system's energy resolution is inferior to $LaBr_3$(Ce) but has the ability to discriminate neutron/photon events and hosts a faster decay time.

With respect to the HPGe detection system, the cooling requirement coupled with the inability to resolve energy information during the fission period is a clear drawback. HPGe systems offer far superior energy resolution and the inability to leverage this attribute during fission precludes its use during this time period. Rates drop considerably following fission making the HPGe detection system more applicable during the back-end or delayed emission time-period.

Ideally, the EJ-309 detection system is used for determining time-dependent neutron-photon proportional events, neutron rates, photon rates, and aggregate rates. The $LaBr_3$(Ce) detection system is used for determining photon rates and crude (comparatively) fission integrated photon emission energy distribution. Alternatively, the HPGe detection system is used on the back-end peri-detonation or delayed time period to leverage the superior energy resolution providing information on short-lived fission and activation products.

## 4.5 Peri-Detonation Detection Characterization Results

Results are presented in this section using the strongest attributes from the EJ-309, $LaBr_3$(Ce), and HPGe detection systems in order to assign early-time signatures. EJ-309 and $LaBr_3$(Ce) detection systems are used exclusively during the front-end time period while the HPGe and $LaBr_3$(Ce) detection systems are used for back-end or delayed emission characterization. Optimistically, computational SA was run on the back-end time period following fission

to the end of acquisition (0.01 seconds). The SA aggregated the counts in each 47 group photon energy bin structure from end of fission to acquisition conclusion using the previously determined $LaBr_3$(Ce) detector response function. Noteworthy, the same regions of interest (ROI) were examined using the HPGe detection system. To highlight the superior energy resolution, the delayed energy histogram from each target nuclide was examined to visually determine ROI(s) for the delayed time-period.

### 4.5.1 Computational Sensitivity Analysis Results Applied to Experimental Peri-Detonation Detection

Making use of previous sensitivity analysis results, potential ROIs are determined from examining the main effect indices, $S_i$, and the total effect, $S_T$, values. For brevity, the SA results used showed the highest fractional main effect "purity" of sensitivity, meaning the difference between $S_i$ and $S_T$ values (amount of interactions) was minimized. Also, only $^{239}$Pu and $^{238}$U sensitivity indices are shown because of the targets used in the experimental analysis. The top energy ranges were determined by eliminating energy ranges with high computational uncertainty ($>$ 3 MeV), energies lower than 100 keV which natural background and electronic noise affect, and energies around 511 keV which is the energy associated with positron annihilation. Once these energy ranges are eliminated, the purity metric is shown below in Eq. 4.1 and top 10 energy ranges are displayed in Tables 4.3 and 4.4.

$$S^k_{Purity} = \frac{S^k_i}{|S^k_T - S^k_i|} \tag{4.1}$$

where:

$S^k_{Purity}$ is the purity metric for nuclide $k$,

$S^k_i$ is the main effect sensitivity index for nuclide $k$,

$S^k_T$ is the total sensitivity index for nuclide $k$,

$|S^k_T - S^k_i|$ is the interaction amount of nuclide $k$ with other variables.

Table 4.3: $^{239}$Pu sensitivity "purity" calculated from $S_i$ and $S_T$ values.

| Energy Range [MeV] | Purity |
|---|---|
| 3.000E-01 - 2.600E-01 | 0.3943 |
| 3.000E+00 - 2.750E+00 | 0.0912 |
| 1.500E-01 - 1.000E-01 | 0.0702 |
| 2.000E-01 - 1.500E-01 | 0.0583 |
| 1.200E+00 - 1.000E+00 | 0.0508 |
| 7.000E-01 - 6.000E-01 | 0.0203 |
| 2.500E+00 - 2.350E+00 | 0.0202 |
| 2.000E+00 - 1.800E+00 | 0.0192 |
| 2.350E+00 - 2.150E+00 | 0.0185 |
| 2.750E+00 - 2.500E+00 | 0.0170 |

Table 4.4: $^{238}$U sensitivity "purity" calculated from $S_i$ and $S_T$ values.

| Energy Range [MeV] | Purity |
|---|---|
| 2.500E+00 - 2.350E+00 | 28.7353 |
| 2.350E+00 - 2.150E+00 | 19.7467 |
| 9.000E-01 - 8.000E-01 | 9.7064 |
| 3.000E+00 - 2.750E+00 | 6.2667 |
| 2.750E+00 - 2.500E+00 | 5.2323 |
| 1.500E-01 - 1.000E-01 | 4.9412 |
| 2.000E+00 - 1.800E+00 | 4.0564 |
| 3.000E-01 - 2.600E-01 | 3.2312 |
| 1.200E+00 - 1.000E+00 | 3.1166 |
| 4.500E-01 - 4.000E-01 | 2.9806 |

$^{238}$U purity values are noticeably higher than $^{239}$Pu values. The lower purity values associated with $^{239}$Pu stem from high interactions in those photon energy bins. $^{235}$U sensitivities are also considered because of the small amounts present in the $^{Nat}$U slugs.

Table 4.5 shows ratio values for each configuration or mixtures for the $LaBr_3$(Ce) detection system. The top 10 main effect purities of $^{239}$Pu and $^{238}$U displayed in Tables 4.3 and 4.4 aided determination of ratios found in Table 4.5 which show clear sensitivities to the nuclides. Also, the 2.600E-01 - 2.000E-01 MeV energy bin was absent from the $^{239}$Pu and $^{238}$U purity tables but was a high purity for $^{235}$U.

Table 4.5: Selected experimental ratio delayed emission results from SA guided analysis. **Acquired during fission or front-end time period. See Table 4.2 for configuration specifications.

| Energy Range Ratio [MeV] | Config. 1 | Config. 2 | Config. 3 | Config. 4 |
|---|---|---|---|---|
| $\frac{0.2-0.26}{0.1-0.15}$ | 2.02 | 3.52 | 5.16 | 7.66 |
| $\frac{0.26-0.3}{0.1-0.15}$ | 0.64 | 1.55 | 2.70 | 4.54 |
| $\frac{0.26-0.3}{0.2-0.26}$ | 0.32 | 0.44 | 0.52 | 0.59 |
| $\frac{0.26-0.3}{0.2-0.26}$** | 0.58 | 0.74 | 1.36 | 1.60 |
| $\frac{0.4-0.45}{0.2-0.26}$ | 0.75 | 0.59 | 0.56 | 0.51 |
| $\frac{0.8-0.9}{0.6-0.7}$ | 0.80 | 0.61 | 0.47 | 0.52 |
| $\frac{2.35-2.5}{0.26-0.3}$ | 0.0094 | 0.0024 | 0.0020 | -0.00094 |

The selected results displayed in Table 4.5 show clear sensitivities to the fissile/fissionable fuel present during irradiation. The fuel-type sensitivities are indicated by the monotonically increasing/decreasing nature of the selected ratios which contain differing proportions of fissile/fissionable fuel. Energy ranges were from the photon 47-group structure. Negative values indicate the background counts overtook the target photon emissions. Interestingly, the $\frac{0.26-0.3}{0.2-0.26}$ ratio followed the same trend during irradiation or the prompt fission period which indicates fuel-type sensitivities and relationships can be determined during the prompt burnup. Acquisition during the fission time period is possible due to the short decay time of the detector. The EJ-309 detector is also capable of handling higher emission rates but can be leveraged in a different manner.

Because of the composition of the detector, the EJ-309 can be used for discrimination between photon and neutron events. Fissile/fissionable isotopes emit different proportions of neutrons and photons during and after fission. The ratio of photon to neutron events can be used as a rough approximation of the fissile isotope. Figures 4.14 and 4.15 show the

time-dependent photon to neutron proportions.

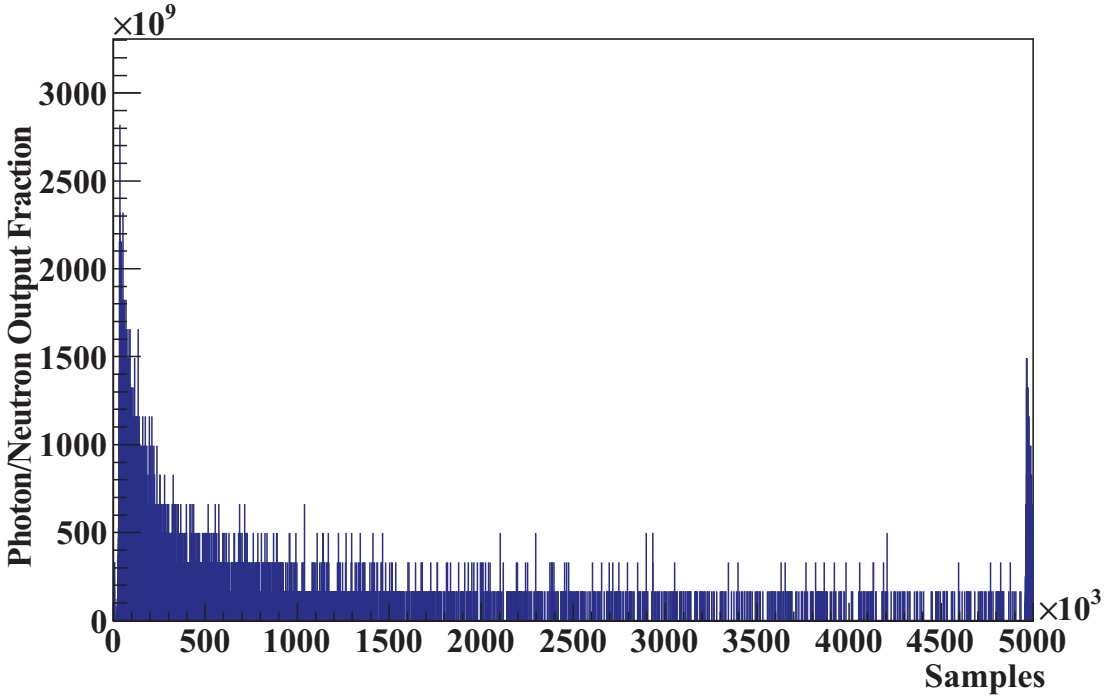


Figure 4.14: Time-dependent photon to neutron ratio associated with $^{239}$Pu acquired from an EJ-309 detector.

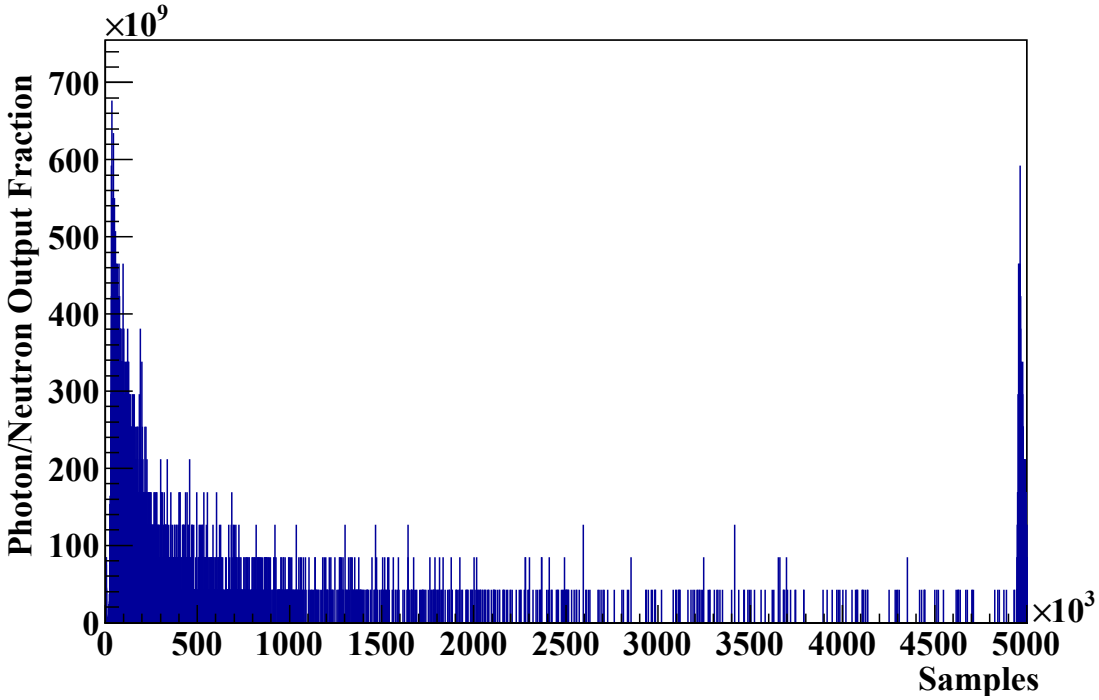


Figure 4.15: Time-dependent photon to neutron ratio associated with $^{Nat}$U acquired from an EJ-309 detector.

There is a considerable difference between $^{239}$Pu and $^{Nat}$U photon to neutron emission proportions. The trend follows the prompt emission proportions from the cited Fat Man and Little Boy devices with Fat Man, $^{239}$Pu, emitting photons an order of magnitude higher [22].

HPGe detection systems have far superior energy resolution but are vulnerable to high emission rates. Delayed emissions during the back-end time period output considerably lower rates compared to the front-end fission period. Taking advantage of the superior energy resolution, ROIs can be determined from examining the integrated delayed emission spectrum. Figure 4.16 shows two ROIs that can be used for the proportion of $^{239}$Pu present during irradiation.

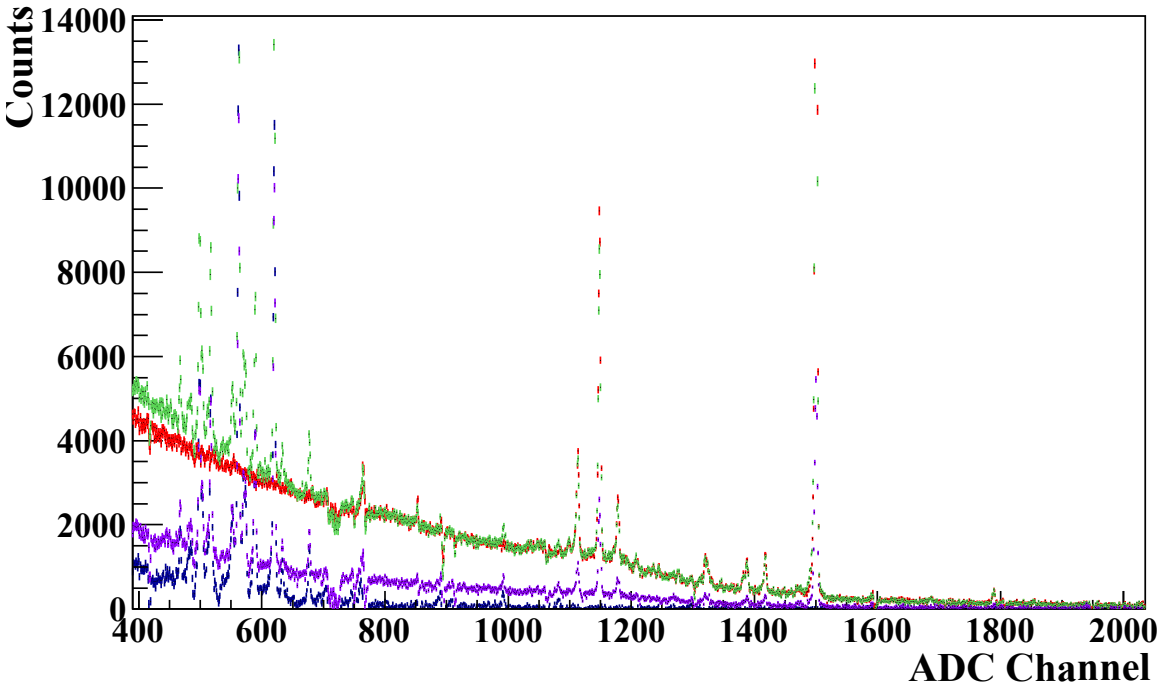


Figure 4.16: Overlaid uncalibrated delayed photon emission spectra for configs. 1-4 used for region of interest determination.

There is a clear sensitivity to the amount $^{239}$Pu present. The channel ROIs are 450-680 and 1100-1520 translating into 0.440-0.676 and 1.106-1.536 MeV energy ranges. The $\frac{0.440-0.676MeV}{1.106-1.536MeV}$ ratio values are: -0.0054, 0.30, 0.46, and 0.64 for configs. 1-4, respectively.

Coupling previous SA results and exploiting detector system strengths provides early-time signatures used for rapid fuel-type determination. The computational SA results provided fuel-type sensitivities, by the purity metric and regression analysis, that were used for ROI determination. The ROIs behaved well with differing $^{239}$Pu and $^{238}$U amounts present during irradiation. Interestingly, the $LaBr_3$(Ce) produced $\frac{0.26-0.3MeV}{0.2-0.26MeV}$ ratio showed clear fuel-type sensitivities during the irradiation period which could give an instantaneous estimation of the dominant fuel-type present. Results from each detection system provide multiple indicators of fuel-type which fortify early-time conclusions.

# CHAPTER 5
# PERI-DETONATION NUCLEAR FORENSIC CONCLUSIONS AND FUTURE WORK

The phenomena surrounding a nuclear detonation present daunting challenges for technical nuclear forensics at early-times. Identifying the factors that affect the emission signatures enables a finer focus on technical analysis and facilitates attribution efforts. The potential consequences and impacts stemming from a detonation necessitates high quality data with known, minimized, uncertainties. Preferably, building a rapid attribution mechanism deters nuclear terrorism, state, and non-state actors from the proliferation and use of nuclear devices.

## 5.1 Sensitivity and Uncertainty Analysis Conclusions

Because the input space of influential factors is vast, identifying the important factors enables model order reduction, places bounds on inferences, and leads to better conclusions. Passively measurable emissions offer promising information which may be used for attribution. Emission profiles change during the peri-detonation period based on dynamic physical phenomena which drives nuclear reactions and processes. Emissions associated with fission, inelastic neutron scatter, and structural activation dominate the burnup or front-end period while fission product decay dominates the back-end or delayed period. Each period holds important information used for rapidly determining key aspects in nuclear device design and the surrounding conditions. The characteristics of the blast may then be used for narrowing down potential source(s).

### 5.1.1 Point-Source Model Conclusions

Point-source model development focused on early-time fission product emissions. The derived sensitivity indices were used for MCF model acceleration and provided the source term in the nuclear cloud rise period. The versatility of SA was mainly demonstrated in the point-source model. Indices were generated with and without $LaBr_3$(Ce) detector responses, for fractionated and unfractionated samples. Also, integrated counts over specified periods were analyzed for the MCF acceleration scheme and nuclear cloud rise period. The sensitivity measures provide a time- and energy-dependent importance guide for analysis focusing research efforts.

The 47-group energy structure was chosen for photon emissions during the front-end and back-end peri-detonation times. This structure appears small considering emissions span wide energy ranges but proved satisfactory and necessary for data generation and subsequent analysis. At the beginning of point-source analysis, the photon rate ($\frac{photons}{second}$) in each of the energy bins, with and without detector response functions, were examined.

As suspected, the rates in all the energy bins were mostly affected by the neutron flux in the device which is shown in Fig. 5.1. The flux variable affected all the energy bins over the entirety of the analysis time which is demonstrated by the small $2\sigma$ range.

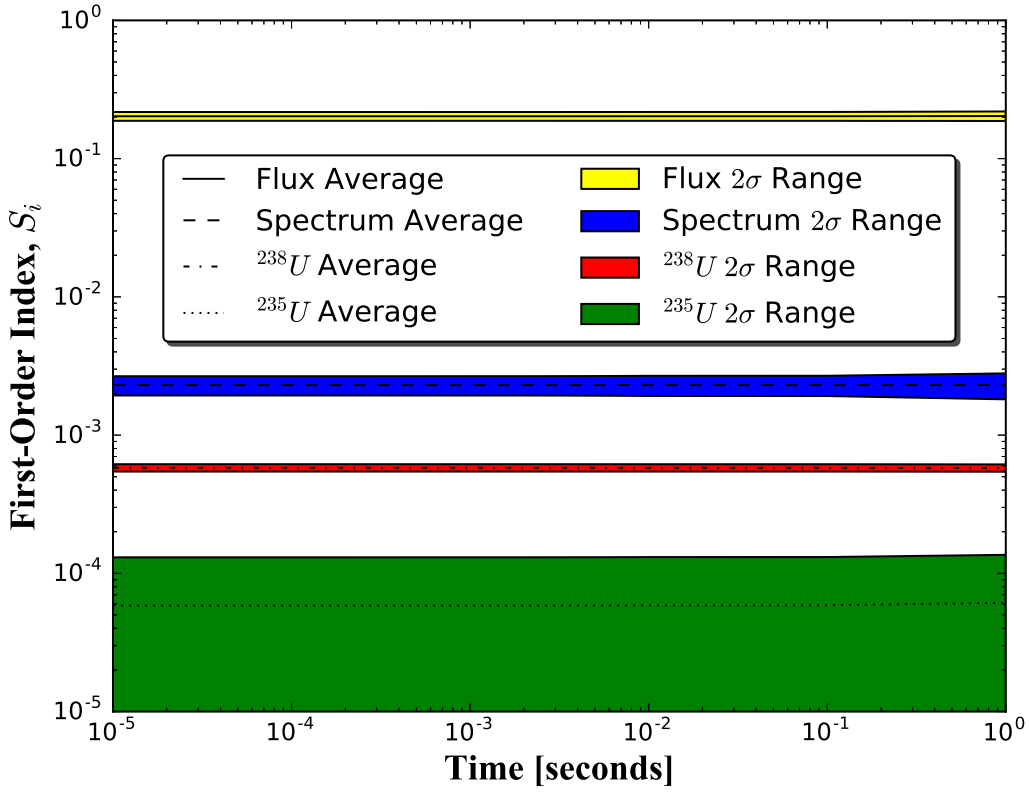


Figure 5.1: Unfractionated $S_i$ values averaged over photon energy bins for flux, spectrum, $^{238}$U, and $^{235}$U with flux variable being the highest contributor to photon production.

While the flux was the dominant effect, the relationship was not linear and included interactions between other variables. Nonlinearities and interactions are shown in the magnitude of the $S_i$ value in Fig. 5.1 with a value of 1 being a perfect linear relationship and 0 indicating no linear relationship. To provide perspective to this observation, Fig. 5.2 below shows the energy group 27 (1.00-1.20 MeV) fitting function for determining the nuclear device flux at 1 second after detonation.

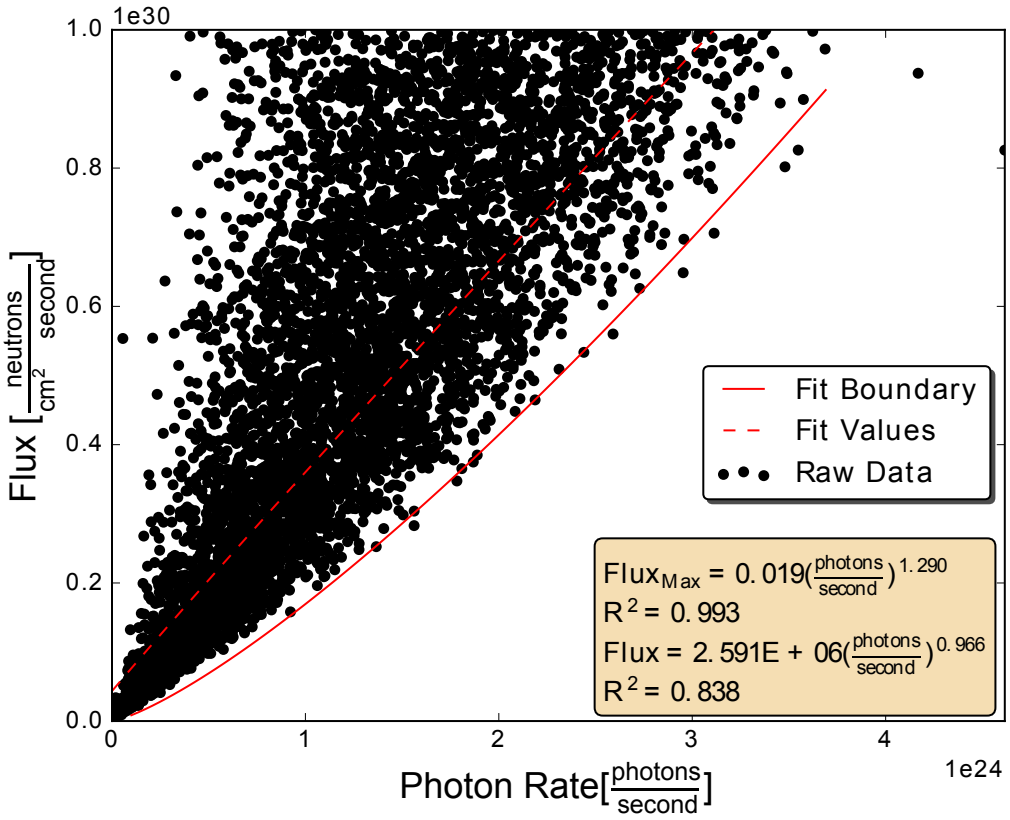


Figure 5.2: Unfractionated flux association with 1.0-1.2 MeV photon energy bin rate at 1.0 second after detonation.

The low $S_i$ value of the flux is explained by the nonlinear fitting function derived in Fig. 5.2. Also, the obvious spread of the data towards higher photon rates explains the low $S_i$ value. Because the flux has a higher (relative) importance in each energy bin, the yield of the device has a near linear relationship with rate in the detector as shown in Fig. 5.3.

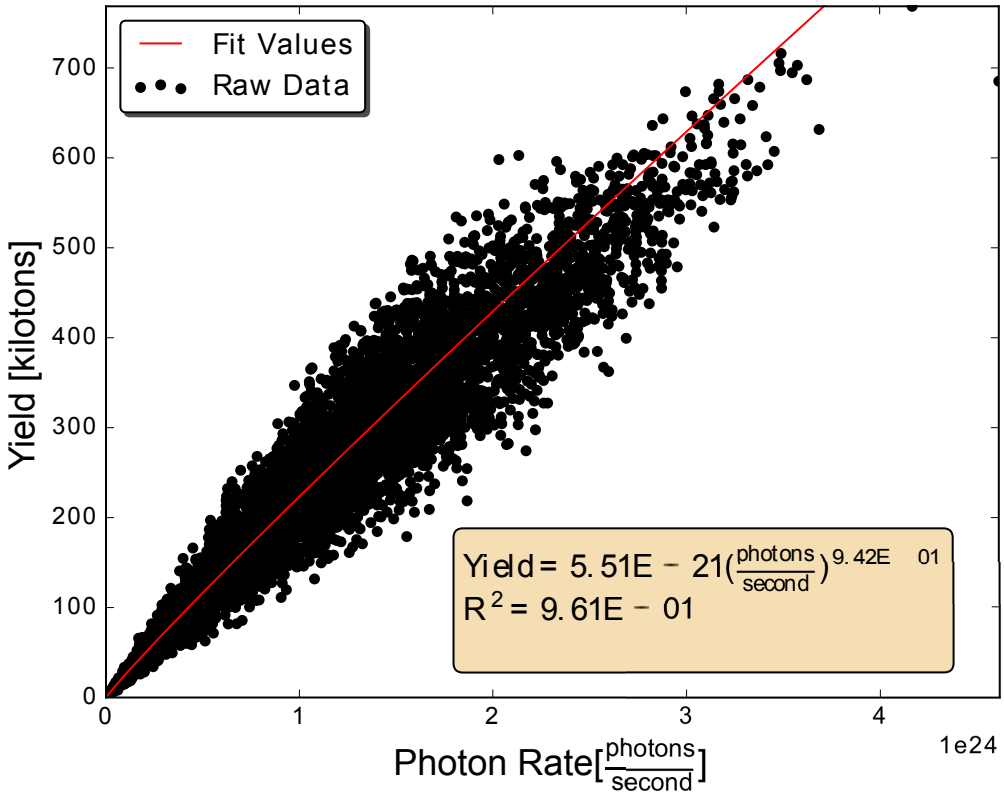


Figure 5.3: Unfractionated yield association with 1.0-1.2 MeV photon energy bin rate at 1.0 second after detonation.

Notably, the flux also affected the fractionated sample similarly; although, fuel-type sensitivities increased at late times. The increase in importance for the various fuel-types is thought to be associated with the small emission rate at late times. Higher fuel-type importances were also in the higher energy bins which contained the highest amount of error. Low emission rates coupled with the uncertainty in the energy bin precludes stating higher importance for the different fuel-types.

A more realistic representation of importance factors is revealed once the detector response is applied. Conversely, with the previous results using raw photon rates, fuel-type sensitivities/importances began to surface by integrating the counts following the front-end period. Each of the fuel-types examined, flux, and spectrum values show stronger linear correlations. Moreover, variables interact unpredictably across each energy bin emphasizing the need for comparing $S_i$ and $S_T$ values associated with each variable. Further

examination of the $S_i$ and $S_T$ values reveals candidate energy ranges used in ratios for fuel type determination which is later applied to accelerate the MCF algorithm and experimental portion of this research.

*Monte Carlo Filtering Acceleration Conclusions*

Results from the point-source SA and local sensitivity methods guided determination of the MCF acceleration scheme. To avoid hydrodynamic calculations associated with fireball expansion, ratios were integrated between the conclusion of fission and 0.1 seconds using the calculated detector response function. $S_i$ and $S_T$ values were used to calculate a fractional main-effect purity metric which is shown below in Eq. 5.1. The purity metric and regression analysis results were used in conjunction to determine the best ratios to identify present fuel-type(s).

$$S^k_{Purity} = \frac{S^k_i}{|S^k_T - S^k_i|} \tag{5.1}$$

where:

$S^k_{Purity}$ is the purity metric for nuclide $k$,

$S^k_i$ is the main effect sensitivity index for nuclide $k$,

$S^k_T$ is the total sensitivity index for nuclide $k$,

$|S^k_T - S^k_i|$ is the interaction amount of nuclide $k$ with other variables.

Because of the flux uncertainty and sampling technique, the found relationships contained upper and lower bounds. An example of this is shown in Fig. 5.4 with the group 15 (2.75-3.00 MeV) to 22 (1.57-1.66 MeV) ratio applied to $^{239}$Pu fractional mass present during irradiation. Because ORIGEN performs a point-source irradiation, the fractional mass value can be roughly compared to the fractional fissions from each examined fuel-type.

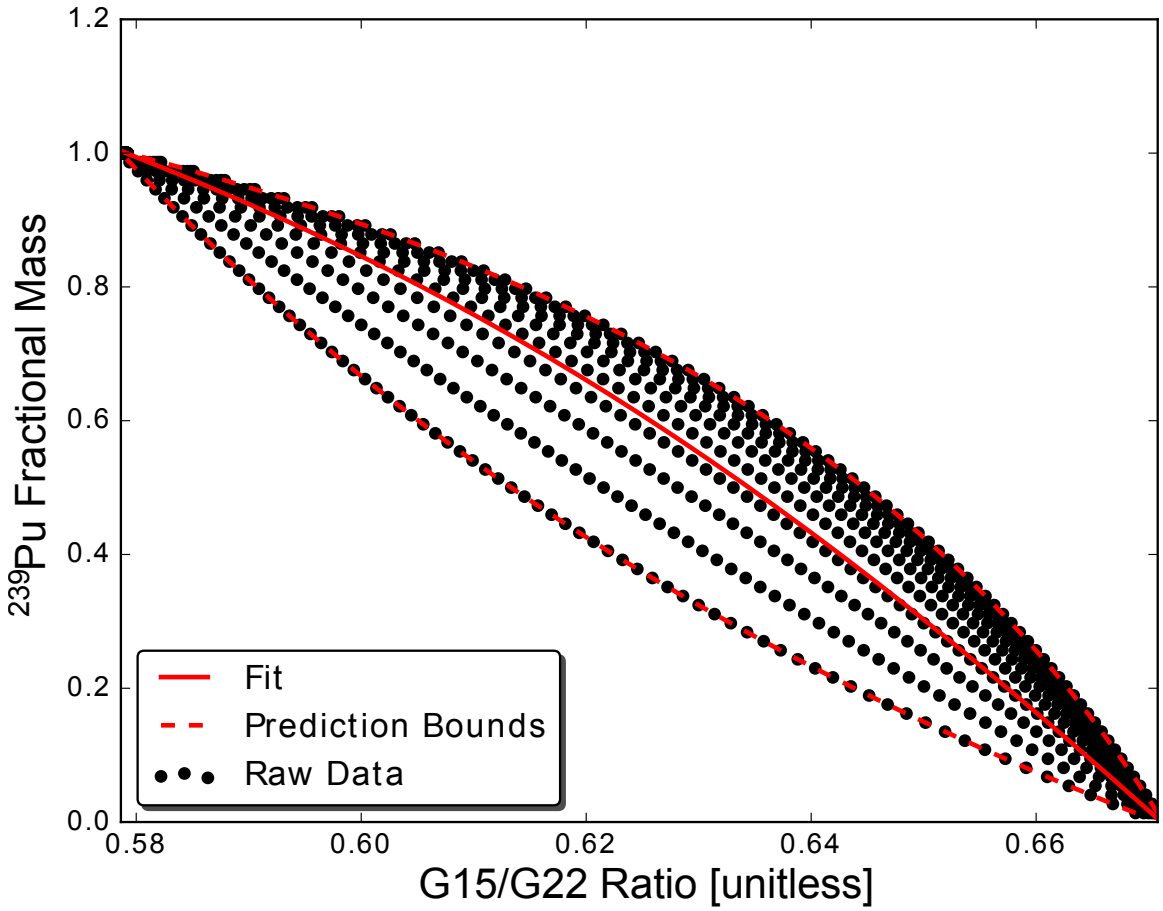


Figure 5.4: $^{239}$Pu fractional mass from the $\frac{E_{grp}15}{E_{grp}22}$ ratio with associated prediction bounds.

The shape of the values in Fig. 5.4 is due to the stratified sampling technique. Stratified sampling was applied to ensure the coverage of all possible fuel, reflector, and flux combinations. For comparison, random sampling was applied in Fig. 5.3 which can produce nonphysical configurations. Stratified sampling increases convergence of $S_i$ and $S_T$ values faster than random sampling [17]. Also, the shape of the data in Fig. 5.4 shows the effect of the flux on the ratio which was a result of the sampling technique. The sampling method fortuitously demonstrates the effect of an unknown device flux on the ratio value. If the flux was known, the prediction bounds would shrink making the results more accurate. Realistically and because of the time constraint, flux values are unknown and force the fitted answer to fall between the upper and lower bound. Regardless, all ratios allowed for acceleration of the MCF algorithm and dramatically reduced the input space.

Table 5.1: MCF acceleration fractional mass results for Fat Man (FM) and Little Boy (LB) reference cases.

| Nuclide - Reference Case [Ratio] | Lower Limit | Average | Upper Limit |
|---|---|---|---|
| $^{233}$U - FM [G29/G31] | -0.0744 | -0.0536 | -0.0257 |
| $^{233}$U - LB [G29/G31] | -0.2946 | -0.1747 | -0.07246 |
| $^{235}$U - FM [G20/G21] | 0.0307 | 0.0475 | 0.0657 |
| $^{235}$U - LB [G20/G21] | 0.6141 | 0.7736 | 0.8372 |
| $^{238}$U - FM [G17/G19] | -0.0173 | -0.0138 | 0.1065 |
| $^{238}$U - LB [G17/G19] | 0.0257 | 0.0577 | 0.1887 |
| $^{239}$Pu - FM [G15/G22] | -0.0744 | -0.0536 | -0.0257 |
| $^{239}$Pu - LB [G15/G22] | -0.0496 | -0.0324 | -0.0149 |

Notably, MCF acceleration relationships were not considered for the other reflector types - Tungsten, Lead, and Iridium. The local sensitivity methods produced unusable ratio values which mimicked Dirac delta functions (undefined slope) at a given ratio amount or simply a vertical line when fractional mass versus ratio amount was plotted. These reflectors were quickly eliminated based on a lack of matched configurations in an abbreviated MCF run with looser scoring requirements and less samples.

The MCF results presented in Table 5.1 drastically reduced the inputs into the main MCF algorithm. These results further illustrate the effect of an unknown flux on the predictive relationships. For example, $^{235}$U is a small component (0.72 atom $\%$) in $^{Nat}$U but the MCF acceleration results show a fractional mass value between 0.0307 and 0.0657. The fractional mass result for $^{235}$U apropos to the Fat Man design derivative indicates the possible existence of $^{235}$U in the device or a possible input into the MCF algorithm.

### 5.1.2 Monte Carlo Filtering and Nuclear Cloud Rise Conclusions

The developed MCF algorithm performed adequately with associated nuclear data uncertainties. The prior derived acceleration results also performed adequately in shrinking the input space and drastically reduced run times. Without the acceleration scheme, run times were unreasonable and a large number of samples did not guarantee coverage of the entire input space which increased the uncertainties associated with mass, density, and height-of-burst.

After optimization of the MCF algorithm, a low number of stratified samples was run on the narrowed input space. In the case of the Fat Man derivative design, no configurations of $^{239}$Pu with an HEU reflected or bare assembly were matched. The acceleration results indicated the presence of $^{235}$U and $^{238}$U leaving the $^{Nat}$U reflector. The problem was repeated again using the same amount of samples but using tighter mass and density ranges with a $^{Nat}$U reflector, pure $^{239}$Pu, WGPu, Aged WGPu, and FGPu. The matched results indicated pure $^{239}$Pu, WGPu, or FGPu fuel-types with a $^{Nat}$U reflector. Results are summarized in Table 5.2.

Table 5.2: Monte Carlo Filtering algorithm results for Fat Man configuration. Weighted and non-weighted estimates of fuel and reflector mass, yield, height-of-burst, and density.

| | $^{239}$Pu/$^{Nat}$U | $^{239}$Pu/$^{Nat}$U (HOB Weighted) |
|---|---|---|
| Fuel Mass [kg] | 6.84 $\pm$ 1.17 | 6.84 $\pm$ 1.18 |
| Reflector Mass [kg] | 112.66 $\pm$ 24.23 | 112.68 $\pm$ 24.23 |
| Yield [kt] | 15.37 $\pm$ 0.93 | 15.37 $\pm$ 0.93 |
| HOB [cm] | 10226.72 $\pm$ 206.92 | 10226.57 $\pm$ 207.06 |
| Density [$\frac{g}{cm^3}$] | 31.60 $\pm$ 3.59 | 31.60 $\pm$ 3.59 |

The results of the Fat Man derivative are accurate and matched the reference spectrum well. Averaged and HOB weighted results are nearly identical because of the stringent scoring system which accounts for rate, integral counts, and shape of the spectrum. The precision

of the values is attributed to the rate score which was resolvable with the prescribed time steps (10 steps from 0 to 1.0E-06 seconds). The resolution of the rate at early-times was due to the large $^{Nat}$U reflector that impeded early-time photon emission signal which did not saturate the detector. The signatures emanating from nuclear cloud rise allowed for the HOB to be determined accurately which can be used as a secondary signature if prompt data is not available. The nuclear cloud rise takes place at extended times (comparatively) and the photon rates can easily be resolved. Interestingly, the MCF algorithm matched 100% $^{239}$Pu to FGPu (86.1% by mass $^{239}$Pu) to the reference Fat Man derivative spectrum which contained 100% $^{239}$Pu. The FGPu matched cases contained higher mass and density estimates which is indicative of higher amounts of $^{240}$Pu (12%) creating lower device yields. Simply, the higher mass and density values made up for the higher $^{240}$Pu amounts which created the same photon rate in the detector volume. While $^{240}$Pu created higher mass and density estimates, the spectrum shape between FGPu and pure $^{239}$Pu were close in proximity creating similar behavior. Because the $^{Nat}$U reflector mass was constant, the higher FGPu mass and density values allowed the leakage spectrum to mimic the reference Fat Man derivative which shows the emissions are highly dependent on the reflector configuration/reactions.

At first glance, the Little Boy derivative design results were less accurate containing high error. The error can be explained by the nature of the design. The Little Boy derivative was modeled as a bare assembly allowing for the leakage spectrum to be unimpeded. Higher leakage emissions cause earlier detector saturation which poses as a detector that is incapable of resolving high emission rates (e.g. HPGe). In reality, the quick "saturation" results from the low number of modeled time steps. Although yield and HOB results were high in error, the calculated fuel mass contained less error and fell close to the actual value confirming leakage and detector signal is highly dependent on mass. Results are shown in Tables 5.3 and 5.4.

Table 5.3: Monte Carlo Filtering algorithm results for Little Boy configuration. Weighted and non-weighted estimates of fuel and reflector mass, yield, and height-of-burst.

| | $^{235}$U/Air | $^{235}$U/Air (HOB Weighted) |
|---|---|---|
| Fuel Mass [kg] | 45.07 $\pm$ 4.72 | 44.87 $\pm$ 5.18 |
| Reflector Mass [kg] | N/A | N/A |
| Yield [kt] | 104.86 $\pm$ 114.52 | 109.82 $\pm$ 118.42 |
| HOB [cm] | 18139.58 $\pm$ 5359.15 | 18258.86 $\pm$ 5843.24 |

Table 5.4: Monte Carlo Filtering algorithm results for Little Boy configuration following secondary cloud rise module scoring requirement. Weighted and non-weighted estimates of fuel and reflector mass, yield, and height-of-burst.

| | $^{235}$U/Air | $^{235}$U/Air (HOB Weighted) |
|---|---|---|
| Fuel Mass [kg] | 39.07 $\pm$ 1.51 | 39.08 $\pm$ 1.52 |
| Reflector Mass [kg] | N/A | N/A |
| Yield [kt] | 11.71 $\pm$ 1.68 | 11.79 $\pm$ 1.66 |
| HOB [cm] | 12429.16 $\pm$ 612.46 | 12457.34 $\pm$ 602.18 |

Because the front-end fission period uses the same scoring system as the back-end nuclear cloud rise period, results can be further filtered by "passing" values associated with the nuclear cloud rise signatures. Using the nuclear cloud rise signatures produces more accurate results across all variables. The effect of the secondary filter on the results emphasizes the detector signal is highly dependent on neutron activation, attenuation, and fission product emissions during nuclear cloud rise. Luckily, high dependency demonstrates the ability to use nuclear cloud rise signatures to deduce design and condition characteristics in the absence of prompt front-end fission data.

Because the MCF algorithm gives mass and energy output estimates, a hypothetical device fission efficiency estimate can be calculated which is highly useful for sophistication

determination. The Fat Man and Little Boy design derivatives produced device fission efficiency estimates of 12.81 $\pm$ 2.32% and 1.71 $\pm$ 0.19%, respectively. Rapid sophistication indicators provide useful information about potential sources or intent. Efficiency coupled with HOB estimates may provide nuclear forensic relevant information.

### 5.1.3 Peri-Detonation Uncertainty Conclusions

With any computational model, the associated data and assumptions inject uncertainties into the results. In this case, passively measurable signatures contain uncertainty stemming from cross-sections, fission product yields, and decay data. The developed model propagates the nuclear data uncertainty from the prompt front-end period through the back-end decay period. Ultimately, these uncertainties dictate which energies can be used for analysis based on limiting the uncertainty.

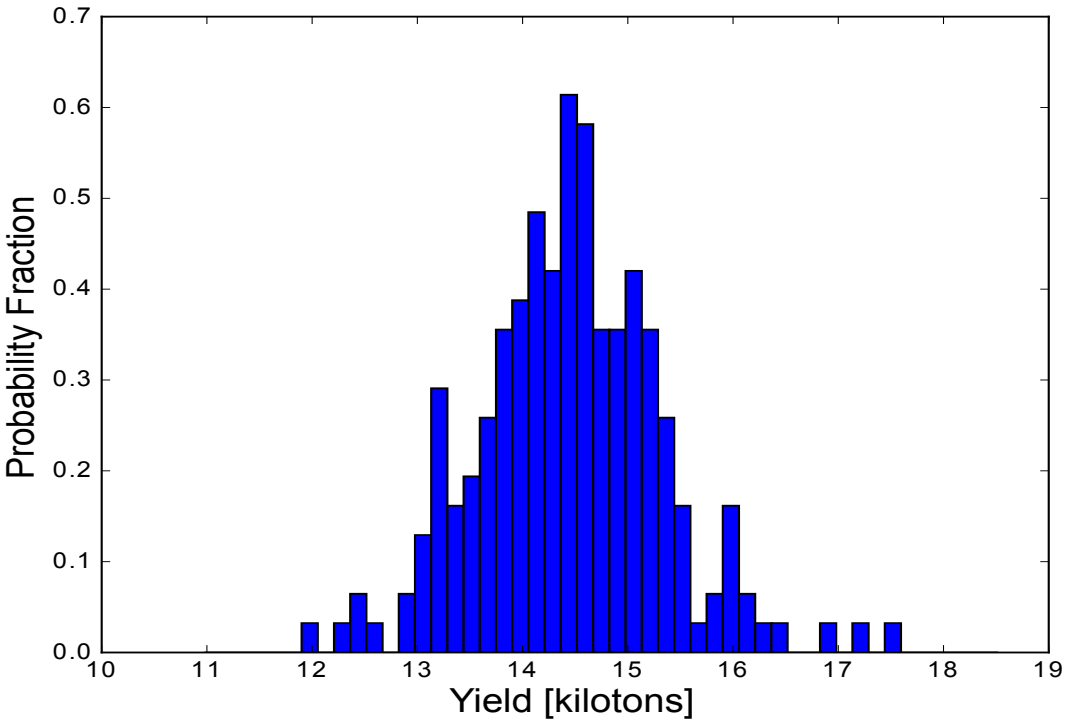


Figure 5.5: Nuclear device yield distribution from cross-section uncertainties.

Figure 5.5 shows the effect of cross-section uncertainty on total energy output. The device yield standard error resulting from the cross-section was calculated as 7.6%. These

errors propagate into fission product emissions due to the dependence on neutron spectrum shape and magnitude. The decay emissions were then used to generate the signatures emanating from early-time nuclear cloud rise.

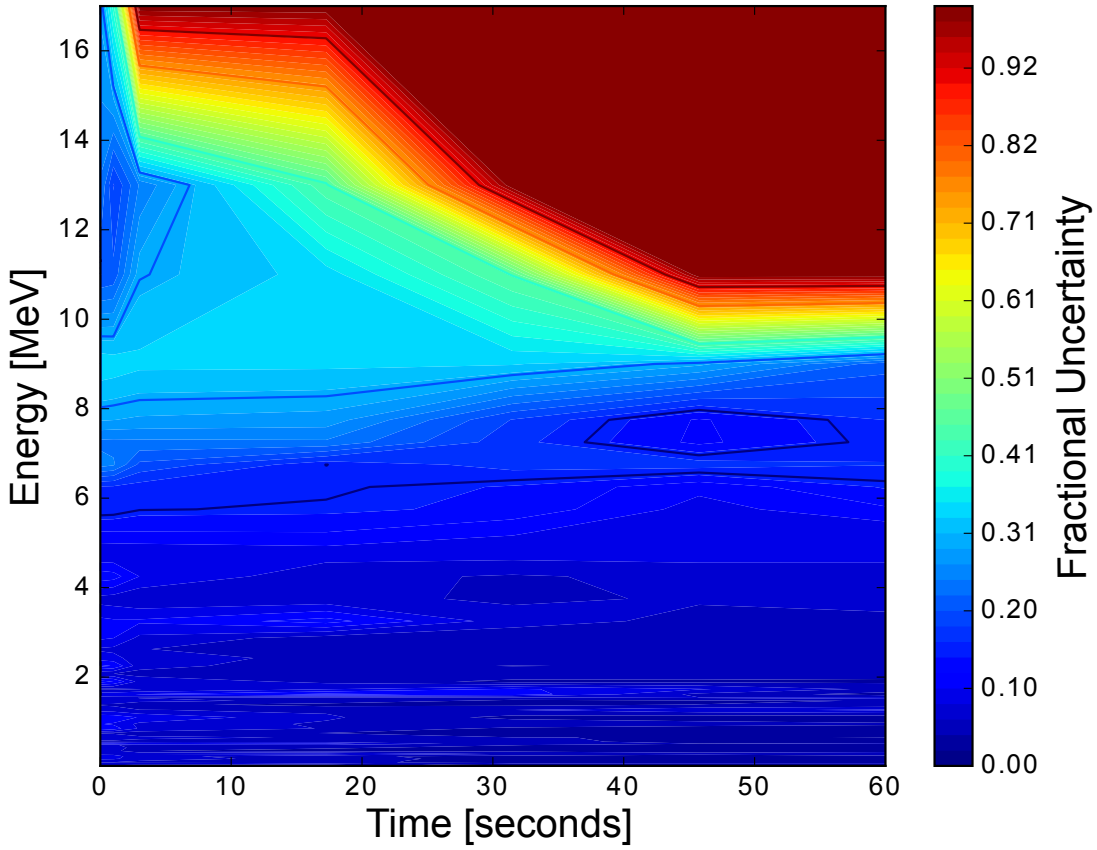


Figure 5.6: Fat Man design derivative photon emission absolute uncertainty between 0.0 and 60.0 seconds.

The propagated uncertainty fundamentally determines quality of conclusions and time of analysis. Figure 5.6 shows the compounded photon emission error originating from the prompt front-end period and extending through the decay back-end period. The decay period error results from cross-section, decay, and fission product yields. Energies over 10 MeV at late times contain high amounts of error which lead to erroneous predictions and conclusions. During the prompt period, errors are lower and produce more accurate predictions and conclusions. Another limiting factor of detectability is the effective distance of the photon emissions which also injects error.

### 5.1.4 Peri-Detonation Effective Detectability Distance Conclusions

An effective detectability distance study was completed to provide a maximum distance for detectability considering nuclear data and counting error within the detector. The uncertainties from nuclear data coupled with counting error showed clear limitations in detectability. The counting error was calculated by integrating the count rate within the detector over 60 seconds at distances between 400 and 8050 meters (approximately 0.25-5.0 miles). Noteworthy, the previous MCF matching algorithm was held static at 400 meters. This short distance from a nuclear explosion would destroy any detection system well before the 60 second mark further necessitating a distance study. Interestingly, the Little Boy design derivative "saturated" the detector at 400 meters. The saturation was due to the large time steps used for the prompt period mimicking a saturated detector or a less advanced detection system. Detector saturation produced high errors in the matching algorithm but fortuitously proved the use of signatures emanating from nuclear cloud rise for gaining device characteristics. The distance study provided perspective on optimum detector placement and showed that increasing the distance from detonation lessened detector saturation with the Little Boy design derivative. Distance error results place a minimum distance limit of detector placement as proximity saturates and destroys the detection system while long distances produce high errors from dwindling counting statistics.

The Fat Man design derivative standard error reached $100\%$ for all energy bins except the 0.01-0.02 MeV energy range at 3300 meters. Unfortunately, this energy range is easily attenuated/shielded and obfuscated by natural background radiation and electronic noise. Figures 5.7 and 5.8 show heat maps of the standard error over distance and energy.

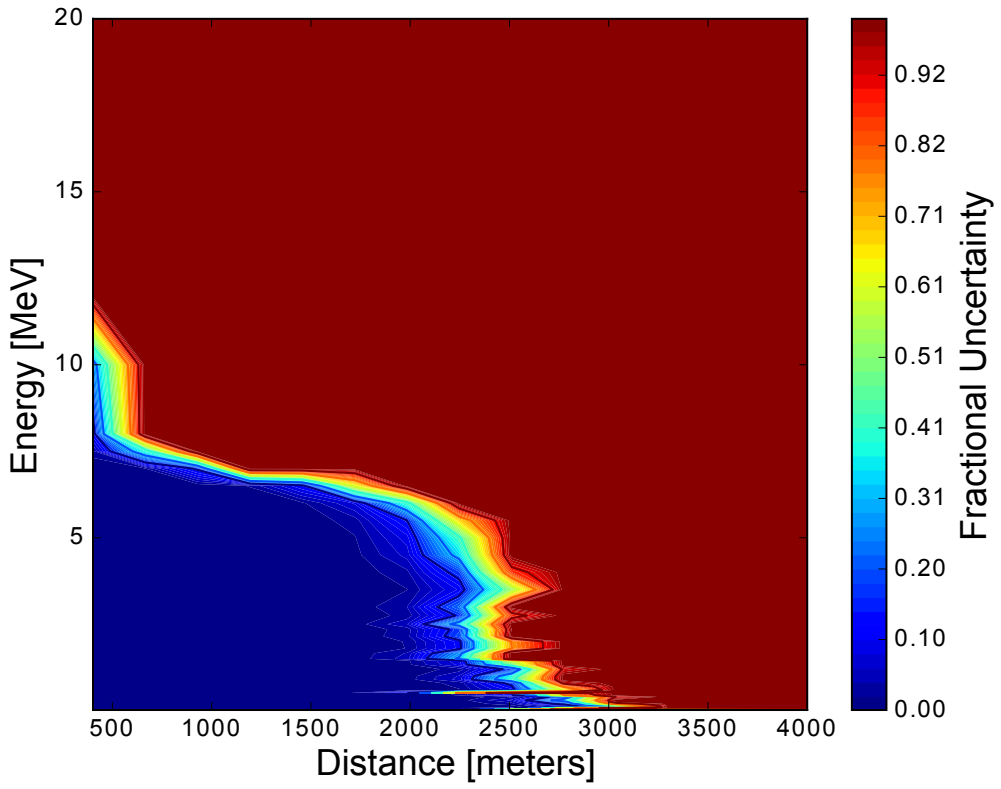


Figure 5.7: Fat Man design derivative fractional uncertainty of energy bins resulting from distance away from nuclear detonation.

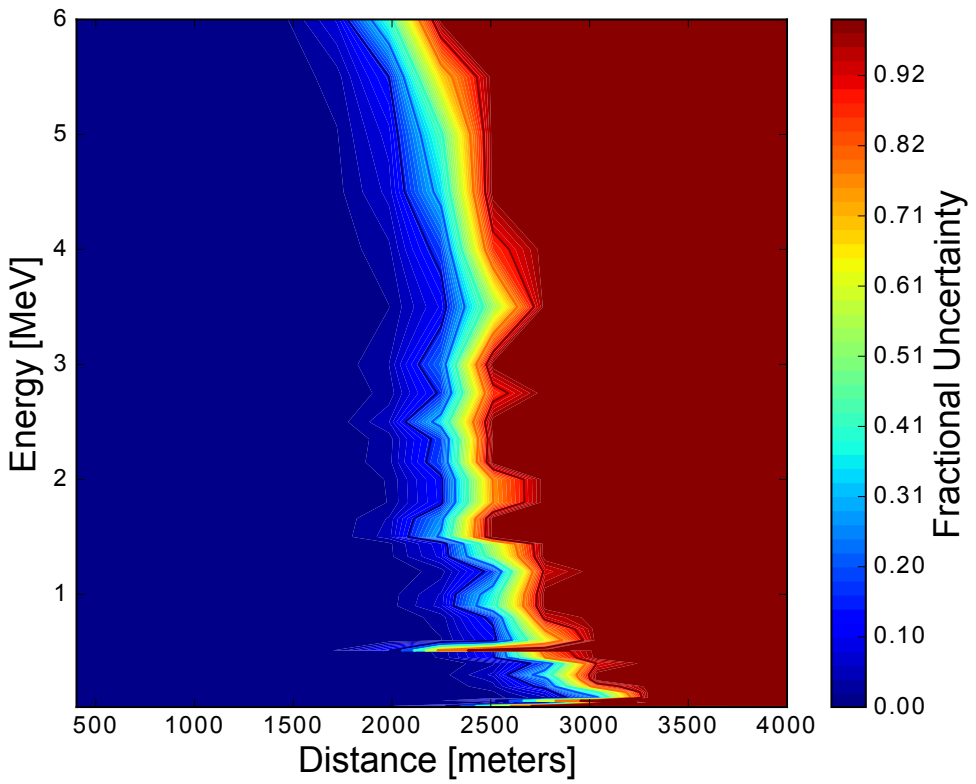


Figure 5.8: Zoomed Fat Man design derivative fractional uncertainty of energy bins resulting from distance away from nuclear detonation.

Clearly, 3300 meters is an absolute cut-off point of passive photon detectability for the Fat Man design derivative. If the ratios for determining the fractional mass and presence of an isotope are used for optimization, the greatest distances of detectability for a Fat Man design derivative is 2200, 1900, and 1700 meters for errors less than 50, 25, and 5%, respectively. If the higher energy range (2.35-2.5 MeV) is removed, the distances extend to 2500 (50%), 2200(25%), and 1900(5%) meters. From a global perspective, 1.0-6.0 MeV energy range effective distances are 1900(50%), 1700(25%), and 1400(5%) meters while under 1.0 MeV gives distances of 1900(50%), 1900(25%), and 1700(5%) meters.

The Fat Man design derivative effective detectability distance study indicated 1700 meters would minimize error in counting for the 0.01-6.0 MeV energy range. Over 6 MeV, the

error is high, drastically reducing the distance required for error minimization and likely destroying the detection system before any information can be relayed.

Little Boy design derivative error differed from the Fat Man design derivative. Although, at first glance of Figure 5.9 shows little difference between the Fat Man and Little Boy design derivatives integral detection uncertainty. Figure 5.10 is more telling and shows the fractional difference between the two designs which is higher in certain energy ranges. The error behavior is due to the differing photon outputs between fissile isotopes and the geometry which affects photon leakage.

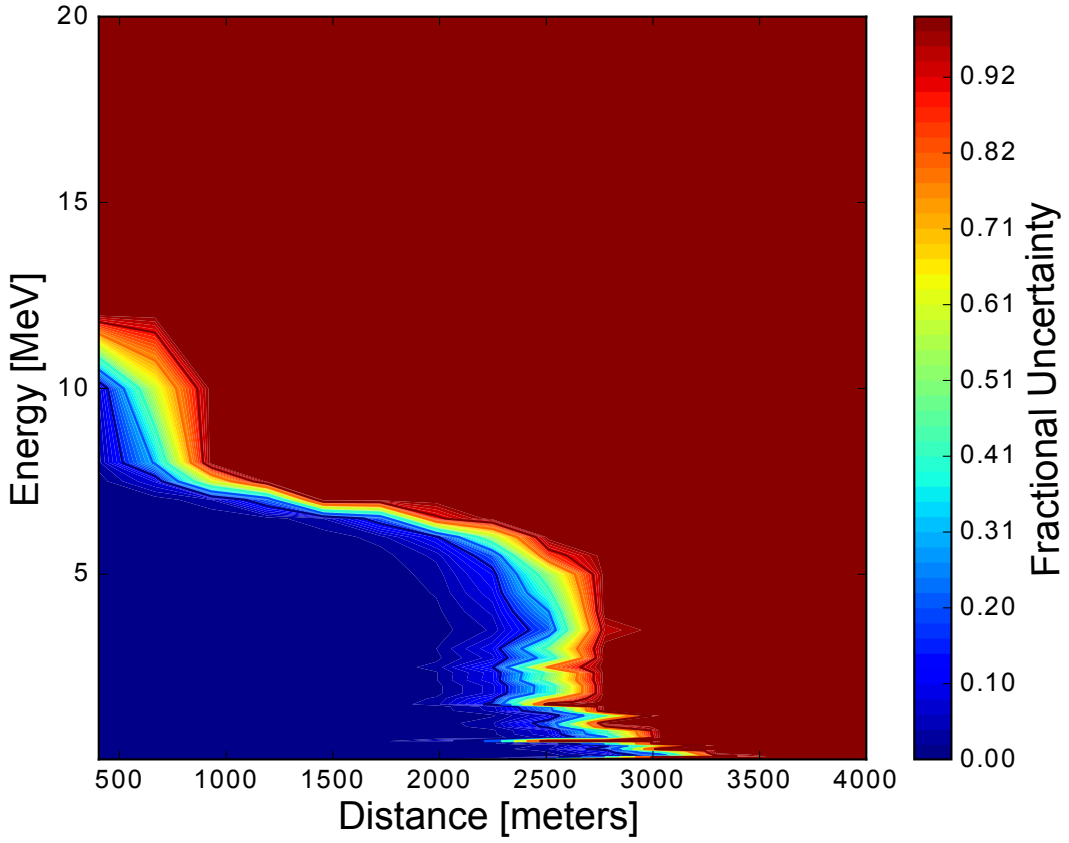


Figure 5.9: Little Boy design derivative heat map of detection uncertainty associated with distance from ground zero.

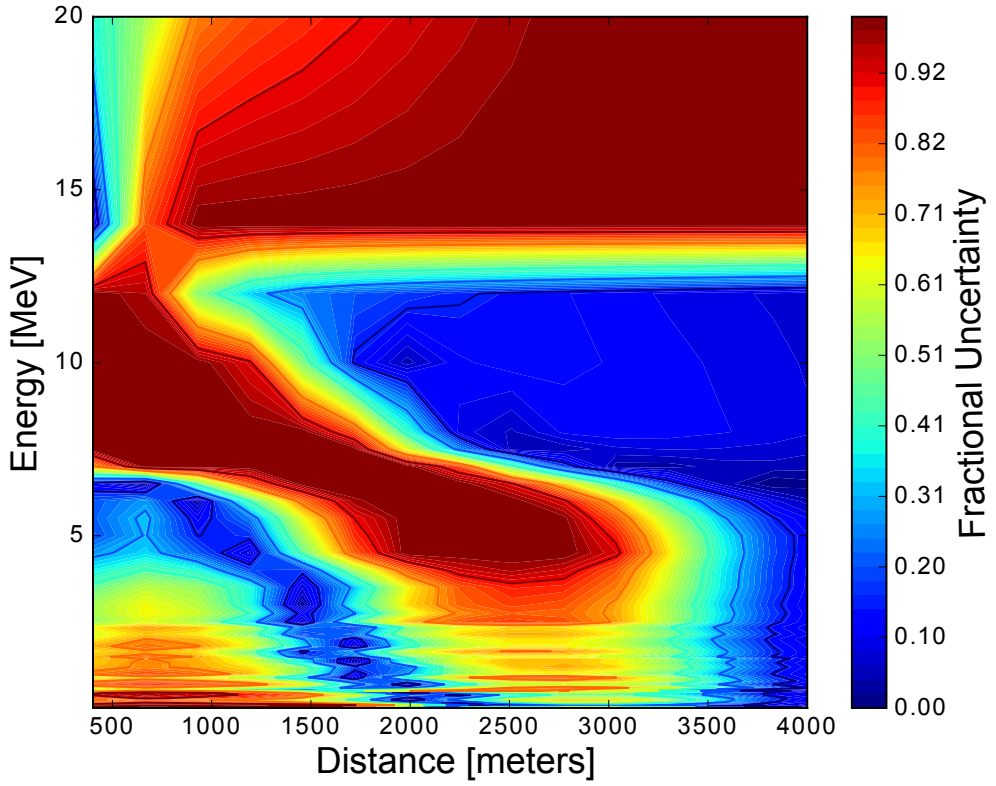


Figure 5.10: Uncertainty fractional difference between Fat Man and Little Boy design derivatives heat map associated with distance from ground zero.

There is a clear band of high uncertainty between the two designs starting between 7 and 12 MeV at close distances which is an exclusion zone for detector placement. The lower uncertainty band between the two designs beginning at approximately 4 and 6 MeV at close distances extends to approximately 2000 meters. Nuclear device design is unknown before detector placement. Uncertainty between the two designs must be minimized because the design type is unknown before detector placement. Simply, each design is a possibility and must be considered. For energies lower than 6 MeV, 1700 meters would minimize both error in counting and error between the two designs.

## 5.2 Experimental Conclusions

Experimentally, the front-end fission period through the back-end delayed period encompassed 0.01 seconds including irradiation of the source and a delayed emission period. Five

different target "configurations" were irradiated with the DT source. Descriptions of the configurations are found in Table 5.5. The low amount (0.5 grams) of $^{237}$Np and the lack of sensitivity indices precluded further analysis of early-time signatures from $^{237}$Np.

Table 5.5: Irradiated fissile/fissionable configurations.

| | $^{239}$Pu [grams] | $^{Nat}$U [grams] | $^{237}$Np [grams] |
|---|---|---|---|
| Config. 1 | 5.0 | 0.0 | 0.0 |
| Config. 2 | 5.0 | 3844.6 | 0.0 |
| Config. 3 | 5.0 | 17300.8 | 0.0 |
| Config. 4 | 0.0 | 17300.8 | 0.0 |
| Config. 5 | 0.0 | 0.0 | 0.5 |

Logically, the emission rates during a nuclear detonation are high, placing limitations on detection method and equipment employed. The rate limitations of the HPGe precluded its use in the front-end fission period as shown in Fig. 5.11. The integrated counts over the 10 microsecond wide pulse are pushed towards "high energies" while in reality the detector is accepting pulse pile-up resembling a single high energy photon pulse. Imitation higher energy pulses can occur for a number of reasons and are likely compounded. The shift to higher energies can occur from the fast-shaping filter in the digitizer not being able to separate rapid successive events, a baseline shift due to higher averaging from pile-up, or the pile-up events create higher voltages which can saturate the electronics.

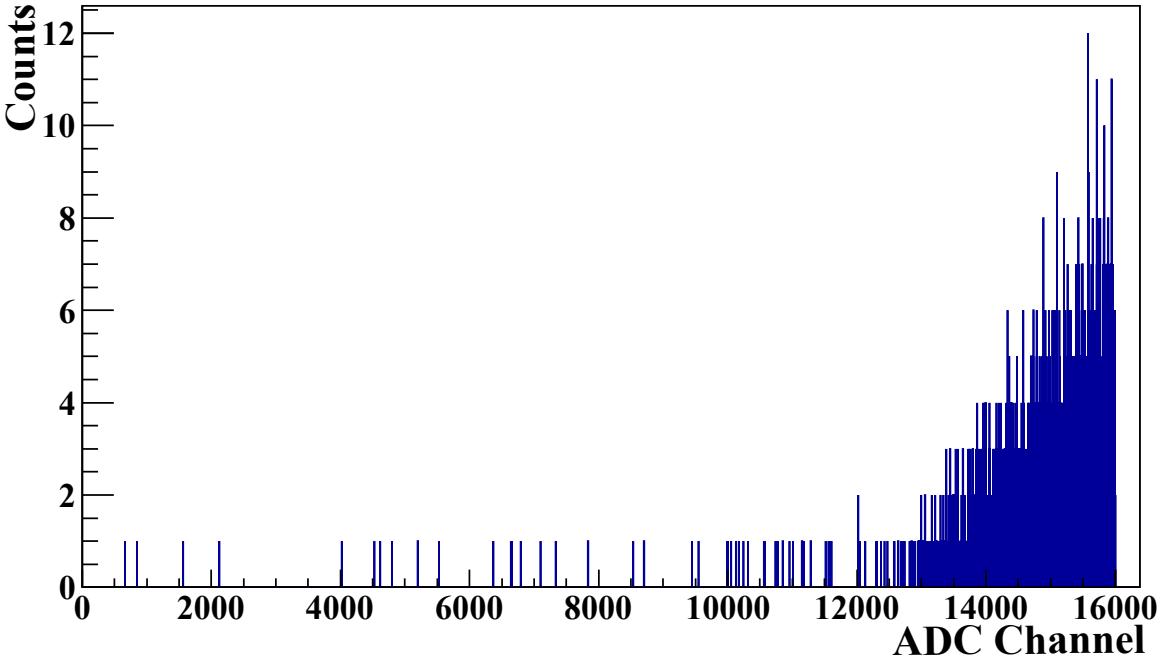


Figure 5.11: Fission uncalibrated energy histogram shown in ADC channel using a HPGe detector with $^{Nat}$U slugs as targets.

EJ-309 and $LaBr_3$(Ce) detectors can manage high emission rates as shown in Fig. 5.12. The energy histogram can be resolved during high emission rate fission period. PSD can be performed with the $LaBr_3$(Ce) and EJ-309 detection systems segregating neutron, photon, and pile-up events. This feature allows for neutron, photon, and total rates to be determined along with confidently counting desired particles (i.e. neutron vs. photon events).

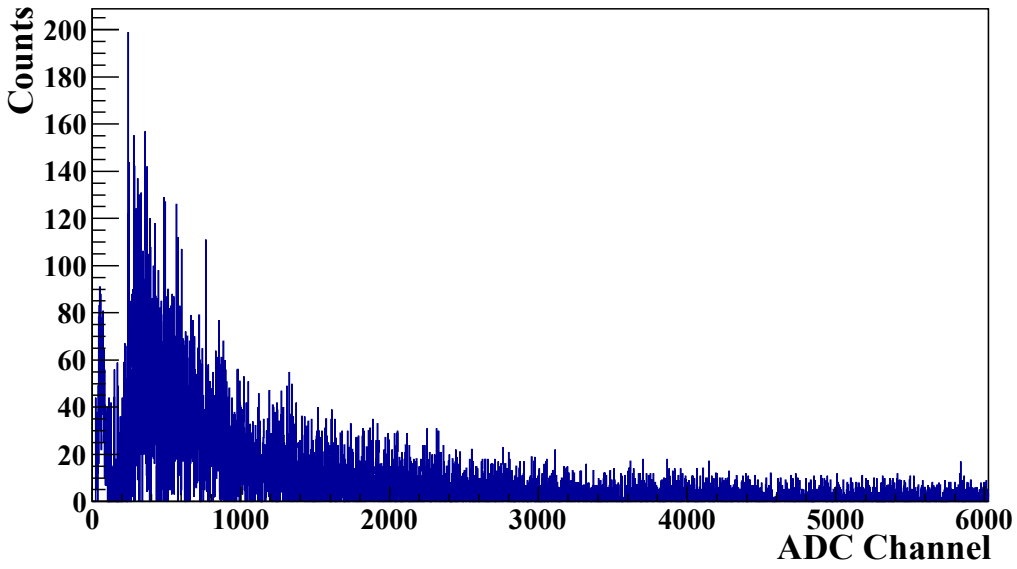


Figure 5.12: Fission uncalibrated energy histogram shown in ADC channel using an $LaBr_3$(Ce) detector with $^{Nat}$U slugs as targets.

The SA used in the computational section provided global and local sensitivity metrics for experimental analysis. Specifically, the SA produced purity metric aided determination of the ROIs used for experimental analysis. The interval of SA analysis was at the conclusion of irradiation to 0.01 seconds matching the period of analysis in the experimental portion. The integral counts between this interval were used in both experimental and computational portions.

Only $^{239}$Pu and $^{238}$U calculated purity metrics are shown because they were the exclusive targets used in the experimental analysis. Top energy ranges were determined by eliminating energy ranges with high computational uncertainty ($>$ 3 MeV), energies lower than 100 keV which are obfuscated by natural background and electronic noise, and energies around 511 keV which is the energy associated with positron annihilation. Once these energy ranges are eliminated, the purity metric is shown below in Eq. 5.2 and top 10 energy ranges are displayed in Tables 5.6 and 5.7.

$$S^k_{Purity} = \frac{S^k_i}{|S^k_T - S^k_i|} \tag{5.2}$$

where:

$S^k_{Purity}$ is the purity metric for nuclide $k$,

$S^k_i$ is the main effect sensitivity index for nuclide $k$,

$S^k_T$ is the total sensitivity index for nuclide $k$,

$|S^k_T - S^k_i|$ is the interaction amount of nuclide $k$ with other variables.

Table 5.6: $^{239}$Pu sensitivity "purity" calculated from $S_i$ and $S_T$ values.

| Energy Range [MeV] | Purity |
|---|---|
| 3.000E-01 - 2.600E-01 | 0.3943 |
| 3.000E+00 - 2.750E+00 | 0.0912 |
| 1.500E-01 - 1.000E-01 | 0.0702 |
| 2.000E-01 - 1.500E-01 | 0.0583 |
| 1.200E+00 - 1.000E+00 | 0.0508 |
| 7.000E-01 - 6.000E-01 | 0.0203 |
| 2.500E+00 - 2.350E+00 | 0.0202 |
| 2.000E+00 - 1.800E+00 | 0.0192 |
| 2.350E+00 - 2.150E+00 | 0.0185 |
| 2.750E+00 - 2.500E+00 | 0.0170 |

Table 5.7: $^{238}$U sensitivity "purity" calculated from $S_i$ and $S_T$ values.

| Energy Range [MeV] | Purity |
|---|---|
| 2.500E+00 - 2.350E+00 | 28.7353 |
| 2.350E+00 - 2.150E+00 | 19.7467 |
| 9.000E-01 - 8.000E-01 | 9.7064 |
| 3.000E+00 - 2.750E+00 | 6.2667 |
| 2.750E+00 - 2.500E+00 | 5.2323 |
| 1.500E-01 - 1.000E-01 | 4.9412 |
| 2.000E+00 - 1.800E+00 | 4.0564 |
| 3.000E-01 - 2.600E-01 | 3.2312 |
| 1.200E+00 - 1.000E+00 | 3.1166 |
| 4.500E-01 - 4.000E-01 | 2.9806 |

$^{238}$U purity values are noticeably higher than $^{239}$Pu values. The lower purity values associated with $^{239}$Pu stem from high interactions in those photon energy bins. Notably, all the ratios used in the experimental portion and found in Table 5.8 stem from $^{238}$U and $^{239}$Pu purity metrics except the 2.600E-01 - 2.000E-01 MeV energy bin. The 2.600E-01 - 2.000E-01 MeV energy bin was found to have a high purity value for $^{235}$U which was also present, albeit small, during irradiation.

Table 5.8: Selected experimental ratio delayed emission results from SA guided analysis. **Acquired during fission or front-end period. See Table 5.5 for configuration specifications.

| Ratio [MeV] | Config. 1 | Config. 2 | Config. 3 | Config. 4 |
|---|---|---|---|---|
| $\frac{0.2-0.26}{0.1-0.15}$ | 2.02 | 3.52 | 5.16 | 7.66 |
| $\frac{0.26-0.3}{0.1-0.15}$ | 0.64 | 1.55 | 2.70 | 4.54 |
| $\frac{0.26-0.3}{0.2-0.26}$ | 0.32 | 0.44 | 0.52 | 0.59 |
| $\frac{0.26-0.3}{0.2-0.26}$** | 0.58 | 0.74 | 1.36 | 1.60 |
| $\frac{0.4-0.45}{0.2-0.26}$ | 0.75 | 0.59 | 0.56 | 0.51 |
| $\frac{0.8-0.9}{0.6-0.7}$ | 0.80 | 0.61 | 0.47 | 0.52 |
| $\frac{2.35-2.5}{0.26-0.3}$ | 0.0094 | 0.0024 | 0.0020 | -0.00094 |

Results of this analysis are shown in Table 5.8 using the sensitivity indices/purity metric derived from computational calculations. Table 5.8 shows sensitivities to the amount of $^{Nat}$U and $^{239}$Pu present during irradiation. The ratios used provide indicators of fuel present with 0.01 seconds. Also, the $\frac{0.26-0.3\text{MeV}}{0.2-0.26\text{MeV}}$ ratio behaved well within the short 10 microsecond fission period yielding an instantaneous indicator of fuel type. While the results show sensitivities, irradiations with more coverage of fissile fuel proportions would provide better indications of emission dependencies. Regardless, the ratios displayed clear sensitivities to the fuel types present and energy range sensitivity indices developed from the SA promoted faster and more focused experimental analyses.

## 5.3 Peri-Detonation Policy Implications

The rise in nuclear smuggling and nuclear criminal activity has brought into question traditional deterrence strategy [49]. One technical indirect deterrence strategy involves developing and maintaining stronger nuclear treaty monitoring programs. Stronger monitoring

programs, such as the CTBTO employed passive monitoring stations have conceivably deterred nuclear states from conducting nuclear weapon testing. Implementing and advancing passive monitoring capabilities supplements existing nuclear deterrence strategies.

Deterring nuclear states from using nuclear weapons follows Cold War logic where boundaries and consequences were clearly defined. The advancement of nuclear device design and strike capabilities offers a limited deterrent when applied to nuclear terrorism. Lack of controls and the global availability of nuclear material increases the likelihood of nuclear terrorism.

Cases of state sponsored nuclear proliferation increase possibilities of nuclear terrorism. North Korea allegedly transferred and sold Libya approximately 2 metric tons of unenriched uranium but pledged to not transfer to terrorists [49]. Countries with known ties to terrorism raise concerns when nuclear capabilities are sought. Moreover, a country on the verge of collapse or drastic political change presents greater risk of assisting and providing a means to nuclear terrorists with the hopes of creating a tangential "swan song" strike [49]. The opinion exists, that the retaliation magnitude of the U.S., or other country(ies), and the fear of attribution deters states from transferring nuclear materials to terrorist organizations [49]. Nuclear forensic science empirically bolsters fear of discovery and creates an indirect deterrent to potential source state proliferation complementing direct deterrence measures.

Post-detonation nuclear forensics provides technical nuclear forensic information which may be used for attribution purposes. Current collection techniques and analysis methods require extended time lines that potentially hinder timely attribution. There are many questions surrounding the ability of post-detonation nuclear forensics contributing to and supporting attribution. Peri-detonation nuclear forensics provides empirical technical nuclear forensics information and avoids complications with timely debris collection.

Peri-detonation period of time encompasses effects up to roughly 60 seconds. The nuclear cloud from a 20 kiloton surface burst reaches 2 miles at this time which is approximately the effective distance of gamma rays creating a limit of detectability and appropriate

cut-off point. These phenomena were divided into 2 periods, front-end prompt burnup and back-end delayed emission. The front-end time-period encompass fission, structural, and environmental emissions while the back-end interval encompasses fission product and environment activation emissions.

SA computational results coupled with the MCF algorithm, indicate passively measurable emissions can be used to infer device characteristics. These early-time device characteristics point to source sophistication and intent. Fat Man derivative results showed the effect of a resolvable rate during the front-end fission period on matching accuracy. While the Little Boy design derivative results contained high error because of the unresolvable rate which is caused by higher emission leakage. These high errors due to unresolvable rates were drastically reduced when the nuclear cloud rise signatures were considered. If data is unavailable or unusable during the prompt period, signatures from nuclear cloud rise up to 60 seconds may provide useful technical nuclear forensic information for attribution.

Configuration derivative results allowed for hypothetical efficiency estimates indicating sophistication level. Sophistication and HOB estimates are clear indicators of source capability and intent. A low HOB coupled with crude device design conceivably stipulates terrorist activity (or the outward appearance) while a high HOB and a sophisticated design may be indicative of a sophisticated source.

Experimental results highlight ratio sensitivities on fuel type(s) present. These ratios were found from computational sensitivity analysis results on $LaBr_3$(Ce) integral counts considering detector response. Some ratios yielded clear sensitivities for present fissile/fissionable fuel indicating viable early-time ratios for rapid fuel type determination. Results of computational and experimental portions performed well for near immediate attribution indicators but also displayed limitations.

Peri-detonation nuclear forensics shows promise for contributing to early-time technical nuclear forensics information used for attribution. Peri-detonation nuclear forensics is also not without limitations. Collection requirements dictate surviving or existing radi-

ation monitoring stations. Existing stations are either fortuitously or strategically placed and also, like other methods, require time for data acquisition and processing. Cost of implementing and maintaining monitoring stations is likely high, but in terms of nuclear deterrence is invaluable. Also, early-time sophistication determination is not full-proof. A crudely designed device could originate from any known and unknown weapons states. Laboratory analyses would produce more accurate results related to the source by quantifying nuanced characteristics (e.g. enrichment, purity, structural components) in a more controlled setting.

Segregation into peri- and post-detonation nuclear forensics is necessary because of the level of information and methods associated with each period. As time progresses, more characteristics come to light as analysis settings move from the field to laboratory. Ultimately, policy maker risk tolerance determines if using early-time, oftentimes vague, indicators containing larger uncertainty is better than using more definitive nuanced indicators, also with uncertainty, that arrive later in time. Peri-detonation signature capabilities coupled to other relevant information could provide an effective indirect deterrent to sophisticated source state proliferation.

## 5.4 Peri-Detonation Nuclear Forensics Future Work

The phenomena surrounding an urban nuclear device detonation is complex and affects early-time emissions. These emissions also contain uncertainties related to nuclear data, experimental setup, phenomena assumptions/approximations. How to minimize these errors while maintaining fidelity and reasonable computation times is a tough problem that needs to be addressed. What is an acceptable level of error when applied to political action is an important question that would determine the level of empirical evidence needed for attribution purposes.

In this research, simplified models were used to demonstrate device design effects and differences of measurable output. The research can be extended to other designs and pa-

rameterized into design sensitivities rather than discretized components. The methods were completed on prompt phenomena up to 60 seconds following detonation but the methods could easily be extended to sample/particulate collection time frames. An extended application time could optimize measurement times for determining device characteristics. Optimistically, the method could also be tailored for other measurement techniques such as mass spectrometry, beta, and alpha detection.

Experimentally, fuel-type sensitivities were demonstrated up to 0.01 seconds using small fractional amounts of $^{239}$Pu due to availability. Other fractional ratios of $^{239}$Pu should be explored to better fill the gaps in trends/sensitivities.

## 5.5 Sponsor Acknowledgment and Disclaimer

This material is based upon work supported by the U.S. Department of Homeland Security under Grant Award Number, 2012-DN-130-NF0001-02. The views and conclusions contained in this document are those of the authors and should not be interpreted as necessarily representing the official policies, either expressed or implied, of the U.S. Department of Homeland Security.

## REFERENCES


[1] Pub. L. 111 - 140, 6 USC. Sec 2, *Nuclear Forensics and Attribution Act*, 2010.

[2] W. J. Perry, B. Scowcroft, and C. D. Ferguson, *U.S. Nuclear Weapons Policy*. Council on Foreign Relations, 2009, pp. 105, 114.

[3] S. Glasstone and P. Dolan, *The Effects of Nuclear Weapons*, 3rd ed. United States Department of Defense, Energy Research, and Development Administration, 1977, pp. 17, 18.

[4] A. Saltelli, K. Chan, and E. M. Scott, *Sensitivity Analysis*. John Wiley and Sons, Ltd., 2000, pp. 6, 424.

[5] A. Saltelli, M. Ratto, F. Campolongo, and S. Tarantola, *Sensitivity Analysis in Practice*. John Wiley and Sons, Ltd., 2004, pp. 112,153,161.

[6] "Getting Mad: Nuclear Mutual Assured Destruction, its Origins and Practice," The U.S. Army War College, Tech. Rep., 2004.

[7] J. W. Knopf, "The Fourth Wave in Deterrence Research," vol. 31, no. 1, pp. 1–33, 2010.

[8] R. Jervis, "Deterrence Theory Revisited," vol. 31, no. 2, pp. 289–324, 1979.

[9] Pub. L. 114 - 328, Sec 1671, *National Defense Authorization Act*, 2016.

[10] D. K. Decker, "Before the First Bomb Goes Off: Developing Nuclear Attribution Standards and Policies," Harvard Kennedy School: Belfer Center for Science and International Affairs, Tech. Rep. Discussion Paper-2011-03, 2011.

[11] P. Geelhood, "Deterrence of Nuclear Terrorism via Post-Detonation Attribution: Is the United States on Target?" Master's thesis, Naval Postgraduate School, Monterey, California, Dec. 2009.

[12] P. Baxter, "The False Hope of Nuclear Forensics? Assessing the Timeliness of Forensics Intelligence," 2015.

[13] D. Cenciotti, "U.S. Air Force deploys WC-135 nuclear sniffer plane to Japan to monitor North Koreas possible nuke weapons tests," 2017.

[14] J. T. Richelson, *The U.S. Intelligence Community*, 7th ed. Westview Press, 2015, Chapter 9.

[15] M. Zhang and L. Wen, "High-precision location and yield of North Korea's 2013 nuclear test," vol. 40, pp. 2941–2946, 2013.

[16] A. B. Carter, M. M. May, and W. J. Perry, "The Day After: Action Following a Nuclear Blast in a U.S. City," 2007.

[17] A. Saltelli, M. Ratto, T. Andres, F. Campolongo, J. Cariboni, D. Gatelli, M. Saisana, and S. Tarantola, *Global Sensitivity Analysis: The Primer*. Wiley, 2008, pp. 11,20,59.

[18] C. M. Perfetti, "Advanced Monte Carlo Methods for Eigenvalue Sensitivity Coefficient Calculations," PhD thesis, University of Michigan, 2012, pp. 12–13.

[19] "Scale Code System," Oak Ridge National Laboratory, Tech. Rep. ORNL/TM-2005/39, 2016, Version: 6.2.1.

[20] R. J. M. Jr, C. Gesh, R. Pagh, R. Rucker, and R. W. III, "Compendium of Material Composition Data for Radiation Transport Monitoring," Pacific Northwest National Laboratory, Tech. Rep. PNNL-15870 Rev. 1, 2011.

[21] V. E. Fortov, *Extreme States of Matter High Energy Density Physics*. Springer, 2011, p. 123.

[22] Richard L. Holmes and Stephen W. White, "Standardized Unclassified Little Boy and Fat Man Outputs," Defense Threat Reduction Agency, Tech. Rep. DTRA-IR-13-67, 2013.

[23] "Scale: A Comprehensive Modeling and Simulation Suite for Nuclear Safety Analysis and Design," Oak Ridge National Laboratory, Tech. Rep. ORNL/TM-2005/39, 2011, Version: 6.1.

[24] C. R. Martin, "Fallout Fractionation in Silicate Soils," PhD thesis, Air Force Institute of Technology, Dec. 1983.

[25] E. O. Freiling, "Fractionation III. Estimation of Degree of Fractionation and Radionuclide Partition for Nuclear Debris," 1963.

[26] C. J. Bridgman, *Residual radiation*, Private Communication.

[27] G. E. Sjoden, *NRE 6201 Reactor Physics Notes*, 2012.

[28] G. Bell and S. Glasstone, *Nuclear Reactor Theory*. Litton Educational Publishing, Inc., 1970, p. 526.

[29] Saint-Gobain, *BrilLanCe 380 Lanthanum Bromide LaBr3(Ce) - Properties*, URL: http://www.crystals.saint-gobain.com/products/brillance-labr3-lanthanum-bromide., 2017.

[30] "Passive Nondestructive Assay of Nuclear Materials," Los Alamos National Laboratory, Tech. Rep. LA-UR-90-732, 1991, p. 43.

[31] M. Berger, J. Hubbell, S. Seltzer, J. Chang, J. Coursey, R. Sukumar, D. Zucker, and K. Olsen, "Xcom: Photon cross section database (version 1.5)," 2010, [Online] Available: http://physics.nist.gov/xcom.

[32] H. G. Norment, "DELFIC: Department of Defense Fallout Prediction System, Volume I - Fundamentals," 1979.

[33] H. G. Norment, "DELFIC: Department of Defense Fallout Prediction System, Volume III - Cloud Rise (Revised)," 1970.

[34] G. F. Knoll, *Radiation Detection and Measurement*, 4th ed. John Wiley and Sons, Inc., 2010, pp. 223, 234–253, 365–368, 424.

[35] P. B. Rose, "Imaging of special nuclear materials using monochromatic gamma rays from low-energy nuclear reactions," PhD thesis, Georgia Institute of Technology, Jan. 2017.

[36] Saint-Gobain, *PRELUDE 420 LYSO*.

[37] Saint-Gobain, *BGO Bismuth Germanate*.

[38] Saint-Gobain, *CsI(Tl) Thallium Activated Cesium Iodide*.

[39] Saint-Gobain, *BrilLanCe 380 Lanthanum Bromide $LaBr_3$(Ce)*.

[40] Saint-Gobain, *NaI(Tl) and Polyscin NaI(Tl) Sodium Iodide*.

[41] Eljen Technology, *NEUTRON/GAMMA PSD EJ-301, EJ-309*.

[42] Saint-Gobain, *$CdWO_4$ Cadmium Tungstate*.

[43] Eljen Technology, *PULSE SHAPE DISCRIMINATION EJ-299-33A, EJ-299-34*.

[44] H. Kim, G. Cho, and H. Kim, "Characteristics of a Stilbene Scintillation Crystal in a Neutron Spectrometer," *Radiation Measurements*, vol. 58, pp. 133 –137, 2013.

[45] S. Yip, *Nuclear Radiation Interactions*. World Scientific, 2015, pp. 250–257.

[46] M. Litz, C. Waits, and J. Mullins, "Neutron-Activated Gamma-Emission: Technology Review," Army Research Laboratory, Tech. Rep. ARL-TR-5871, 2012.

[47] K. S. Krane, *Introductory Nuclear Physics*. John Wiley and Sons, Inc., 1988, pp. 462–463.

[48] G. B. Jr., "University Loaned Normal Uranium Slug Disposition - University Survey Responses," Westinghouse Savannah River Company, Tech. Rep. NMP-92-05, 1992.

[49] C. D. Ferguson, W. C. Potter, A. Sands, L. S. Spector, and F. L. Wehling, *The Four Faces of Nuclear Terrorism*. Routledge, 2005, p. 5.